eXPRESS Polymer Letters Vol.1, No.9 (2007) 545
Available online at www.expresspolymlett.com
DOI: 10.3144/expresspolymlett.2007.77

Editorial corner – a personal view
Fire retardancy of polymers: challenges and new concepts

Gy. Marosi[*]

Organic and Chemical Technology Department of Budapest University of Technology and Economics, H-1111 Budapest, Műegyetem rkp. 3, Hungary

The rapidly growing polymer market increases the risk of fire. The competition for reducing the costs and the activities for increasing the recyclability are advantageous from many aspects but promote the use of cheap and flammable polymers.

The relative amount of the types of fire retardants (FRs) used in polymers is changing. The halogen containing compounds initiate corrosion, furthermore, some of them proved to be harmful to the environment and human health. Therefore the new European regulations promote the substitution of some conventional flame retardants by environmental-friendly ones.

Reactive processing methods bond the additives to the polymer chains thus provide solution against their release to the environment, which is critical especially for some potential pseudohormones. Beyond the increasing importance of reactive methods the nano-concept is the most widely investigated novel approach to fire retardancy. Promising is the low environmental impact of nanofillers and influence on the macromolecular arrangement owing to their high surface area (reducing the heat distortion and melt dripping at high temperature). However, their fire retardancy performance should be enhanced, which requires better understanding of the mechanism of their action. It has to be clarified what is the relative role of their catalytic and physical action. The importance of the geometric dimensions, quality of dispersion and the potential synergism between different types should be clarified as well. Furthermore, the undesirable by-effect of removing stabilizers from the polymer matrix through their high surface area has to be eliminated. Most recent concepts are the in situ formation of nanofillers (during extrusion of the polymers) and of FR-active interfaces or surfaces around inclusions. Advancement of these concepts require the development of new micro-scale fire modeling/testing methods.

Based on the described research activities increasing use of reactive, halogen free solutions in combination with nanofillers of well designed interfaces are predicted. Economic approaches applying recycled polymer matrices, nanofillers and multifunctional additives will increase in the close future. A multifunctional flame retardant can be applied for example as adaptive interlayer in a multiphase systems facilitating good mechanical, transport or adhesive performance at ambient temperature and transforming to protective (heat and combustible-gas barrier) layer at the temperature of combustion.

Prof. Dr. György Marosi
Member of International Advisory Board

[*]Corresponding author, e-mail: gmarosi@mail.bme.hu
© BME-PT and GTE

eXPRESS Polymer Letters Vol.1, No.9 (2007) 546–575
Available online at www.expresspolymlett.com
DOI: 10.3144/expresspolymlett.2007.78

Nanotechnology and its applications in lignocellulosic composites, a mini review

*S. Kamel**

University of Malakand, Pharmacy Department, Chakdara Dir, N.W.F.P., Pakistan
Permanent address; National Research Center, Cellulose & Paper Department, El-Tahrir St. Dokki, Cairo, P.O. 12622, Egypt

Received 1 March 2007; accepted in revised form 14 June 2007

Abstract. Nanotechnology has applications across most economic sectors and allows the development of new enabling science. The ability to see materials down to nanoscale dimensions and to control how materials are constructed at the nanoscale is providing the opportunity to develop new materials and products in previously unimagined ways.
This review covers the academic and industrial aspects of the preparation, characterization, material properties, crystallization behavior; melt rheology, and processing of polymer/cellulose or cellulose/cellulose nanocomposites. Cellulosic materials have a great potential as nanomaterials because they are abundant, renewable, have a nanofibrillar structure, can be made multifunctional, and self-assemble into well-defined architectures. The fibrillation of pulp fiber to obtain nano-order-unit web-like network structure, called microfibrillated cellulose, is obtained through a mechanical treatment of pulp fibers, consisting of refining and high pressure homogenizing processes. Also, nano-whisker can be used as novel reinforcement in nanocomposites; it can be obtained by acid hydrolysis from various sources such as wood, tunicin, ramie, cotton, wheat straw, bacterial cellulose, and sugar beet. The properties of nanocomposite materials depend not only on the properties of their individual parents, but also on their morphology and interfacial characteristics. Compared with plant cellulose, bacterial cellulose has found many applications in the biomedical field as tissue engineering materials due to their good biocompatibility, mechanical properties similar to those of hard and soft tissue and easy fabrication into a variety of shapes with adjustable interconnected porosity. One of the drawbacks of cellulose whiskers with polar surfaces is poor dispersibility/compatibility with nonpolar solvents or resins. Thus, their incorporation as reinforcing materials for nanocomposites has so far been largely limited to aqueous or polar systems. To overcome this problem and broaden the type of possible polymer matrices, efforts of surface modification have been made. These attempts include surfactant coating or graft copolymerization.

Keywords: *nanomaterials, nanocomposites, reinforcements, rheology and mehanical properties*

1. Introduction

1.1. Nanotechnology

Technology is the major driving factor for growth at every level of an economy. At the 1 nanometer (nm) scales and below, quantum mechanics rules, and at dimension above 100 nm classical quantum mechanics, physics, and chemistry dictate properties of matter. Between 1 and 100 nm, a hybrid exists, and interesting things can happen such as mechanical, optical, electrical, magnetic, and a variety of other properties can behave quite differently [1]. A nanometer is a billionth of a meter, or 80 000 times thinner than human hair. So, nanometer domain covers sizes bigger than several atoms but smaller than the wavelength of visible light. Nanotechnology (based on the Greek word for dwarf) is defined as the manipulation of materials measuring 100 nm or less in at least one dimension.

*Corresponding author, e-mail: samirki@yahoo.com
© BME-PT and GTE

Where the physical, chemical, or biological properties are fundamentally different from those of the bulk material. By expanding our understanding and control of matter at such levels, new avenues in product development can be opened [2].

Nanotechnology can be defined as the science and engineering involved in the design, synthesis, characterization, and application of materials and devices whose smallest functional organization in at least one dimension is on the nanometer scale or one billionth of a meter [3]. Classified by nanofiller dimensionality, there are a number of types of nanocompomposites. Zero-dimensional (nanoparticle), one-dimensional (nanofiber), two-dimensional (nanolayer), and three-dimensional (interpenetrating network) systems can all be imagined [4]. Also, lamellar nanocomposites can be divided into two distinct classes, intercalated and exfoliated. In intercalated nanocomposites, the polymer chains alternate with the inorganic layers in a fixed compositional ratio and have defined number(s) of polymer layers in the intralamellar space. In exfoliated nanocomposites, the number of polymer chains between the layers is almost continuously variable and the layers stand >100 Å apart. Determining and altering how materials and their interfaces are constructed at nano- and atomic scales will provide the opportunity to develop new materials and products. Because of this ability, nanotechnology represents a major opportunity for wood and wood-based materials to improve their performance and functionality develop new generations of products, and open new market segments in the coming decades [5]. Now it is possible to ask, why nanotechnology is important.

The answer is [6]:

a) Less space, faster, less material, and less energy.
b) Novel properties and phenomena.
c) Most efficient length scale for manufacturing.
d) Intersection of living/non-living.

Polymer nanocomposites are produced by incorporating materials that have one or more dimensions on the nanometer scale (<100 nm) into a polymer matrix. These nanomaterials are in the literature referred to as for example nanofillers, nanoparticles, nanoscale building blocks or nanoreinforcements. Nanocomposites have improved stiffness, strength, toughness, thermal stability, barrier properties and flame retardancy compared to the pure polymer matrix. Nanoreinforcements are also unique in that they will not affect the clarity of the polymer matrix. Only a few percentages of these nanomaterials are normally incorporated (1–5%) into the polymer and the improvement is vast due to their large degree of surface area [7]. Because of the nanometric size effect, these composites have some unique outstanding properties with respect to their conventional microcomposite counterparts. Since the pioneering work by the Toyota group [8–10] polymer nanocomposites have attracted an increasing amount of attention.

The properties of nanocomposite materials depend not only on the properties of their individual parents, but also on their morphology and interfacial characteristics. In the particular case of polymer reinforced with rigid nanofillers, various parameters seem to be of importance in characterizing the fillers: geometrical factors such as the shape, the size, and the aspect ratio; intrinsic mechanical characteristics such as the modulus or the flexibility; surface properties such as specific surface area and surface treatment [11]. The type of polymer matrix used and the possible effects of nanofillers on its microstructure and its intrinsic properties are also essential parameters determining the composite properties. In addition, the processing conditions can affect on composite properties. To study this factor high aspect ratio nanofibers/poly (styrene co-butyl acrylate) composites were prepared with two different processing conditions. It was found that, in case of evaporated cellulose filled composites; the highest mechanical reinforcement (with a mechanical percolation phenomenon) coupled to an increase in composites thermo-mechanical stability. While in case of freeze-dried cellulose filled composites; the freeze-drying process prevents the creation of strong contacts between nanofibrils, a lower mechanical reinforcement is measured [12].

Whereas the general class of inorganic nanocomposites has enjoyed much discussion and is still a fast-growing area of research, exciting new research on bio-based nanocomposites have a greater potential because the bio-resource can be both sustainable and genetically manipulated. Wood cellulose nanofibrils have about 25% of the strength of carbon nanotubes, which are expected to be the strongest fibers that can be produced. Their potential cost, however, might be 10 to 100 times less, giving cellulose nanofibrils a unique economic advantage [5].

1.2. Nanocomposite materials

The definition of nanocomposite materials has significantly broadened in the last few years. This term now encompasses a large variety of systems combining one-, two-, and three dimensional materials with amorphous materials mixed at the nanometer scale. Natural fibers are pervasive throughout the world in plants such as grasses, reeds, stalks, and woody vegetation. They are also referred to as cellulosic fibers, related to the main chemical component cellulose, or as lignocellulosic fibers, since the fibers usually often contain a natural polyphenolic polymer, lignin, in their structure.

The use of lignocellulosic fibers derived from annually renewable resources as a reinforcing phase in polymeric matrix composites provides positive environmental benefits with respect to ultimate disposability and raw material use [13]. By comparing with inorganic fillers, the main advantages of lignocellulosics are;

- Renewable nature
- Wide variety of fillers available throughout the world
- Nonfood agricultural based economy
- Low energy consumption
- Low cost
- Low density
- High specific strength and modulus
- High sound attenuation of lignocellulosic based composites
- Relatively reactive surface, which can be used for grafting specific groups.
- The recycling by combustion of lignocellulosic filled composites is easier in comparison with inorganic fillers systems.

Therefore, the possibility of using lignocellulosic fibers as a reinforcing phase has received considerable interest. In addition, it is necessary to discuses the intrinsic nanoscale properties of wood and similar lignocellulosic materials for developing advanced nanomaterials and use nanoprocesses to modify lignocellulosic materials.

1.2.1. Structure of wood fiber

The structure of wood spans many length scales: meters for describing the whole tree, centimeters for describing structures within the tree cross section (pith, heartwood, sapwood, and bark), millimeters for describing growth rings (early wood, latewood), tens of micrometers for describing the cellular anatomy, micrometers for describing the layer structure within cell walls, tens of nanometers for describing the configuration of cellulose fibrils in a matrix of hemicellulose and lignin, and nanometers for describing the molecular structures of cellulose, hemicellulose, and lignin and their chemical interactions.

Wood fibers, the most abundant biomass resource on earth, are hollow tubes made up of cellulose embedded in a matrix of hemicellulose and lignin. Most of the cell-wall materials are located in the second layer, which consists of a helically wound framework of microfibrils (Figure 1) [14]. The most important attribute of wood is its mechanical properties, in particular its unusual ability to provide high mechanical strength and high strength-to-

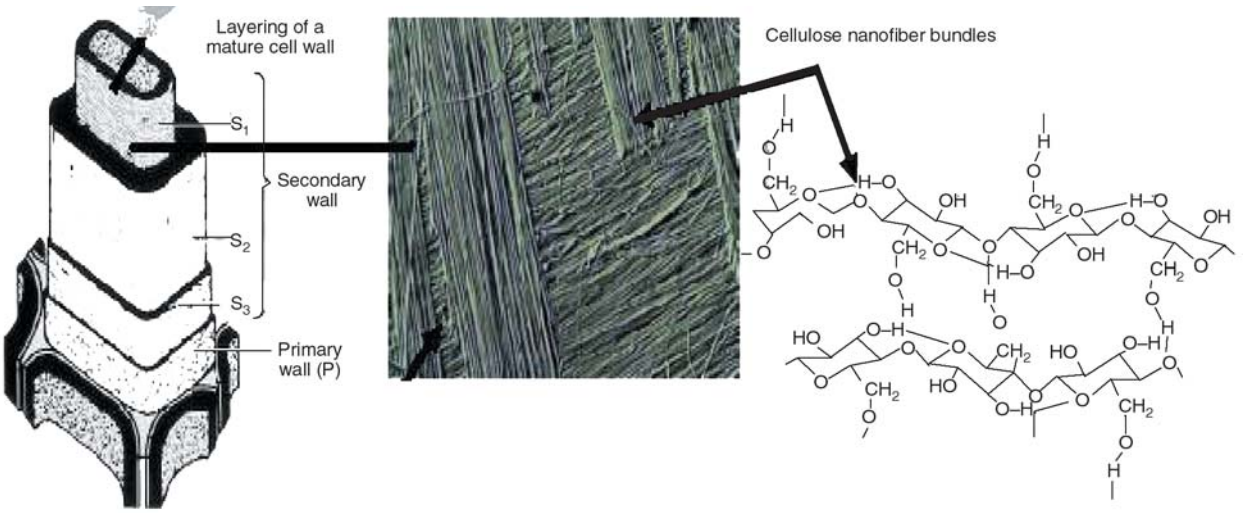

Figure 1. Microstructure of wood fiber cell wall: S_1, S_2, and S_3 are the inner, middle and outer layers of the secondary wall, respectively. Reproduced from; Jupiter.phys.ttu.edu/corner/1999/dec99.pdf

weight ratio while allowing for flexibility to counter large dimensional changes due to swelling and shrinking. These unique properties of wood are a direct result of its hierarchical internal structure. Microfibrils, nano-order-unit (10 nm×3.5 nm) [15] fibers that compose most fiber cell walls, consist of monocrystalline cellulose domains with cellulose chains parallel to the microfibril axis. As they are devoid of chain foldings and contain only a small number of defects, each microfibril can be considered a string of polymer whiskers having a modulus close to that of the perfect crystal of native cellulose, which is estimated to be 150 GPa, and possessing a strength of about 10 GPa [16]. Cellulose is a polydisperse linear polymer of poly-β(1,4)-D-glucose. The monomers are linked together by condensation such that glycosidic oxygen bridges join the sugar rings. In nature, cellulose chains have a degree of polymerization of approximately 10 000 glucopyranose units in wood cellulose and about 15 000 in native cellulose cotton. These cellulose chains are biosynthesized by enzymes, deposited in a continuous fashion and aggregate to form microfibrils, long threadlike bundles of molecules stabilized laterally by hydrogen bonds between hydroxyl groups and oxygen of adjacent molecules. Depending on their origin, the microfibril diameters range from about 2 to 20 nm for lengths that can reach several tens of microns. These microfibrils highly ordered (crystalline) regions alternate with less ordered (amorphous) regions [17]. Properties of cellulose crystallites from different earlier reports are concluded and shown in Table 1 [13, 17–22].

Beside cellulose I, cellulose II, III and IV are present with the possibility of conversion from one form to another [23]. Regenerated cellulose II is formed whenever the lattice of cellulose I is destroyed for example on swelling with strong alkali or on dissolution of cellulose. Since the strongly hydrogen bonded cellulose II is thermochemically more stable than cellulose I, so cellulose I can be converted into cellulose II but cellulose II can not be converted into cellulose I [17].

Table 1. Properties of cellulose crystallites

Property	Cellulose crystallites
Length [nm]	300–2000
Diameter [nm]	5–20
Aspect ratio, *L*/*d*	20–60
Tensile strength [MPa]	10 000
E-modulus [GPa]	150

1.2.2. Cellulosic whiskers

Native cellulose that reinforces most plant cell walls is a typical example of a material that can be described as whisker-like. Since amorphous regions act as structural defects, it is responsible for the transverse cleavage of the microfibrils into short monocrystals under acid hydrolysis [24, 25]. This procedure can be used to prepare highly crystalline particles called microcrystalline cellulose [26]. Microcrystalline cellulose consists generally of stiff rod-like particles called whiskers. Whiskers are obtained from natural fibers such as wood [27, 28], sisal [29], ramie [30], cotton stalks [31] wheat straw [22], bacterial cellulose [32, 33], sugar beet [34], chitin [35, 36], potato pulp [37, 38] as well as tunicin [39, 40].

The sea animals have a mantle consisting of cellulose microfibrils or tunicin embedded in a protein matrix. After deproteinization and acid hydrolysis, tunicin breaks down in the form of whiskers having several microns in length [41, 42].

Starting from the raw material and after successive chemical processing steps and, ultimately, controlled acid hydrolysis, the cellulose whisker microcrystals are suspended in aqueous media. Geometrical characteristics of cellulose whiskers depend on the origin of cellulose microfibrils, as well as on acid hydrolysis process conditions such as time, temperature, and purity of material. De Souza *et al.* [43] studied two rodlike systems in aqueous suspensions, cotton and tunicate whiskers the average size whisker dimensions are $L = 255$ nm and $d = 15$ nm for the cotton (ratio $L/d = 17$) while $L = 1160$ nm and $d = 6$ nm (ratio $L/d = 72.5$) for the tunicate whiskers. The whiskers are relatively easy to prepare as they are dispersible in water, in a variety of sizes, and can be used in composite liquids.

The main characteristics of the whiskers are their high aspect ratio and their nanoscopic size. For this reason, the interface area offered by the whiskers surface is high. This might lead to the formation of an interphase in which mechanical properties of the matrix are modified like the nanocomposite of plasticized poly (vinyl chloride) matrix reinforced by cellulose whiskers [44]. In addition, Dong *et al.* [45] also studied the effect of preparation conditions (time, temperature, and ultrasound treatment) on the resulting cellulose microcrystals structure from sulfuric acid hydrolysis of cotton fiber. They reported a decrease in microcrystalline cellulose

length and an increase in their surface charge with prolonged hydrolysis time. On the other hand, using of sulfuric acid for cellulose whiskers preparation leads to more stable whiskers aqueous suspension than that prepared using hydrochloric acid [29]. Indeed, the H_2SO_4-prepared whiskers present a negatively charged surface, whereas the HCl prepared whiskers are not charged. Another way to achieve charged whiskers consists of the oxidation of the whiskers surface [46, 47] or the post-sulfation of HCl-prepared microcrystalline cellulose [48]. So, whiskers can be defined as the fibers that have been grown under controlled conditions that lead to the formation of high-purity single crystals [49–51]. Acid hydrolysis of native cellulose leads to aqueous rod-like suspensions of elongated microcrystals with high aspect ratio. Depending on their origin, their lateral dimensions range from 2 to 50 nm, with length up to several micrometers. When suspended in water, the cellulose whiskers do not flocculate as they are stabilized by electrostatic repulsion arising from ionic species grafted during the acidic treatment.

Cellulose whiskers have a mechanical strengths equivalent to the binding forces of adjacent atoms leading to highly ordered structure, which produces not only unusually high strength but also significant changes in electrical, optical, magnetic, ferromagnetic, dielectric, conductive, and even superconductive properties. So, it can be used as a reinforcement of polymer matrix [52]. The reinforcing ability of the cellulose whiskers lies in their high surface area and good mechanical properties [53]. However, to obtain a significant increase in material properties the whiskers should be well separated and evenly distributed in the matrix material.

One of the drawbacks in using polar surface cellulose whiskers is that they cannot be uniformly dispersed in non-polar media such as organic solvents or monomers. Thus, their incorporation as reinforcement material for nanocomposite processing or their use as complex fluids has so far been mainly limited to aqueous or polar environment. In order to obtain non-flocculated dispersion of cellulose in non-polar solvents such as alkanes, one can envisage two routes, namely (a) coat the surface of the whiskers with surfactants having polar heads and long hydrophobic tails, and (b) graft hydrophobic chains at the surface of the cellulose whiskers. By the first route, Bonini *et al.* [54] dispersed the surfactant coated whisker in toluene by mixing of

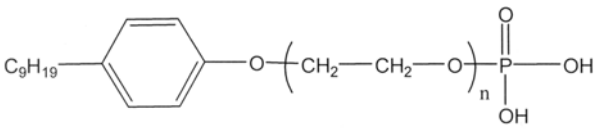

Figure 2. Chemical structure of the surfactant phosphoric ester of poly(ethylene oxide)

surfactants with cellulose whisker in aqueous suspensions. After freeze-drying of these suspensions, the surfactant coated whisker could be dispersed in cyclohexane. By surface acetylation stable suspension of cellulose whiskers with degree of substitutions of 0.75 could be obtained in acetone, but not in solvents of lower polarity [55]. Another recent approach has described suspensions of cellulose whisker in toluene using phosphoric ester of poly (ethylene oxide) as surfactant (Figure 2), these aqueous cellulose whisker suspensions are usually stabilized by steric repulsion between poly (ethylene glycol) chains grafted on the surface.

Using surface silylation of the cellulose whiskers with different silylating agents such as; isopropyl dimethyl chlorosilane, n-butyldimethyl chlorosilane, n-octyldimethyl chlorosilane or n-dodecyldimethyl chlorosilane (Figure 3), the whiskers could be homogeneously dispersed without aggregation in various organic solvents of medium polarity, such as acetone or tetrahydrofurane but not in solvents of very low polarity such as toluene or hexane [56].

As mentioned before, wood cellulose nanofibrils have about 25% of the strength of carbon nanotubes, by comparing the mechanical and electrical behavior of poly (styrene-co-butyl acrylate) nanocomposites [57, 58] reinforced by cellulose nanofibrils (obtained from sugar beet pulp) and multi-walled carbon nanotubes (synthesized from the catalytic decomposition of acetylene at 720°C on supported cobalt/iron catalyst) [59], a high reinforcement effect is achieved for cellulose filled materials, suggesting the presence of a rigid cellulose nanofibril network, linked by strong hydrogen bonds, within the material. With carbon nanotubes as fillers, no strong interactions are possible between multi-walled carbon nanotubes. The soft

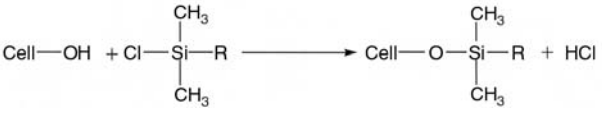

Figure 3. Preparation of silylated cellulose whiskers
R = i-C_3H_7, n-C_4H_9, n-C_8H_{17}, n-$C_{12}H_{25}$

entangled nanotube network was found to have an influence on the composite tensile behavior only at high temperatures. Such a soft network is efficient for mechanical reinforcement when the polymer matrix is highly viscous. Opuntia ficus-indica cladode cells were individualized under alkaline conditions and homogenized under a shear action to produce cellulose microfibril suspensions. Individualized microfibrils consist of flexible and hairy, high aspect ratio fibers almost 5 nm in width. The resulting suspension was used to process nanocomposite materials with a high level of dispersion using latex of poly (styrene-co-butyl acrylate) as a matrix. Cellulose microfibrils bring a great reinforcing effect at high temperature ($T > T_g$ of the matrix) and improve the thermal stability of the composite materials, even at very low filler loading. The swelling behavior of the polymeric matrix was found to strongly decrease even at only 1 wt% of cellulose microfibrils and was almost independent of the filler content [60].

Three types of surface characteristics cellulose whiskers were compared; aggregated whiskers without surface modification, aggregated whiskers grafted with maleated polypropylene, and novel surfactant-modified whiskers. The whiskers were incorporated as nanometric fillers in, polypropylene, by solvent casting from toluene followed by film pressing. The crystallization behavior of the films, as evaluated by X-ray diffraction, displayed two crystalline forms (α and β) in the nanocomposites containing aggregated whiskers without surface modification and novel surfactant-modified whiskers, whereas the neat matrix and the material reinforced with aggregated whiskers grafted with maleated polypropylene only crystallized in the α-form. Differential scanning calorimetry experiments also indicated that the aggregated surfactant-modified whiskers acted as nucleating agents for the polypropylene. The α-phase crystallites represent the predominant part of the neat polypropylene, whereas the appearance of the other two phases (β or γ) may eventually be favored by the presence of fillers, under high pressure or by thermal annealing. The mechanical properties of the nanocomposite films were evaluated by dynamic mechanical analysis, and were found to be significantly enhanced by the incorporation of the cellulose whiskers. Particularly, the materials with novel surfactant-modified whiskers and aggregated whiskers without surface modification displayed increased moduli as compared to the neat matrix and the aggregated whiskers grafted with maleated polypropylene composite. The presence of the β-phase may have an important influence on the mechanical properties of the resulting composites, since its toughness is higher than that of the α-phase [61]. An environmental friendly chemical modification route to confer high hydrophobicity to crystalline cellulose was developed. With low reagent consumption and simple treatment procedures, highly hydrophobic whiskers can be obtained. The acylated whiskers, using *iso*-octadecenyl succnic anhydride and *n*-tetradecenyl succinic anhydride as acylating agent, could disperse in medium- to low-polarity solvents, i. e., dimethyl sulfoxide to 1,4-dioxane. By controlling the heating time, whiskers with different dispersibility could be obtained. Based on its organic-solvent dispersibility, the acylated whiskers are expected to be useful in direct mixing with synthetic resins to form nanocomposites with improved dispersion and adhesion with matrices [55].

1.2.3. Bacterial cellulose

Besides being the cell-wall component of plants, cellulose is also secreted extracellularly as synthesized cellulose fibers by some bacterial species. Bacterial cellulose is produced by *Acetobacter* species cultivated in a culture medium containing carbon and nitrogen sources. It presents unique properties such as high mechanical strength and an extremely fine and pure fiber network structure. This network structure is in the form of a pellicle made up of a random assembly of ribbon shaped fibrils, less than 100 nm wide, which are composed of a bundle of much finer microfibrils, 2 to 4 nm in diameter. Bacterial cellulose microfibrils have a density of 1600 kg/m^{-3} [62–65]. In addition, it has sufficient porosity, 3-dimensional (3-D) network structure, water holding capability, and biocompatibility [66].

Instead of being obtained by fibrillation of fibers, bacterial cellulose is produced by bacteria in a reverse way, synthesizing cellulose and building up bundles of microfibrils. These bundles are somewhat straight, continuous, and dimensionally uniform. In addition, compared with animal-derived polymers, bacterial cellulose is free of any occurrence of cross infection likely associated with collagen. Current applications for bacterial cellulose

include use as a dietary food, as medical pads for skin burns, as reinforcement in high-strength papers, as binding or thickening agents, and as diaphragms of lectoracoustic transducers [67–70]. For the last application, Nakagaito *et al*. [71] reported a markedly high dynamic Young's modulus, close to 30 GPa, for sheets obtained from bacterial cellulose pellicles when adequately processed. Due to this remarkable modulus, bacterial cellulose sheets seemed to be an ideal candidate as raw material to further enhance the Young's modulus of high-strength composite. When bacterial cellulose pellicles compressed into sheets and impregnated with phenolic resin to produce high-strength composites. The Young's modulus of the composites was significantly higher when compared to that of microfibrial cellulose-based composites, 28 GPa against 19 GPa, respectively. The higher modulus of bacterial cellulose composites was credited to the extremely fine, pure, and dimensionally uniform ribbon-like cellulose microfibril bundles, arranged in a network of relatively straight and continuous alignment, and also to the planar orientation of these elements obtained through the compression of the bacterial cellulose pellicles into sheets.

1.2.4. Starch

There are numerous examples where animals or plants synthesize extracellular high-performance skeletal biocomposites consisting of a matrix reinforced by fibrous biopolymers. Cellulose and chitin are classical examples of these reinforcing elements, which occur as whisker-like microfibrils that are biosynthesized and deposited in a continuous fashion. Starch is another example of natural semicrystalline polymer that is produced by many plants and occurs as microscopic granules. It acts as a storage polymer in cereals and tubers. These abundant and natural polymers can be used to create high performance nanocomposites presenting outstanding properties. Starch granules become swollen and gelatinized when water is added or when they are heated, and water is often used as a plasticizer to obtain desirable product properties and during

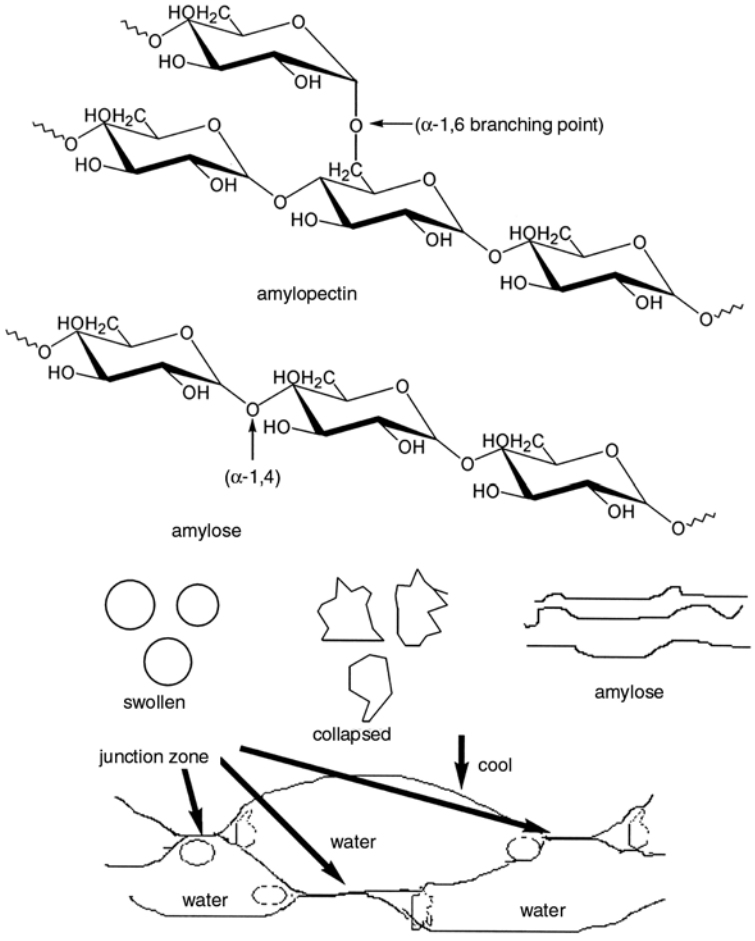

Figure 4. Starch gelation

this swelling amylose leaches out the water but amylopectin forms gel (Figure 4) [72]. Gelatinization of starch was found to lead to the destruction or diminution of hydrogen bonding in granules and a decrease in crystallinity of starch [73].

Aqueous suspensions of crystallites can be prepared by acid hydrolysis of the purified substrates. The object of this treatment is to dissolve away regions of low lateral order so that the water-insoluble, highly crystalline residue may be converted into a stable suspension by subsequent vigorous mechanical shearing action. For cellulose and chitin, these monocrystals appear as rod-like nanoparticles, dimensions of which depend on the biological source of the substrate. In the case of starch they consist of platelet-like nanoparticles. High reinforcing capability was reported resulting from the intrinsic chemical nature of these polymers and from their hierarchical structure [74]. On the other hand, amylose content in starch may affect the properties of the prepared composites. Ke *et al.* [75] studied the effect of amylose content in starches on the mechanical properties. Four dry corn starches with different amylose content were blended with poly lactic acid at various starch/poly lactic acid ratios and characterized for morphology, mechanical properties and water absorption. Tensile strength and elongation of the blends decreased as starch content increased, but no significant difference was observed among the four starches at the same ratio of starch/poly lactic acid. The rate and extent of water absorption of starch/poly lactic acid blends increased with increasing starch. Blends made with high-amylose starches had lower water absorption than the blends with normal and waxy corn starches.

Starch can be used as a reinforcing or a matrix. Nanocomposite materials were obtained using glycerol plasticized starch as the matrix and a colloidal suspension of cellulose whiskers as the reinforcing phase. After mixing the raw materials and gelatinization of starch, the resulting suspension was cast and evaporated under vacuum. The composites were conditioned at various moisture contents in order to evaluate the effect of this parameter on the composite structure. The specific behavior of amylopectin chains located near the interface in the presence of cellulose probably led to a transcrystallization phenomenon of amylopectin on cellulose whiskers surface [76]. The reinforcing effect of whiskers strongly depended on the ability of cellulose filler to form a rigid network, resulting from strong interactions between whiskers such as hydrogen bonds, and therefore on the moisture content. It was shown that increasing water content induced the crystallization of amylopectin chains and the accumulation of plasticizer in the cellulose/amylopectin interfacial zone [77]. Another approach is using latex of poly (hydroxyoctanoate) as a matrix and using a colloidal suspension of hydrolyzed starch or cellulose whiskers as natural and biodegradable filler. High-performance materials were obtained from these systems, preserving the natural character of poly (hydroxyoctanoate). Specific polymer-filler interactions and geometrical constraint due to the particle size of the latex have to be considered to account for the mechanical reinforcement effect of cellulose whiskers [78].

2. Preparation

2.1. Nanofibrill

A variety of techniques have been used to make nanostructures.

2.1.1. By mechanical fibrillation

The fibrillation of pulp fiber to obtain nano-order-unit web-like network structure, called microfibrillated cellulose, is obtained through a mechanical treatment of pulp fibers, consisting of refining and high pressure homogenizing processes. The refining process used is common in the paper industry, and is accomplished via a piece of equipment called a refiner. In a disk refiner, the dilute fiber suspension to be treated is forced through a gap between the rotor and stator disks, which have surfaces fitted with bars and grooves, against which the fibers are subjected to repeated cyclic stresses. This mechanical treatment brings about irreversible changes in the fibers, increasing their bonding potential by modification of their morphology and size. In the homogenization process, dilute slurries of cellulose fibers previously treated by refining are pumped at high pressure and fed through a spring high pressure loaded valve assembly. As this valve opens and closes in rapid succession, the fibers are subjected to a large pressure drop with shearing and impact forces. This combination of forces promotes a high degree of microfibrillation of the cellulose fibers, resulting in microfibrillated cellulose [79].

Figure 5. Homogenizer (Microfluidizer) used for the production of microfibrillated cellulose

The refining process is carried out prior to homogenization due to the fact that refining produces external fibrillation of fibers by gradually peeling off the external cell wall layers (*P* and S_1 layers) and exposing the S_2 layer and also causes internal fibrillation that loosens the fiber wall, preparing the pulp fibers for subsequent homogenization treatment [80].

Nakagaito *et al*. [81] studied how the degree of fibrillation of pulp fibers affects the mechanical properties of high strength cellulose composites. It was found that fibrillation solely of the surface of the fibers is not effective in improving composite strength, though there is a distinct point in the fibrillation stage at which an abrupt increase in the mechanical properties of composites occurs. In the range between 16 and 30 passes through refiner treatments, pulp fibers underwent a degree of fibrillation that resulted in a stepwise increment of mechanical properties, most strikingly in bending strength. This increase was attributed to the complete fibrillation of the bulk of the fibers. For additional high pressure homogenization-treated pulps, composite strength increased linearly against water retention values, which characterize the cellulose's exposed surface area, and reached maximum value at 14 passes through the homogenizer (Figure 5.).

2.1.2. By electrospinning of polymer

Electrospinning derived from electrostatic spinning. Electrospinning has been recognized as an efficient technique for the fabrication of polymer nanofibers. Various polymers have been successfully electrospun into ultrafine fibers e.g. cellulose acetate. There are basically three components to fulfill the process: a high voltage supplier, a capillary tube with a pipette or needle of small diameter, and a metal collecting screen. In the electrospinning process a high voltage is used to create an electrically charged jet of polymer solution or melt out of the pipette. Before reaching the collecting screen, the solution jet evaporates, and is collected as an interconnected web of small fibers [82, 83]. One electrode is placed into the spinning solution/melt, the other is attached to the collector. The electric field is subjected to the end of the capillary tube that contains the solution fluid held by its surface tension. This induces a charge on the surface of the liquid. The potential difference depended on the properties of the spinning solution, such as polymer molecular weight and viscosity. When the distance between the spinneret and the collecting device was short, spun fibers tended to stick to the collecting device as well as to each other, due to incomplete solvent evaporation. Mutual charge repulsion and the contraction of the surface charges to the counter electrode cause a force directly opposite to the surface tension [84]. As the intensity of the electric field is increased, the hemispherical surface of the fluid at the tip of the capillary tube elongates to form a conical shape known as the Taylor cone [85]. By further increasing in the electric field, a critical value is attained with which the repulsive electrostatic force overcomes the surface tension and the charged jet of the fluid is ejected from the tip of the Taylor cone. The discharged polymer solution jet undergoes an instability and elongation process, which allows the jet to become very long and thin. Meanwhile, the solvent evaporates, leaving behind a charged polymer fiber. In the case of the melt the discharged jet solidifies when it travels in the air.

Most of the polymers were dissolved in some solvents before electrospinning. When the solid polymer or polymer pellet is completely dissolved in a proper amount of solvent that is held, for example, in a glass container, it becomes a fluid form called polymer solution. The polymer fluid is then introduced into the capillary tube for electrospinning. Both the dissolution and the electrospinning are essentially conducted at room temperature with atmosphere condition.

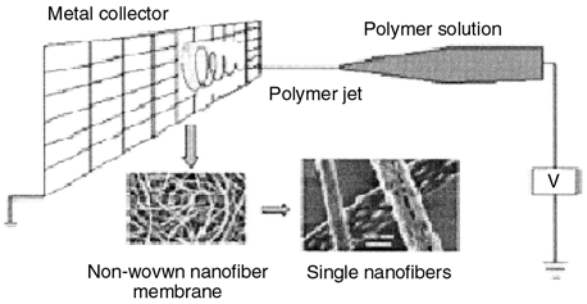

Figure 6. Schematic diagram to show polymer nanofibers by electrospinning.

Polymers, molten in high temperature, can also be made into nanofibers through electrospinning. Instead of a solution, the polymer melt is introduced into the capillary tube. However, different from the case of polymer solution, the electrospinning process for a polymer melt has to be performed in a vacuum condition [86–88]. Namely, the capillary tube, the traveling of the charged melt fluid jet and the metal collecting screen must be encapsulated within a vacuum. A schematic diagram to interpret electrospinning of polymer nanofibers is shown in Figure 6.

A polymer solution, such as cellulose acetate dissolved in 2:1 acetone: dimethyl acetamide was introduced into the electric field. The polymer filaments were formed, from the solution, between two electrodes bearing electrical charges of opposite polarity. One of the electrodes was placed into the solution and the other onto a collector. Once ejected out of metal spinnerets with a small hole, the charged solution jets evaporated to become fibers which were collected on the collector [89].

2.1.3. From sea animals

Colloidal suspensions of cellulose whiskers in water were prepared as following; the shells of the tunicates cut into small fragments and bleach by three successive treatments with sodium hypochlorite in dilute acetic acid. Heat the mixture to 70–80°C and keep at this temperature for 1 hour. After the third cycle, the tunicate mantles isolate via decanting, wash with ice water, and disintegrate in blender into an aqueous suspension (tunicate content ~3% w/w). The disintegrated mantles subsequently hydrolyze by adding concentrated sulfuric acid, heating the mixture to 80°C, and rigorous stirring at this temperature for 20 minute to yield a suspension of cellulose whiskers. After washing with water until the pH is neutral, adding water so that the whisker concentration, suspension of cellulose whiskers will be obtained [90].

2.1.4. From microcrystalline cellulose in organic solvent

The microcrystalline cellulose was swelled and partly separated to whiskers by chemical and ultra sonification treatments. Dimethyl acetamide with 0.5 wt% LiCl solution was used as swelling agent. The microcrystalline cellulose in LiCl/dimethyl acetamide was 10 wt% which was agitated using a magnetic stirrer for 12 hour at 70°C to swell the microcrystalline cellulose particles. The slightly swelled particles were then sonicated in an ultrasonic bath for 3 hours over a period of 5 days with long intervals between each sonication treatment, to separate cellulose nano whiskers [91].

2.1.5. By acid hydrolysis

Suspensions of nanocrystalline cellulose were prepared. Hydrolysis was carried out with sulfuric acid with constant stirring. Immediately following the acid hydrolysis, the suspension dilute 10-fold with deionized water to quench the reaction. The suspension centrifuges at 6000 rpm for 10 min to concentrate the cellulose and to remove excess aqueous acid. The resultant precipitate should be rinsed, recentrifuged, and dialyzed against water for 5 days until constant neutral pH [92].

2.1.6. From bacterial cellulose

Cellulose can be synthesized by some bacteria [31, 33]. For example, the cellulose was produced by static cultivation of Acetobacter xylinum, sub species BPR2001, in a fructose/CSL medium at 30°C [93]. The bacteria were grown in 400 ml Erlenmeyer flasks containing 100 ml of media. In order to remove the bacteria and to exchange remaining media, the produced cellulose pellicles were boiled in 1 M NaOH at 80°C for 1 hour followed by repetitive boiling in deionised water. To prevent drying and to avoid contamination, the washed cellulose was stored in diluted ethanol in a refrigerator.

The advantage in using bacterial cellulose as a model for plant cellulose lies in its high purity, fine fibrils (high surface area) [94], high tensile strength and water-holding capacity. So, bacterial cellulose

has been used as a reinforcing in nanocomposites [95].

2.2. Preparation of nanocomposite films

2.2.1. From regenerated cellulose

Microcrystalline cellulose powder is produced by acid hydrolysis of amorphous domains, which results in high crystallinity. Microcrystalline cellulose was activated for 6 hours in distilled H_2O at room temperature. Subsequently, the cellulose was dehydrated in ethanol, acetone, and N,N-dimethyl acetamide for 4 hours each. After decanting N,N-dimethyl acetamide from the dehydrated cellulose, LiCl/N,N-dimethyl acetamide solution was poured onto cellulose sample and stirred for 5 minutes. The solutions were then poured into Petri dish, and left at ambient atmosphere for 12 hour. After this time a 5–8 mm thick transparent gel had formed which was washed in distilled water and dehydrated between gently compressed sheets of paper. The final nanocomposite films were optically transparent and had a thickness between 0.2 and 0.5 mm [96].

2.2.2. By solution casting

For preparing solid polymer nanocomposite film, combine appropriate amounts of the nanoreinforcement's solution and dissolved polymer matrix.
Two processing conditions can be used to prepare the composites film from this mixture.
The mixture cast in a Petri dish and put in a drying oven under vacuum. The chosen temperature allows the solvent evaporation and the film formation (i. e. polymer particles coalescence). A so-called evaporated film is obtained and materials compression in mold under heating and pressure [92, 97].
The second route used to elaborate composite film, the mixture is first freeze-dried to allow water sublimation, and a compact soft powder is obtained. This powder then press under heating and pressure [62].

2.2.3. By extrusion

For mixing dry material with suspension solution; the composite materials will be compounded using a co-rotating twin-screw extruder with a gravimetric feeding system for dry materials and a peristaltic pump for the cellulose whiskers suspension. Figure 7, shows a schematic picture of the compounding process.

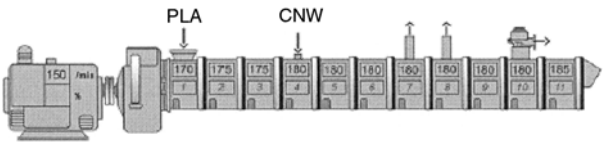

Figure 7. Schematic picture of the compounding process: feeding of poly (lactic acid) in zone 1, pumping of dispersed of cellulose whiskers in zone 4 and removal of the liquid using atmospheric and vacuum venting in zones 7, 8 and 10

For preparing nanocomposite film of poly (lactic acid)-malic anhydride-poly (ethylene glycol) reinforced with cellulose whiskers suspended in LiCl/dimethyl acetamide, poly (lactic acid) was fed in zone 1 and the cellulose whiskers suspension was pumped into the melted polymer at zone 4. The liquid phase was removed by atmospheric venting in zones 7 and 8 and by vacuum venting in zone 10. Both poly (lactic acid)-malic anhydride and poly (ethylene glycol) were premixed and fed in zone 1. The LiCl/dimethyl acetamide was removed by the venting system during the extrusion. The extruded materials were compression moulded to ~1.3 mm thickness.
The color on the samples was changed from transparent yellow to light brown which indicates thermal degradation. The color change and decreased mechanical properties indicates that the LiCl/dimethyl acetamide is not suitable as swelling-separation agent for cellulose whiskers if high temperature processing is used [91].

2.2.4. By electrostatic layer-by-layer

Electrostatic layer-by-layer self-assembled films have been exploited for the fabrication of sophisticated nanocomposite incorporated the linear polymer cellulose sulfate. In this method, a charged solid substrate is exposed to a solution of oppositely charged polyelectrolyte, followed by rinsing. The polymeric material adhering to the surface has more than the stoichiometric number of charges required for charge neutralization, thereby reversing the surface charge. This allows for easy adsorption of the next oppositely charged polyelectrolyte, also resulting in charge reversal. The amount of adsorbed polymer is self-limiting as a result of rinsing and allows for stepwise film growth [98, 99].

Resultant films and coatings show long-life stability as well as self-healing characteristics.

Structured layer-by-layer films have potential applications as antireflective coatings [100], waveguides, bio/optical sensors [101], separation technologies and drug delivery systems [102]. Conventionally, layer-by-layer assembly has employed solution-dipping (or dip-coating) in beakers of various sizes containing dilute aqueous polymer solutions. This inexpensive method works for most substrates independent of shape but has not always resulted in adequately homogeneous films. Alternatively, spin-coating is the most widely used technique for obtaining uniform films in lithography and other micromachining applications. The spin-coating process involves the acceleration of a liquid solution on a rotating substrate and is characterized by a balance of centrifugal forces (spin speed) and viscous forces (solution viscosity). Films created by this way have been found to be consistent and reproducible in thickness [103]. Nanocrystalline cellulose is amenable to sequential film growth by layer-by-layer assembly, as presented schematically in Figure 8.

Thin multilayered films incorporating polyelectrolyte layers such as poly (allylamine hydrochloride) and nanocrystalline cellulose layers were prepared by the electrostatic layer-by-layer methodology, as well as by a spin coating variant. Both techniques gave rise to smooth and stable thin films, as confirmed by atomic force microscopy surface morphology measurements as well as scanning electron microscopy investigations. Films prepared by spin-coating were substantially thicker than solution-dipped films. Thus both techniques are viable for producing structured nanocomposites, where the large aspect ratio cellulose units may serve to strengthen the elastic polymer matrix [93].

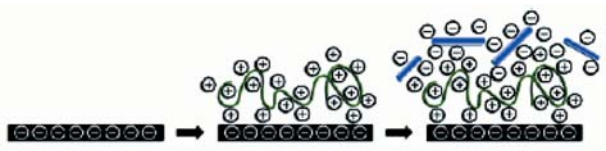

Figure 8. Schematic representation of the build-up of electrostatically adsorbed multilayered films. The polyelectrolyte, cationic poly(allylamine hydrochloride), is shown by the curved line and colloidal cellulose nanocrystals are represented by straight rods; counterions have been omitted for clarity

3. Characterization

Characterization of nanofibers and nanocomposites can be performed using different techniques such as transmission electron microscopy (TEM), X-ray and neutron diffraction, dynamic infrared spectroscopy, atomic force microscopy (AFM), differential scanning calorimetry (DSC), small angle neutron scattering (SANS), etc.

3.1. Nanoindentation techniques

Mechanical properties of materials have been commonly characterized using indentation techniques. Properties that are measured by indentation describe the deformation of the volume of material beneath the indenter (interaction volume). Deformation can be by several modes: elasticity, viscoealasticity, plasticity, creep, and fracture. These deformation modes are described by the following properties, respectively: elastic modulus, relaxation modulus, hardness, creep rate, and fracture toughness [2].

3.2. Microscopy characterization

Scanning electron microscopy (SEM) as well as atomic force microscopy (AFM) can be used for structure and morphologies determination of cellulose whiskers and their nanocomposites. From conventional bright-field transmission electron microscopy (TEM) it was possible to identify individual whiskers, which enabled determination of their sizes and shape. AFM overestimated the width of the whiskers due to the tip-broadening effect. Field emission SEM allowed for a quick examination giving an overview of the sample; however, the resolution was considered insufficient for detailed information.

By comparing TEM, Field emission scanning electron microscopy (FESEM) and AFM analysis of cellulose whiskers as in Figure 9, it is shown that; a) the whiskers did not differ significantly in contrast from the carbon film, b) it was difficult to clearly discern individual whiskers from agglomerated structures, and therefore an estimate of the width of the whiskers was not obtained while in, c) the structures differed from the needlelike shape as observed in TEM. The whiskers appeared significantly broader having a rounded shape. AFM could therefore be a powerful alternative to conventional

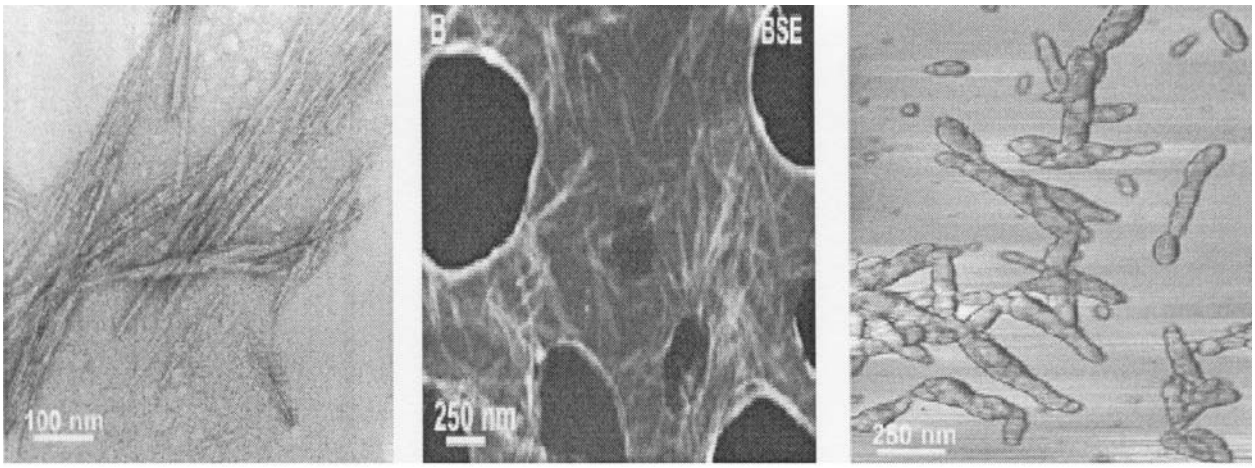

Figure 9. TEM, FESEM and AFM images of cellulose whiskers. a) Bright-field TEM image of stained cellulose whiskers on a porous carbon film, b) FESEM backscatter overview image of stained cellulose, c) AFM phase image of cellulose whiskers

bright-field transmission electron microscopy in such composite materials [104].

3.2.1. Small angle neutron scattering

Due to the sensitivity of this technique, this method was used for instance to investigate polymer layers grafted onto spherical particles with high specific area such as whisker, silica, latex particles or surfactants adsorbed onto ferrofluid particles [54, 105, 106].

3.3. X-ray diffractometry

The structural properties of the nanocomposite films can be characterized using X-ray diffraction like, the size of the cellulose crystallites [107] and crystallinity index [108].

3.4. Tensile tests

The nonlinear mechanical behavior of composites and unfilled matrix was analyzed using testing machine in tensile mode. The true strain ε was determined by the Equation (1):

$$\varepsilon = \ln \frac{L}{L_0} \tag{1}$$

where L and L_0 are the length of the specimen at the time of the test and the length at zero time, respectively.

The true stress σ was calculated by the Equation (2):

$$\sigma = \frac{F}{S} \tag{2}$$

where F is the applied load and S is the cross-sectional area at the time of the test.

From the stress-strain curves, the Young modulus (E) was determined from the slope of the low-strain region [21].

3.5. Electrical conductivity

For measuring ionic conductivities of ion-conducting solid polymer electrolytes or composites, the sample must be coated at their end with a silver paint to ensure a good electrical contact. Electrical conductivity measurements are performed at ambient temperature using several frequencies. The complex admittance is Y^* recorded versus time. From this admittance, the conductivity σ_c^* can be deduced by the Equation (3):

$$\sigma_c^* = Y^* \frac{L}{WT} = Y^* \frac{L^2}{V_0} \tag{3}$$

where W, L and T are the width, the length and the thickness of the sample during the test, and V_0 (the sample initial volume) = $L_0 \cdot T_0 \cdot W_0$ [58].

3.6. Transparency measurements

Transparency can be carried out using UV-visual spectrometry which gives the amount of light being transmitted trough the nanocomposite films at different wavelengthes [97].

3.7. Thermomechanical analysis

Thermomechanical measurements are perform using a thermomechanical analyzer. This analysis shows the temperature dependencies of a dynamic storage modulus [92].

3.8. Rheological behavior of suspensions

Rheological data could be collected with a rotating rheometer.

4. Applications

4.1. Cellulose–cellulose nanocomposites

Composite materials, typically glass fibers or carbon fibers embedded into epoxy resin or unsaturated polyester, show excellent mechanical and thermal properties; thus, they are widely used in various applications ranging from aerospace to vehicles to sports utensils [109]. However, these advantages cause environmental problems when disposing by incineration. Consequently, there are growing demands for environmentally friendly composites. Cellulose is the most abundant biomass resource and possesses excellent mechanical and thermal properties as mention before. Natural cellulose (cellulose I) also boasts an elastic modulus, E_l, of 138 GPa for the crystalline regions in the direction parallel to the chain axis. This is comparable with the E_l values of high performance synthetic fibers such as poly (phenylene terephthalamide) 130 GPa. In addition, the maximum macroscopic Young's modulus of natural plant cellulose (up to 128 GPa) is higher than those of aluminum (70 GPa) and glass fibers (76 GPa). The ultimate tensile strength of cellulose is estimated to be 17.8 GPa. This is 7 times higher than that of steel. Intrinsically, the very high elastic modulus and tensile strength (not specific modulus and specific strength) imply that cellulose possesses the potential to replace glass fiber, and it shows promise as a reinforcement fiber for composites where the density is not a concern. Current trends toward environmentally friendly composites focus on the use of cellulose fibers [110]. The interface between the fiber and the matrix often brings serious problems such as poor adhesion and water uptake by the composites. On the other hand, when the fiber and the matrix are composed of the same material, some benefits relevant to recyclability, and a better adhesion at interface, can be expected [111].

Cellulose is well known not to melt, but shows thermal degradation at high temperature. Therefore, to process cellulose, a wet process should be employed. Consequently, cellulose/cellulose composite was manufactured by the wet process using LiCl/N,N-dimethyl acetamide as cellulose solvent and by controlling the solubility of cellulose through pretreatment conditions. This composite is totally composed of sustainable cellulosic resources, so it can be biodegradable after service. Cellulose self-reinforced composite, possessed excellent mechanical and thermal properties during use as well as transparent to visible light. This composite can be used as an alternative of the glass-fiber-reinforced composite. By choosing the pretreatment condition to the fiber, the transverse mechanical properties of the composite can be also enhanced through the molecular diffusion across the interface between the fiber and the matrix [92, 111].

The ratio of cellulose I and II affects the properties of the resulting nanocomposites. So, cellulose-based nanocomposite films with different ratios of cellulose I and II were produced by partial dissolution of microcrystalline cellulose powder in LiCl/N,N-dimethyl acetamide and subsequent film casting. The films are isotropic, transparent to visible light, highly crystalline, and contain different amounts of un-dissolved cellulose I crystallites as a filler. By varying the cellulose I and II ratio, the mechanical performance of the nanocomposites can be tuned depending on the composition. Also, the nanocomposites clearly surpass the mechanical properties of most comparable cellulosic materials, their greatest advantage being the fact that they are fully biobased and biodegradable, but also of relatively high strength [92].

4.2. Nanocomposites from cellulose derivatives

The chemical modification of dissolving-grade wood pulp fibers with a variety of acids and anhydrides represents longstanding industrial practice. Cellulose ethers and cellulose esters are used for a wide variety of products in the food, household products, health care, textile, and many other industries. Esters with short alkyl chains (acetate or propionate) form solvent-soluble, spinnable fibers;

esters with bulky substituents (butyrate, hexanoate, and higher) are progressively more thermally deformable under pressure. Such cellulose ester powders in the presence of different plasticizers and additives are extruded to produce various grades of commercial cellulose plastics in palletized form [112, 113]. Among biopolymeric materials, cellulose and cellulose derivatives enjoy widespread use and remain the single largest biopolymer. In multiphase polymer materials, cellulose may find application in both polymeric blends and as fibers in reinforced polymeric composites. Recently, composite materials based on cellulose derivatives have been the subject of intense research.

Polymer nanocomposites are one of the important application areas for nanotechnology, as well as naturally derived organic nanophase materials are of special interest in the case of polymer nanocomposites. Nanocomposites have been successfully fabricated from cellulose acetate, triethyl citrate plasticizer, and organically modified clay Cloisite 30B with and without maleic anhydride grafted cellulose acetate butyrate as a compatibilizer. The cellulosic plastic with cellulose acetate/triethyl citrate (80/20 wt%) was used as the polymer matrix for nanocomposite fabrication. Cellulosic plastic-based nanocomposites obtained using increased pre-plasticizing times showed better exfoliated structures. In the system containing compatibilizer, the minimum retention time required for obtaining almost completely exfoliated hybrid nanocomposites was shorter than in the system without compatibilizer [114–118].

Cellulose diacetate films incorporated with small amount of montmorillonite nanoclay ($Al_4Si_8O_{20}(OH)_4 \cdot nH_2O$) were prepared from methylene chloride/ethanol (9:1 wt/wt) casting solutions. The various nanoclays were incorporated into the cellulose structure in order to enhance the mechanical properties as well as thermal stability of cellulose. The plasticizers used were: dibutyl phthalate, diethyl phthalate, poly (ethylene glycol). The films were completely transparent in the composition range of 10 to 30 w/w plasticizers and 1 to 7 w/w montmorillonite nanoclay. The strength of films decreased with the increase in the plasticizer content. All the films gave a single glass transition temperature, T_g, which decreased sharply from 180°C of the original cellulose diacetate to approximately 95°C according to the content and kind of plasticizer [119, 120]. When the plasticizer was added into the cellulose diacetate film up to 30 wt%, the Young's modulus of film was decreased from 1930 MPa to 1131 MPa but was increased from 1731 MPa to 2272 MPa when the montmorillonite nanofiller was added into the film up to 7 wt%. The mechanical properties of cellulose diacetate films were decreased by addition of plasticizer but strengthened by the incorporation of montmorillonite nanofiller. Also, nanocomposites were synthesized using cellulose acetate bioplastic, citrate based plasticizer and organically modified clay nanofillers. Transmission electron microscopy revealed the existence of intercalated clay dispersed throughout the cellulose acetate matrix. The intercalated reinforcements resulted in enhancements of the composite tensile strength, tensile modulus, and coefficient of thermal expansion. The composite tensile strength of cellulose acetate increased approximately 38% after incorporating 5 wt% clay. The tensile modulus was also enhanced as much as 33% [121].

Biodegradable cellulose acetate/layered silicate grafted poly(ε-caprolactone) nanocomposites were prepared by in situ polymerization of ε-caprolactone in the presence of cellulose acetate and organically modified layered silicate [122].

Nearly monodisperse nanoparticles have been synthesized based on a naturally occurring polymer of hydroxypropyl cellulose. The hydroxypropyl cellulose nanoparticle assembly in water has been further stabilized by covalently bonding neighboring particles to form a three-dimensional network. This network contains a large amount of water similar to a conventional bulk gel [123]. From morphology analysis of hydroxypropyl cellulose fibril reinforced nanocomposites using nanoindentation. It was observed that hydroxypropyl cellulose composite with a fibril showed lighter and darker structures that can be explained by a contrast of crystalline fibril areas and the amorphous polymer matrix. The direct use of aqueous fibril suspensions for the compounding with hydroxypropyl cellulose was found to be an effective method of dispersing the fibrils within the polymer matrix. The results show a homogeneous distribution of cellulose fibrils at higher magnifications [124].

Another less studied form of cellulose, microcrystalline cellulose, which is used in the production of pharmaceutical tablets as binding material and

compatibility enhancer. Borges *et al.* [125] produced and characterized composites based on a cellulose derivative, 2-hydroxypropylcellulose used as matrix and reinforced with microcrystalline cellulose fibers. As both the matrix and Avicel fibers have free hydroxyl groups in the anhydrogluclose units, they proposed a new way of elaborating these natural composites through the direct coupling between the fibers and the matrix. Different diisocyanates were used as coupling agents and the obtained composites presented improved mechanical properties as the result of a better fiber-matrix adhesion. In addition, the fibers concentration in the composite material used up to 30 w/w%. This means that, the inclusion of fibers in a hydroxypropylcellulose matrix produces composites with superior mechanical properties.

Carboxymethyl cellulose is a polyelectrolyte derived from natural materials. It has been extensively studied as a hydrogel polymer. The effect of nano-sized fillers on the properties of carboxymethyl cellulose-based composites is of interest in the development of novel or improved applications for hydrogel polymers in general and carboxymethyl cellulose in particular. The composite material composed of carboxymethyl cellulose, microcrystalline cellulose or cellulose nanocrystals, with glycerol as a plasticizer was prepared. Cellulose nanocrystals improved the strength and stiffness of the resulting composite compared to microcrystalline cellulose. In addition, a simple heat treatment was found to render the nanocomposite water resistant [126].

Ethyl cellulose/montmorilloniote nanocomposite film plasticized with environmental-friendly plasticizer epoxidized soybean oil was prepared by melt process using Haake mixer. The addition of 10 wt% epoxidized soybean oil causes a decrease of T_g from 81 to 61°C. When the plasticizer was added into the ethyl cellulose films, the mechanical properties of ethyl cellulose films was decreased, however the addition of montmorillonite into the ethyl cellulose films or the ring opening reaction of epoxidized soybean oil plasticizer cause enhancement of mechanical properties [127].

The reaction of dissolving-grade wood pulp fibers with a mixed *p*-toluenesulfonic/hexanoic acid anhydride system and a titanium (IV) isopropoxide catalyzed system under non-swelling reaction conditions produces fibers that represent biphasic cellulose derivatives. Transparent or semitransparent composite sheets can be formed in which the thermoplastic cellulose hexanoate phase is consolidated into a continuous matrix reinforced with discontinuous cellulose I domains. The cellulose I component also varies with the extent of modification, and it provides for biodegradability and reinforcement (i. e., high modulus). Although no precise dimensions can be determined for the respective phase domains, the low solubility of the products and the decrease in the crystal size of cellulose I suggest that they are on the nanometer scale. There are differences in some properties based on the difference in the distribution of subsistent between the materials generated by toluenesulfonic/hexanoic acid anhydride and the titanium (IV) isopropoxide catalyzed systems [107].

4.3. Cellulose–inorganic nanocomposites

The integration of polymers and inorganic materials is an attractive field in materials science. Unfortunately, because of the differences in their individual intermolecular interaction forces, the interfacial incompatibility between inorganic and organic polymers often causes failures in the preparation of these composites. The lack of affinity and hydrophobic polymers make it difficult for a homogeneous mixture to be achieved. Tourmaline, from singhalese tourmaline, a mixed stone, is a naturally complex group of hydrous silicate minerals containing Li, Al, B, and Si and various quantities of alkalis (K and Na) and metals (Fe, Mg, and Mn). It is the principle boron-containing mineral in the crust and has its genesis in both igneous (principally pegmatites) and metamorphic rocks. Its structural formula is $Na(Li,Al)_3Al_6(BO_3)_3Si_6O_{18}(OHF)_4$. Tourmaline forms hexagonal and prismatic crystals and possesses as antibacterial activity. On the other hand, the NaOH/thiourea aqueous system is hydrophilic, so it can be expected to disperse hydrophilic tourmaline nanoparticles. By using NaOH/thiourea aqueous solutions as cosolvents of cellulose and nanoparticles provides a simple, cheap, and pollution-free way of preparing such composite materials. By this way Dong *et al*. [128] prepared cellulose/tourmaline nanocomposites films via a casting method through coagulation with $CaCl_2$ and HCl aqueous solutions. Results indicated that adhesion between regenerated cellulose and filled nanocrystals can occur, and the dispersion of nanocrystals in cellulose is homoge-

neous but the induction of tourmaline breaks the partial intermolecular hydrogen bonds of cellulose, and this result in a reduction of the thermal stability of the composite films but composite films with tourmaline exhibit satisfying antibacterial action against Staphylococcus aureus. So, using NaOH/thiourea aqueous solutions as cosolvents of cellulose and nanoparticles provides a simple, cheap, and pollution-free way of preparing composite materials.

Suber *et al.* [129] study the synthesis and the comparative structural and morphological study of iron oxide nanoparticles in polystyrene-based ion-exchange resins and cellulose. The results show that the matrix influences the iron oxide particle size; the average size is about 7 nm in the resins and 25 nm in the cellulose. In the resins, particles are present inside the pores and as aggregates on the surface of the resin beads, whereas in the cellulose they are present on the surface and in the swollen network of the microfibers constituting the single fibers.

4.4. Starch nanocomposites

A number of researchers have presented work in the field of starch nanocomposites. Park *et al*. [131] reported on the preparation and properties of gelatinized starch/montmorillonite clay nanocomposites using both naturally occurring sodium montmorillonite and a number of alkyl ammonium modified clays. X-ray diffraction and transmission electron microscopy showed an intercalated structure for the starch/sodium montmorillonite, however the modified clays appeared either unchanged or agglomerated in structure [130]. Also they found that the unmodified sodium montmorillonite/starch nanocomposite also exhibited the greatest increase in modulus of all the clays used. Park *et al*. [132] also investigated the formation of montmorillonite-reinforced glycerol/plasticized thermoplastic starch. Scanning electron microscopy showed well-dispersed montmorillonite platelets. The Fourier-Transformed Infrared spectra indicated cooperation existed between montmorillonite and starch molecules and hydrogen bonds that formed between the reactive hydroxyl groups of montmorillonite and the hydroxyl groups of starch molecules. The mechanical and thermal properties of the starch nanocomposites formed showed significant improvements. Wilhelm *et al*. [133] have also investigated the formation of starch/clay nanocomposites, using a Ca^{2+} hectorite ($Mg_6Si_8O_{20}(OH)_4 \cdot nH_2O$). Solution cast starch/clay nanocomposites showed no X-ray diffraction due to the first basal spacing, indicating almost total exfoliation in the starch matrix. Although this was a good result, starch does require some kind of plasticizer to reduce the brittleness of the starches. When glycerol was added by itself to the clay, the interplanar distance increased. Fischer *et al*. [134, 135] also investigated starch/clay nanocomposites and a number of experimental pathways were investigated, including the dispersion of Na^+ montmorillonite clay in water, followed by blending in an extruder at a temperature of 85–105°C with a premixed powder of potato starch, glycerol and water. The resulting material appeared to be fully exfoliated and exhibited a reduction in hydrophilicity, and improved stiffness, strength and toughness.

The natural smectite clays, montmorillonite and hectorite, readily formed nanocomposites with thermoplastic starch which prepared by melt-processing of starch and glycerol [136]. In all cases, clay increased the elastic modulus of thermoplastic starch. The moduli of treated-hectorite and kaolinite composites were very similar at similar clay loadings and were lower than the nanocomposites, for nanocomposites, montmorillonite generally provided a slightly greater improvement in the modulus than untreated hectorite [137]. Another group of starch-based nanocomposites is those that are blended with biodegradable polyesters. McGlashan and Halley studied the dispersion of nanoclays in a number of different biodegradable starch/polyester blend formulations. The crystallization temperature of the nanocomposite blends was found to be significantly lower than the base blend, probably due to the clay platelets inhibiting order, and hence crystallization, of the starch and polyester. The best dispersions were found in the 30 wt% starch blends [138]. Kalambur and Rizvi [139] also investigated starch nanocomposites blends and successfully made starch/polylactic acid blends in the presence of montmorillonite nanoclay ($Al_4Si_8O_{20}(OH)_4 \cdot nH_2O$). By study the thermal stability of nanocomposites of starch/clay it is found that there is no significant effect of clay on the thermal degradation of starch, whereas a significant increase in thermal stability was observed when nanocomposites of thermoplastic starch and unmod-

ified montmorillonite was prepared by melt intercalation method even at 5% filler content. Thus, the preparation method might have an effect on the properties. Composites have been prepared by solution method after drying of starch and clay at 110°C. All composites show highest weight loss at 296°C. It was assumed that thermal degradation was influenced by hydroxyl group exposure, clay dispersion and reassociation of starch chains where clay dispersion was more important than others [140]. However, hydrophobic poly (lactic acid) and hydrophilic starch are thermodynamically immiscible, leading to poor adhesion between the two components, and hence poor and irreproducible performance. Various compatibilizers and additives have been investigated to improve the interfacial interactions of these blends. Wang *et al*. [141, 142] used methylenediphenyl diisocyanate to improve the interface and studied a blend of 55/45 w/w mixture of poly (lactic acid) and dried wheat starch in an intensive mixer with or without a low level of methylenediphenyl diisocyanate. Blends with methylenediphenyl diisocyanate had enhanced mechanical properties that could be explained by the in situ formation of a block copolymer acting as a compatibilizer. Scanning electron microscopy showed reduced interfacial tension between the two phases. The presence of methylenediphenyl diisocyanate also enhanced the mechanical properties of the blend at temperatures above T_g. Water uptake by the poly (lactic acid)/ starch blends with and without methylenediphenyl diisocyanate did not differ. Wang *et al*. [143] also studied the effect of starch moisture content on the interfacial interaction of an equal-weight blend of wheat starch and poly (lactic acid) containing 0.5% methylenediphenyl diisocyanate by weight. Starch moisture (10–20%) had a negative effect on the interfacial bonding between starch and poly (lactic acid). The tensile strength and elongation of the blend both decreased as starch moisture content increased. In blends of poly (lactic acid) /starch using dioctyl maleate as a compatibilizer markedly improved the tensile strength of the blend, even at low concentrations (below 5%). When dioctyl maleate functioned as a plasticizer at concentrations over 5%, significant enhancement in elongation was observed. Compatibilization and plasticization took place simultaneously according to the blends [144]. With dioctyl maleate as a polymeric plasticizer, thermal loss in the blends was not significant. Water absorption of poly (lactic acid)/starch blends increased with dioctyl maleate concentration. Other compatibilizers were also studied for the starch/poly (lactic acid) blends, such as poly (vinyl alcohol) [145] and poly(hydroxyester ether) [146] it was added to a starch and poly (lactic acid) blend (50/50, w/w) to enhance compatibility and improve mechanical properties.

4.5. Reinforcing agent for polymer electrolytes for lithium batteries application

Ion-conducting solid polymer electrolytes have attracted considerable interest, because of their potential application in rechargeable batteries, fuel cells, light-emitting electrochemical cells, electrochromics, and many other electrochemical devices [147–149]. Cellulose crystallites in the form of microcrystalline cellulose are currently utilized widely industrially. In the nanocomposite field, cellulose whiskers can be used as mechanical reinforcing agents of low-thickness polymer electrolytes for lithium batteries application but, the filler content is generally relatively low, below 10 wt%, avoiding significant decrease of the ionic conductivity. Nanocomposite polymer electrolytes based on high-molecular weight poly (oxy ethylene) were prepared from high aspect ratio cellulose nanocrystalline whiskers and lithium trifluoromethyl sulfonyl imide. The main effect of whisker is thermal stabilization of the modulus of composites above the melting point of the poly (oxy ethylene)/lithium trifluoro methyl sulfonyl imide complexes. The filler provides a high reinforcing effect, while a high level of ionic conductivity is retained with respect to unfilled polymer electrolytes. So the ionic conductivity was quite consistent with the specifications of lithium batteries [150, 151].

To study the effect of cellulose whiskers on mechanical properties of nanocomposite an aqueous suspension of high aspect ratio rod-like cellulosic particles composed of tunicin whiskers and a poly (oxy ethylene) aqueous solution casted in a Petri dish. After water evaporation a solid composite film was obtained, the mechanical behavior of tunicin whiskers/poly (oxy ethylene) nanocomposites was evaluated in the linear range over a broad temperature range from dynamic mechanical analysis. The main effect of the filler was a thermal sta-

bilization of the storage modulus for the composites above the melting temperature of the poly (oxy ethylene) matrix. It was shown that the formation of the cellulosic network through inter-whiskers hydrogen bonds, assumed to be responsible for the high mechanical properties of the composites, was not affected by the matrix crystallization process and filler/poly (oxy ethylene) interactions [152]. The incorporation of liquid compounds like plasticizers into the polymer electrolytes improves the ionic conduction. It generally results from the decrease of glass transition temperature of the complex, the reduction of crystallinity, the increase of salt dissociation capability and the rise of charge carrier diffusions. However, a decrease in mechanical strength of the resulting polymer electrolytes is predictable. Different plasticizers were used to enhance the conductivity. Plasticizers generally consist of low molecular weight organic molecules like propylene carbonate, ethylene carbonate, dimethyl carbonate, dioctyl phthalate, etc. An efficient plasticizer must display several properties: miscibility with poly (oxy ethylene), low viscosity, low volatility, electrochemical stability and high capability to solvate lithium salts. Low molecular weight poly (ethylene glycols) have chemical structure similar to that of poly (oxy ethylene), are thermally stable and can solvate lithium salts. To obtain new nanocomposite polymer electrolytes with both improved mechanical properties and improved conductivities, Azizi *et al*. [153] studied, poly (oxy ethylene)-lithium trifluoromethyl sulfonyl imide-based polymer electrolyte with tetra(ethylene) glycol dimethyl ether as plasticizer and cellulose whiskers as nanometric filler. The plasticizer induces both a loss of mechanical stiffness in the rubbery state of poly (oxy ethylene) and an increase of the ionic conductivity of the electrolyte. For salt-free systems and polymer electrolytes based on poly (oxy ethylene), a high reinforcing effect was observed above T_g of poly (oxy ethylene) when adding a low amount of tunicin whiskers. In addition, the filler provides a thermal stabilization effect of the material above the melting of poly (oxy ethylene). Both phenomena were ascribed to the formation of a rigid cellulosic network within the matrix as well as the conduction performances were similar for unplasticized and unfilled electrolytes on the one hand and plasticized filled systems on the other hand. Therefore, the later allows conciliating good ionic conductivities and high mechanical performances.

The processing of a composite polymer electrolyte from an aqueous suspension of cellulose whiskers is not easy to consider since water can react with the negative electrode and reduce the battery cycle life. On the other hand, cellulose whiskers are very difficult to disperse in a polymeric matrix as they have a large surface area and possess large hydrogen forces among themselves. It can lead to the formation of strongly bound aggregates. A surfactant can be used to disperse cellulose whiskers in a non-polar solvent [39, 54] like toluene. However, the large amount of surfactant necessary to maintain the stability of the suspension, due to the high specific area of the filler, prevents the use of this technique for composites processing in organic solvents. Another way is the surface chemical modification of cellulose whiskers to disperse cellulose whiskers in organic solvents [56] but, the mechanical performances of the resulting composites strongly decrease after chemical modification. Azizi *et al*. [21] prepared nanocomposite film reinforced with tunicin whiskers from a *N*,*N*-dimethylformamide as an organic solvent without a surfactant addition or a chemical surface modification. Both the high value of the dielectric constant of dimetyl formamide and the medium wettability of tunicin whiskers were supposed to control the stability of the suspension. The nanocomposite materials were prepared by UV cross-linking; with thermally stable photoinitiator, 4-(2-hydroxyethoxy)-phenyl-(2-hydroxy-2-propyl) ketone, using an unsaturated polyether as matrix.

Cross-linking is one of the most common methods used to disrupt polymer crystallinity and to ensure mechanical properties. It is classically performed to provide both low-temperature conductivity and high-temperature mechanical stability. In comparing the behavior of weakly cross-linked poly ether α,ω-dihydroxyoligo(oxyethylene) filled with tunicin whiskers suspended in *N*,*N*-dimethylformamide and the one of unfilled materials exhibiting different cross-linking density. The cellulosic nanofiller provided a much higher reinforcing effect at high temperature than the cross-linking process, a photoinitiator, 4-(2-hydroxyethoxy) phenyl-(2-hydroxy-2-propyl) ketone used as cross-linking agent. In addition, nanocomposite electrolytes display a higher ionic conductivity on the whole temperature range due to the high crosslinking density that

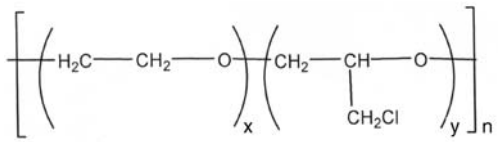

Figure 10. Chemical structure of ethylene oxide-epichlorohydrin coploymer

should be used for unfilled electrolytes in order to ensure satisfactory mechanical properties. It was also shown that tunicin whiskers seem to have no effect on the conduction mechanism of the polymer electrolyte. Therefore, the used cross-linked nanocomposite polymer electrolytes allow conciliating both higher ionic conductivities and higher mechanical performances [154]. Lithium perchlorate-doped nanocomposites of ethylene oxide-epichlorohydrin copolymers and cellulose whiskers can readily be produced by solution casting tetrahydrofuran/water mixtures comprising the components and subsequent compression molding of the resulting nanocomposites. Films of these materials display substantially improved mechanical properties, when compared to the not reinforced lithium perchlorate/ethylene oxide-epichlorohydrin (Figure 10), and their electrical conductivities experience comparably small reductions [90].

High performance solid lithium-conducting nanocomposite polymer electrolytes based on poly (oxy ethylene) were prepared from high aspect ratio cellulosic whiskers and lithium trifluoro methane sulfonyl imide. The filler provided a high reinforcing effect while a high level of ionic conductivity was retained with respect to the unfilled polymer electrolytes [155, 156].

4.6. In biomedical

From a biological viewpoint, almost all of the human tissues and organs are deposited in nanofibrous forms or structures. Examples include: bone, dentin, collagen, cartilage, and skin. All of them are characterized by well organized hierarchical fibrous structures. In biomedical applications, for soft tissue replacement a developed material that will not only display similar mechanical properties as the tissue it is replacing, but also shows improved life span, biocompatibility, nonthrombogenic, and low degree of calcification needed. Hydrophilic bacterial cellulose fibers of an average diameter of 50 nm are produced by the bacterium Acetobacter xylinum, using a fermentation process. They can be used in combination with poly (vinyl alcohol) to form biocompatible nanocomposites. Millon *et al*. [157] prepared poly (vinyl alcohol)/bacterial cellulose nanocomposites and they found that, the resulting nanocomposites possess a broad range of mechanical properties and can be made with mechanical properties similar to that of cardiovascular tissues, such as aorta and heart valve leaflets.

Silk fibroin-microcrystalline cellulose (cellulose whisker) composite films with varied compositions were prepared by casting mixed aqueous solution/suspensions of the two components. Silk fibroin was dissolved in lithium thiocyanate followed by dialysis; a cellulose whisker suspension was prepared by sulfuric acid hydrolysis of tunicate cellulose. Composite films showed improved mechanical strength at 20–30 wt% fibroin content, with breaking strength and ultimate strain about five times those of the constituent materials. From the observed shift in the infrared absorption bands of amide I and amide II of fibroin, the anomaly in the mechanical strength is considered to arise from the contact of fibroin with the highly ordered surface of cellulose whiskers. This phenomenon is not practicable for producing bulk materials because of the lengthy procedure of solubilization and dialysis involved, but may be useful in biomedical applications such as for cell culture media and implant materials, since both components are chemically inert and known to be compatible with living tissues [158]. Hydroxyapatite ($Ca_{10}(PO_4)_6(OH)_2$)-bacterial cellulose as a novel class of nanocomposites were prepared by Wan *et al*. [159, 160]. The structure characterizing reveals that the crystallite sizes of the hydroxyapatite crystals are nano-sized and their crystallinities are low. The Fourier-Transformed Infrared spectroscopy results show that hydroxyapatite crystals are formed when the phosphorylated and $CaCl_2$-treated bacterial cellulose fibers are soaked in a 1.5 simulated body fluid the hydroxyapatite crystals are partially substituted with carbonate, resembling natural bones. The nanocomposites containing hydroxyapatite with structural features close to those of biological apatites are attractive for applications as artificial bones. From the scheme, it is believed that the non-ionic hydroxyl groups on the unphosphorylated bacterial cellulose may firstly bind the calcium ions

through ionic-dipolar interaction, and then hydroxyapatite crystals grow around these trapped ions.

The process is schematically displayed in Figure 11a. However, a different process is involved for the phosphorylated bacterial cellulose. As shown in Figure 11b, esterification takes place during phosphorylation and thus anionic phosphate groups are bonded to the cellulose chain through strong covalent bonds. The negatively charged phosphate groups are capable of trapping calcium ions, forming calcium phosphate complexes that act as nuclei of hydroxyapatite and hydroxyapatite grows by further complexation with phosphate ions in SBF as shown in Figure 11c. Note that the bonding between the calcium ions and bacterial cellulose chain is via strong ionic bonds for the phosphorylated bacterial cellulose while the calcium ions complexation with nonionic hydroxyl groups proceeds via ionic-dipolar interaction for the unphosphorylated bacterial cellulose (Figure 11a). An organic-mineral composite of hydroxyapatite ($Ca_{10}(PO_4)_6(OH)_2$) nanoparticles and

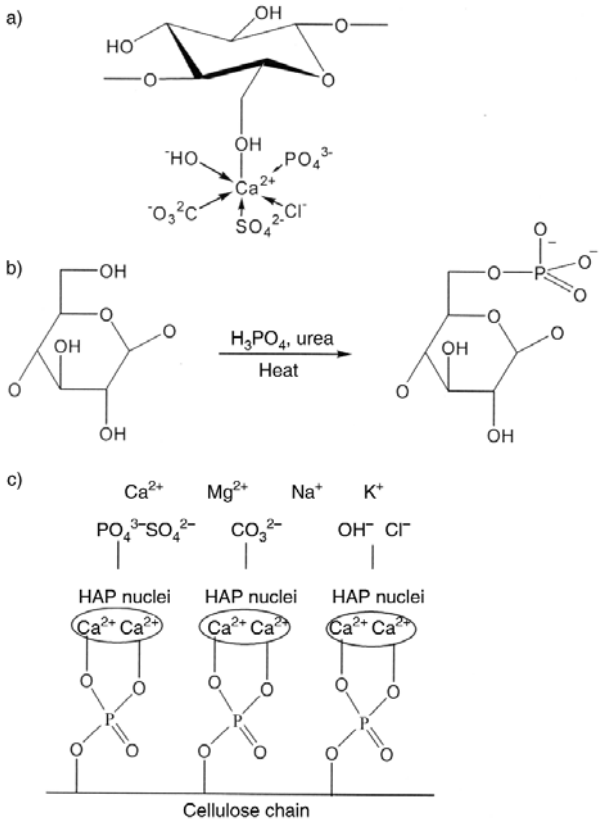

Figure 11. Schematic diagrams of various interaction processes. a) Hydroxyapatite growth on unphosphorylated bacterial cellulose, b) Phosphorylation of bacterial cellulose, c) Hydroxyapatite growth on phosphorylated bacterial cellulose (HPA = Hydroxyapatite)

carboxymethyl cellulose is synthesized via coprecipitation from a solution containing $CaCl_2$, aqueous ammonia, $(NH_4)_2HPO_4$, and carboxymethyl cellulose. The hydroxyapatite nanoparticles are shown to form agglomerates about 200 nm in size. The interaction between the nanoparticles and carboxymethyl cellulose macromolecules leads to the formation of a pore structure potentially attractive for biomedical applications [161].

4.7. In papers industry

The pulp and paper industry is a materials industry. It provides materials for use in communications, packaging, consumer products, and other products. The intersection of wood fiber-based materials with nano-materials provides nearly unlimited opportunities for the pulp and paper industry to develop new products with enhanced functionality and greater value. Paper in itself provides an excellent platform for developing nano-material fiber composites for use in higher value printing, barrier packaging, and intelligent communications media.

TiO_2/cellulose nanocomposites were prepared through the titanyl sulphate hydrolysis in acidic medium in the presence of cellulosic fibers in specific experimental conditions, the cellulose fibers promote the nucleation and growth of TiO_2 particles, yielding hybrid materials containing up to 46% TiO_2. Two series of paper handsheets having distinct TiO_2 content have been prepared, one from a selected hybrid composition and the other from mixtures of commercial TiO_2 and cellulose fibers. Comparative optical studies performed on the paper handsheets revealed a much higher opacity for the synthetic sample [162].

The pore structure of the cell wall of the never-dried pulp fibers has been identified as a general micropackaging or encapsulation system for a broad range of both organic and inorganic chemicals [163–166] these substances are entrapped in the cellulosic fiber matrix during the collapse of the cell wall pores as the pulp is dried [167]. Fahmy *et al.* [168] used sucrose as the nanoadditive to the mercerized non-dried cotton linter fibers. Relative to the sucrose-free paper, the sucrose-containing counterparts exhibit greater breaking length and remarkably high water uptake up to a sucrose content of 8–15% w/w.

4.8. In packing

In cellulose-based base material (e.g., copier paper or packing); a cellulose particles in nano-size range can be obtained from starting product containing cellulose (e.g., wood) by mixing with water; the mixture is heated, so that the product containing cellulose is hydrolyzed; the mixture then undergoes a shearing process giving base material and the base material is added to another solid- or liquid material-containing fiber substances [169]. On the other hand, biodegradable polymers such as starch [170, 171] poly (lactide) [172, 173] and poly (ε-caprolactone) [174–176] have attracted considerable attention in the packaging industry. In addition poly (lactic acid) is biodegradable thermoplastic polyester produced from L-lactic acid, which is derived from the fermentation of corn starch. Poly (lactic acid) is becoming increasingly popular as a biodegradable engineering plastic owing to its high mechanical strength and easy processability compared to other biopolymers [177]. It has gained enormous attention as a replacement for conventional synthetic packaging materials in the last decade [178] but the problem is the amount of transmitter light through the poly (lactic acid) sheet, for reducing this transmitter light, bentonite a layered silicate and microcrystalline cellulose chosen as nanoreinforcement for poly (lactic acid).

By comparing the mechanical, thermal and barrier properties of two different types of biopolymer based nanocomposites such as, bentonite a layered silicate and microcrystalline cellulose. The polymer matrix used was poly (lactic acid), a common available biopolymer. The bentonite nanocomposite showed great improvements in both tensile modulus and yield strength, while the microcrystalline cellulose nanocomposite only showed tendencies to improve the yield strength. There are a few factors that will help to explain these differences. First of all, the bentonite added to the poly (lactic acid)/bentonite material has theoretically twice the surface area of the added swelled microcrystalline cellulose. A larger surface area will allow the nanoreinforcement to interact with a larger amount of polymer chains and thereby having a larger effect on the mechanical properties. Secondly, the bentonite clay is organically modified to be compatible with polymers like poly (lactic acid) and will therefore have better interaction with the poly (lactic acid) matrix. Good interaction between the reinforcing phase and the matrix in a composite will allow for good stress transfer to take place in the composite. This gives rise to large improvements in the mechanical properties of the weaker matrix.

Also these two nanoreinforcements would affect poly (lactic acid) as a packaging material. The results showed a reduction in the oxygen permeability for the bentonite nanocomposite, but not for the microcrystalline cellulose nanocomposite. The amount of light being transmitted through the nanocomposites was reduced compared to pure poly (lactic acid) indicating that both nanoreinforcements were not fully exfoliated. [97].

4.9. Nanotechnology and wood as a building materials

Half of the wood products now used in construction are engineered wood composites. Nanotechnology will result in a unique next generation of wood-based products that have hyper-performance and superior serviceability when used in severe environments. They will have strength properties now only seen with carbon-based composites materials, and they will be both durable while in service and biodegradable after their useable service-life. Nanotechnology will also promote the development of intelligent wood- and biocomposite products with an array of nanosensors built in. Building functionality onto lignocellulosic surfaces at the nanoscale could open new opportunities for such things as self- sterilizing surfaces, internal self-repair and electronic lignocellulosic devices. The high strength of nanofibrillar cellulose together with its potential economic advantages will offer the opportunity to make lighter weight, strong materials with greater durability [5]. However, as in all markets, technology and shifting demographics give rise to hanging market demands. Materials and products used in housing construction are not immune to such changes. Because a home or a commercial building is typically the largest purchase a family will make and one of the larger investments a corporation will make, consumers want structures that maintain their value over time and are safe and secure, healthy, comfortable, long-lasting (durable), low maintenance, affordable (lower in cost and providing more value for the dollar), easily adaptable to new and modified architectural designs, and allow for personalized customization, have smart system

capabilities, and reduce costs for heating and air conditioning.

Wood-based construction materials function extremely well under a variety of end-use conditions. Under wet conditions, however, they can be prone to decay, mold, mildew, and insect attack. Wood can be protected from biodeterioration by treatments using toxic chemicals or by maintaining low moisture content in wood. Achieving control of moisture is a major opportunity for nanotechnology to aid in preventing biodeterioration of wood and wood-based materials. New non- or low-toxicity nanomaterials such as nanodimensional zinc oxide, silver, titanium dioxide, and even possibly clays might be used as either preservative treatments or moisture barriers. In addition, resistance to fire might be enhanced by use of nanodimensional materials like titanium dioxide and clays.

Composites allow an array of disparate materials with greatly differing properties to be engineered into products matched to end-user needs and performance requirements. For example, future nanocomposite construction materials may use combinations of wood, wood fiber, plastics, steel, and concrete. To achieve this, it will be necessary to be able to make hydrophilic materials compatible with hydrophobic materials such as wood and plastics [179].

5. Conclusions

Nanotechnology presents a tool to extend structural performance and serviceability by orders of magnitude. Nanotechnology will allow engineers and scientists to manipulate and systematically eliminate the formation of random defects that now dictate the properties, performance, and serviceability of biocomposites as known today. This new ability to minimize and eliminate naturally occurring and human-made internal defects will allow realizing the true potential of biomaterials. Nanotechnology will help the ability of manipulate and control fiber-to-fiber bonding at a microscopic level, and it will also offer an opportunity to control nanofibrillar bonding at the nanoscale. Nanocomposites will be the new frontier. So, understanding the synthesis-structure-property relationship of nanocomposites is vital for the development of advanced polymer nanocomposites with enhanced mechanical strength, stiffness and toughness for structural engineering applications.

In the nanocomposite field, cellulose whiskers can be used as mechanical reinforcing agents of low-thickness polymer electrolytes for lithium batteries application but, the filler content is generally relatively low, below 10 wt%, avoiding significant decrease of the ionic conductivity. But using aqueous suspension of cellulose whiskers is not easy to consider since water can react with the negative electrode and reduce the battery cycle life. On the other hand, a surfactant can be used to disperse cellulose whiskers in a nonpolar solvent like toluene. However, the large amount of surfactant necessary to maintain the stability of the suspension, due to the high specific area of the filler, prevents the use of this technique for composites processing in organic solvents. Another way is the surface chemical modification of cellulose whiskers to disperse cellulose whiskers in organic solvents but, the mechanical performances of the resulting composites strongly decrease after chemical modification. Nanocomposites reinforced with cellulose whisker suspended in organic solvent without surfactant addition or surface modification lead to high ionic conductivities and high mechanical performances.

Wood can be protected from biodeterioration by treatments using toxic chemicals or by maintaining low moisture content in wood. Achieving control of moisture is a major opportunity for nanotechnology to aid in preventing biodeterioration of wood and woodbased materials. New non- or low-toxicity nanomaterials such as nanodimensional zinc oxide, silver, titanium dioxide, and even possibly clays might be used as either preservative treatments or moisture barriers. In addition, resistance to fire might be enhanced by use of nanodimensional materials like titanium dioxide and clays.

Future nanocomposite construction materials may use combinations of wood, wood fiber, plastics, steel, and concrete. To achieve this, it will be necessary to be able to make hydrophilic materials compatible with hydrophobic materials such as wood and plastics.

References

[1] Wegner T. H., Jones P. E.: Advancing cellulose-based nanotechnology. Cellulose, **13**, 115–118 (2006).

[2] Moon R. J., Frihart C. R., Wegner T. H.: Nanotechnology applications in the forest products industry. Forest Products Journal, **56**, 4–10 (2006).

[3] Gabriel A. S.: Introduction to nanotechnology and its applications to medicine. Surgical Neurology, **61**, 216–220 (2004).
[4] Schmidt D., Shah D., Giannelis E. P.: New advances in polymer/ layered silicate nanocomposites. Current Opinion in Solid State and Materials Science, **6**, 205–212 (2002).
[5] Wegner T. H., Winandy J. E., Ritter M. A.: Nanotechnology opportunities in residential and non-residential construcxtion. in '2nd International Symposium on Nanotechnology in Construction, Bilbao, Spain' (2005).
[6] Moon R. J., Frihart C. R., Wegner T. W.: Nanotechnology applications in the forest products industry. Forest Products Journal, **56**, 4–10 (2006).
[7] Alexandre M., Dubois P.: Polymer-layered silicate nanocomposites: preparation, properties and uses of a new class of materials. Materials Science and Engineering, Reports, **28**, 1–63 (2000).
[8] Okada A., Kawasumi M., Toyotak K., Kamigaito O.: Synthesis and characterization of a nylon 6 clay hybrid. Polymer Preprints, **28**, 447–458 (1987).
[9] Usuki A., Kojima Y., Kawasumi M., Okada A., Fukushima Y., Kurauchi T., Kamigaito O.: Synthesis of nylon 6-clay hybrid. Journal of Material Research, **8**, 1179–1184 (1993).
[10] Yano K., Usuki A., Okada A., Kurauchi T., Kamigaito O.: Synthesis and properties of polymide-clay hybrid. Journal of Polymer Science, Part A: Polymer Chemistry, **31**, 2493–2498 (1993).
[11] Chazeau L., Gauthier C., Vigier G., Cavaillé J-Y.: Relashionships between microstructural aspects and mechanical properties of polymer-based nanocomposites. in 'Handbook of Organic-Inorganic Hybrid Materials and Nanocomposites' (ed.: Nalwa H. S.), American Scientific Publishers, Los Angles (2003).
[12] Damas F., Cavaillé J-Y., Gauthier C., Chazeau L., Dendievel R.: Viscoelastic behavior and electrical properties of flexible nanofiber filled polymer nanocomposites. influence of processing conditions. Composites Science and Technology, **67**, 829–839 (2007).
[13] Eichhorn S. J., Baillie C. A., Zafeiropoulos N., Mwaikambo L. Y., Ansell M. P., Dufresne A., Entwistle K. M., Herrera-Franco P. J., Escamilla G. C., Groom L., Hughes M., Hill C., Rials T. G., Wild P. M.: Current international research into cellulosic fibers and composites. Journal of Materials Science, **36**, 2107–2131 (2001).
[14] Page D. H., El-Hosseiny F., Winkler K.: Behaviour of single wood fibres under axial tensile strain. Nature, **229**, 252–253 (1971).
[15] Shchniewind A. P.: Concise encyclopedia of wood & wood-based materials. Pergamon, Oxford (1989).
[16] Eichhorn S. J., Young R. J.: The Young's modulus of a microcrystalline cellulose. Cellulose, **8**, 197–207 (2003).
[17] Sjöström E.: Wood chemistry fundamentals and applications. Academic Press, New York (1993).
[18] Mathew A. P., Dufresne A.: Morphological investigation of nanocomposites from sorbitol plasticized starch and tunicin whiskers. Biomacromolecules, **3**, 609–617 (2002).
[19] Morin A., Dufresne A.: Nanocomposites of chitin whiskers from riftia tubes and poly (caprolactone). Macromolecules, **35**, 2190–2199 (2002).
[20] Hamad W.: Cellulosic materials, fibers, networks and composites. Kluwer Academic Publishers, Boston (2002).
[21] Azizi Samir M. A. S., Alloin F., Sanchez J-Y., El-Kissi N., Dufresne A.: Preparation of cellulose whiskers reinforced nanocomposites from an organic medium suspension. Macromolecules, **37**, 1386–1393 (2004).
[22] Helbert W., Cavaillé J-Y., Dufresne A.: Thermoplastic nanocomposites filled with wheat straw cellulose whiskers. Part I: Processing and mechanical behavior. Polymer Composites, **17**, 604–611 (1996).
[23] O'Sullivan A. C.: Cellulose: the structure slowly unravels. Cellulose, **4**, 173–207 (1997).
[24] Hakansson H., Ahlgren P.: Acid hydrolysis of some industrial pulps: effect of hydrolysis conditions and raw material. Cellulose, **12**, 177–183 (2005).
[25] Battista O. A., Smith P. A.: Microcrystalline cellulose. Industrial and Engineering Chemistry, **54**, 20–29 (1962).
[26] Iijima H., Takeo K.: Microcrystalline cellulose: An overview. in 'Handbook of Hydrocolloids' (eds.: Phillips G. O., Williams P. A.) Woodhead Publishing Limited, Cambridge, **Ch19**, 331–346 (2000).
[27] Revol J. F., Bradford H., Giasson J., Marchessault R. H., Gray D. G.: Helicoidal self-ordering of cellulose microfibrils in aqueous solution. International Journal of Biological Macromolecule, **14**, 170–172 (1992).
[28] Araki J., Wada M., Kuga S., Okano T.: Flow properties of microcrystalline cellulose suspension prepared by acid treatment of native cellulose. Colloids and Surfaces, **142**, 75–82 (1998).
[29] de Rodriguez N. L. G., Thielemans W., Dufresne A.: Sisal cellulose whiskers reinforced polyvinyl acetate nanocomposites. Cellulose, **13**, 261–270 (2006).
[30] Whistler R. L., BeMiller J. M.: Carbohydrate chemistry for food scientists. American Association of Cereal Chemists, St Paul (1997).
[31] El-Sakhawy M., Hassan M. L.: Physical and mechanical properties of microcrystalline cellulose prepared from local agricultural residues. Carbohydrate Polymers, **67**, 1–10 (2007).
[32] Bondeson D., Mathew A., Oksman K.: Optimization of the isolation of nanocrystals from microcrystalline cellulose by acid hydrolysis. Cellulose, **13**, 171–180 (2006).
[33] Stromme M., Mihranyan A., Ek R.: What to do with all these algae? Materials Letters, **57**, 569–572 (2002).
[34] Dufresne A., Cavaillé J-Y., Vignon M. R.: Mechanical behavior of sheet prepared from sugar beet cellulose microfibrils. Journal of Applied Polymer Science, **64**, 1185–1894 (1997).

[35] Gopalan N. K., Dufresne A., Gandini A., Belgacem M. N.: Crab shell chitin whisker reinforced natural rubber nanocomposites. 3. Effect of chemical modification of chitin whiskers. Biomacromolecules, **4**, 1835–1842 (2003).

[36] Gopalan N. K., Dufresne A.: Crab shell chitin whisker reinforced natural rubber nanocomposites. 1. Processing and swelling behavior. Biomacromolecules, **4**, 657–665 (2003).

[37] Dufresne A., Vignon M. R.: Improvement of starch film performances using cellulose microfibrils. Macromolecules, **31**, 2693–2696 (1998).

[38] Dufresne A., Dupeyre D., Vignon M. R. Cellulose microfibrils from potato tuber cells: Processing and characterization of starch-cellulose microfibril composites. Journal of Applied Polymer Science, **76**, 2080–2092 (2000).

[39] Heux L., Chauve G., Bonini C.: Nonocculating and chiral-nematic self-ordering of cellulose microcrystals suspensions in nonpolar solvents. Langmuir, **16**, 8210–8212 (2000).

[40] Favier V., Dendievel R., Canova G., Cavailé J. Y., Gilormini P.: Simulation and modeling of three-dimensional percolating structures: case of a latex matrix reinforced by a network of cellulose fibers. Acta Materiala, **45**, 1557–1565 (1997).

[41] Terech P., Chazeau L., Cavaillé J-Y.: A small-angle scattering study of cellulose whiskers in aqueous. suspensions. Macromolecules, **32**, 1872–1875 (1999).

[42] Dufresne A., Kellerhals M. B., Witholt B.: Transcrystallization in mcl-PHAs/cellulose whiskers composites. Macromolecules, **32**, 7396–7401 (1999).

[43] De Souza Lima M. M., Wong J. T., Paillet M., Borsali R., Pecora R.: Translational and rotational dynamics of rodlike cellulose whiskers. Langmuir, **19**, 24–29 (2003).

[44] Chazeau L., Paillet M., Cavaillé J-Y.: Plasticized PVC reinforced with cellulose whiskers. I. Linear viscoelastic behavior analyzed through the quasi-point defect theory. Journal of Polymer Science, Part B: Polymer Physics, **37**, 2151–2164 (1999).

[45] Dong X. M., Revol J-F., Gray D. G.: Effect of microcrystallite preparation conditions on the formation of colloid crystals of cellulose. Cellulose, **5**, 19–32 (1998).

[46] Araki J., Wada M., Kuga S.: Steric stabilization of a cellulose microcrystal suspension by poly (ethylene glycol) grafting. Langmuir, **17**, 21–27 (2001).

[47] Isogai A., Kato Y.: Preparation of polyuronic acid from cellulose by TEMPO-mediated oxidation. Cellulose, **5**, 153–164 (1998).

[48] Araki J., Wada M., Kuga S., Okano T.: Influence of surface charges on viscosity behavior of cellulose microcrystal suspension. Journal of Wood Science, **45**, 258–261 (1999).

[49] Milewski J. V.: Whiskers. in 'Concise Encyclopedia of Composite Materials' (ed.: Kelly A.) Pergamon, New York, 311–314 (1994).

[50] Favier V., Chanzy H., Cavaillé J-Y.: Polymer nanocomposites reinforced by cellulose whiskers. Macromolecules, **28**, 6365–6367 (1995).

[51] Favier V., Canova G. R., Cavaillé J-Y., Chanzy H., Dufresne A., Gauthier C. Nanocomposite materials from latex and cellulose whiskers. Polymers for Advanced Technologies, **6**, 351–355 (1995).

[52] Ruiz M. M., Cavaillé J-Y., Dufresne A., Graillat C., Gerard J-F.: New waterborne epoxy coating based on cellulose nanofillers. Die Makromolekulare Chemie, **169**, 211–222 (2001).

[53] Grunert M., Winter T. W.: Nanocomposites of cellulose acetate butyrate reinforced with cellulose nanocrystals. Journal of Polymers and the Environment, **10**, 27–30 (2002).

[54] Bonini C., Heux L., Cavaillé J-Y., Lindner P., Dewhurst C., Terech P.: Rodlike cellulose whiskers coated with surfactant: A small-angle neutron scattering characterization. Langmuir, **18**, 3311–3314 (2002).

[55] Yuan H., Nishiyama Y., Wada M., Kuga S.: Surface acylation of cellulose whiskers by drying aqueous emulsion. Biomacromolecules, **7**, 696–700 (2006).

[56] Gousse C., Chanzy H., Excofier G., Soubeyrand L., Fleury E.: Stable suspensions of partially silylated cellulose whiskers dispersed in organic solvents. Polymer, **43**, 2645–2651 (2002).

[57] Ruiz M. M., Cavaillé J-Y., Dufresne A., Graillat C.: New waterborne epoxy coatings based on cellulose nanofillers. Macromolar Symposia, **169**, 211–222 (2001).

[58] Florent D., Chazeau L., Gauthier C., Cavaillé J-Y., Remy D.: Large deformation mechanical behavior of flexible nanofiber filled polymer nanocomposites. Polymer, **47**, 2802–2812 (2006).

[59] Lukic B., Seo. J. W., Couteau E., Lee K., Gradecak S., Berkecz R., Hernadi K., Delpeux S., Cacciaguerra T., Béguin F., Fonseca A., Nagy J. B., Csányi G., Kis A., Kulik A. J., Forró L.: Elastic modulus of multi-walled carbon nanotubes produced by catalytic chemical vapour deposition. Applied Physics A: Materials Science and Processing, **80**, 695–700 (2005).

[60] Malainine M. E., Mahrouz M., Dufresne A.: Thermoplastic nanocomposites based on cellulose micro fibrils from opuntia ficus-indica parenchyma cell. Composites Science and Technology, **65**, 1520–1526 (2005).

[61] Ljungberg N., Cavaillé J-Y., Heux L.: Nanocomposites of isotactic polypropylene reinforced with rod-like cellulose whiskers. Polymer, **47**, 6285–6292 (2006).

[62] Colvin J. R., Leppard G. G.: The biosynthesis of cellulose by Acetobacter xylinum and Acetobacter acetigenus. Canadian Journal of Microbiology, **23**, 701–709 (1977).

[63] White D. G., Brown R. M. J.: Prospects for the commercialization of the biosynthesis of microbial cellulose. in 'Cellulose and Wood-Chemistry and Technology', Schuerech, C., Ed., John Wiley and Sons, New York. (1989).

[64] Williams, W. S., Cannon, R. E.: Alternative environmental roles for cellulose produced by acetobacter xylinum. Applied and Environmental Microbiology, **55**, 2448–2452 (1989).
[65] Brown R. M. Jr.: Bacterial cellulose. in 'Cellulose: Structural and Functional Aspects' (eds. Kennedy, Phillips G. O., Williams P. A.) Ellis Horwood Ltd., Chirchester, 145–151 (1989).
[66] Yamanaka S., Watanabe K., Kitamura N., Iguchi M., Mitsuhashi S., Nishi Y., Uryu M.: The structure and mechanical properties of sheets prepared from bacterial cellulose. Journal of Material Science, **24**, 3141–3145 (1989).
[67] Okiyama A., Motoki M., Yamanka S.: Bacterial cellulose IV. Application to processed foods. Food Hydrocolloids, **6**, 503–511 (1993).
[68] Shibazaki H., Kuga S., Fumihiko O., Usuda M.: Bacterial cellulose as separation medium. Journal of Applied Polymer Science, **50**, 965–969 (1993).
[69] Yamanaka S., Watanabe K. Applications of bacterial cellulose. in 'Cellulosic Polymers' (ed.: Gilbert R.) Hanser Publishers Inc., Cincinnati, **93** (1994).
[70] Geyer U., Heinze T., Stei A., Klenn D., Marsch S., Schumann D., Schmauder H.: Formation, derivatization and applications of bacterial cellulose. International Journal of Biological Macromolecule, **16**, 343–347 (1994).
[71] Nakagaito A. N., Iwamoto S., Yano H.: Bacterial cellulose: the ultimate nano-scalar cellulose morphology for the production of high-strength composites. Applied Physics A: Materials Science and Processing, **80**, 93–97 (2005).
[72] Ke T., Sun X.: Effect of moisture content and heat treatment on the physical properties of starch and poly (lactic acid) blends. Journal of Applied Polymer Science, **81**, 3069–3082 (2001).
[73] Park J. W., Im S. S., Kim S. H., Kim Y. H.: Biodegradable polymer blends of poly (L-lactic acid) and gelatinized starch. Polymer Engineering and Science, **40**, 2539–2550 (2000).
[74] Dufresne A.: Comparing the mechanical properties of high performances polymer nanocomposites from biological sources. Journal of Nanoscience and Nanotechnology, **6**, 322–330 (2006).
[75] Ke T., Sun S. X., Seib P.: Blending of poly (lactic acid) and starches containing varying amylose content. Journal of Applied Polymer Science, **89**, 3639–3646 (2003).
[76] Angles M. N., Dufresne A.: Plasticized starch/tunicin whiskers nanocomposites. 1. Structural analysis. Macromolecules, **33**, 8344–8353 (2000).
[77] Angle's M. N., Dufresne A.: Plasticized starch/tunicin whiskers nanocomposite materials. 2: Mechanical behavior. Macromolecules, **34**, 2921–2931 (2001).
[78] Dubief D., Samain E., Dufresne A.: Polysaccharide microcrystals reinforced amorphous poly (3-hydroxyoctanoate) nanocomposite materials. Macromolecules, **32**, 5765–5771 (1999).
[79] Herrick F. W., Casebier R. L., Hamilton J. K., Sandberg K. R.: Microfibrillated cellulose: Morphology and accessibility. Journal of Applied Polymer Science, **37**, 797–813 (1982).
[80] Wagberg L.: Wood material science. Finnish-swedish research programme, 2003–2007. Year Book 91–95 (2005).
[81] Nakagaito A. N., Yano H.: The effect of morphological changes from pulp fiber towards nano-scale fibrillated cellulose on the mechanical properties of high-strength plant fiber based composites. Applied Physics A-Materials Science and Processing, **78**, 547–552 (2004).
[82] Deitzel J. M., Kleinmeyer J. D., Hirvonen J. K., Beck Tan. N. C.: Controlled deposition of electrospun poly (ethylene oxide) fibers. Polymer, **42**, 8163–8170 (2001).
[83] Fong H., Reneker D. H.: Electrospinning and formation of nano-fibers. in 'Structure formation in polymeric fibers' (eds.: Salem D. R., Sussman M. V.) Hanser, Munich, 225–246 (2001).
[84] Fang X., Reneker D. H.: DNA fibers by electrospinning. Journal of Macromolecular Science, **36** 169–173 (1997).
[85] Taylor G. I.: Electrically driven jets. Proceedings of the Royal Society: Series A, **313**, 453–475 (1969).
[86] Larrondo L., St John Manley R.: Electrostatic fiber spinning from polymer melts I. and experimental observations on fiber formation and properties. Journal of Polymer Science, **19**, 909–920 (1981).
[87] Larrondo L., St John Manley R.: Electrostatic fiber spinning from polymer melts. II. Examination of the flow field in an electrically driven jet. Journal of Polymer Science, **19**, 921–932 (1981).
[88] Larrondo L., St John Manley R.: Electrostatic fiber spinning from polymer melts. III. Electrostatic deformation of a pendant drop of polymer melt. Journal of Polymer Science, **19**, 933–940 (1981).
[89] Liu H, Q., Hsieh Y-L.: Ultrafine fibrous cellulose membranes from electrospinning of cellulose acetate. Journal of Polymer Science: Part B, Polymer Physics, **40**, 2119–2129 (2002).
[90] Schroers M., Kokil A., Weder C.: Solid polymer electrolytes based on nanocomposites of ethylene oxide-epichlorohydrin copolymers and cellulose whiskers. Journal of Applied Polymer Science, **93**, 2883–2888 (2004).
[91] Oksman K., Mathew A. P., Bondeson D., Kvien I.: Manufacturing process of cellulose whiskers/polylactic acid nanocomposites. Composites Science and Technology, **66**, 2776–2784 (2006).
[92] Cranston E. D., Gray D. G.: Morphological and optical characterization of polyelectrolyte multilayers incorporating nanocrystalline cellulose. Biomacromolecules, **7**, 2522–2530 (2006).
[93] Albert S., Mittal G. S.: Comparative evaluation of edible coatings to reduce fat uptake in a deep-fried cereal product. Food Research International, **35**, 445–458 (2002).

[94] Ek R., Gustafsson C., Nutt A., Iversen T., Nyström C.: Cellulose powder from Cladophora sp. algae. Journal of Molecular Recognition, **11**, 263–265 (1998).

[95] Vilaseca F., Peijs T.: Cellulose-based nanocomposites. in '8th International Conference on Woodfiber-Plastic Composites (and Other Natural Fibers)' Madison, USA. 283–295 (2005).

[96] Gindl W., Keckes J.: All-cellulose nanocomposite. Polymer, **46**, 10221–10225 (2005).

[97] Petersson L., Oksman K.: Biopolymer based nanocomposites: Comparing layered silicates and microcrystalline cellulose as nanoreinforcement. Composites Science and Technology, **66**, 2187–2196 (2006).

[98] Decher G., Schlenoff J. B.: Multilayer thin films. Wiley, New York (2002).

[99] Park S. Y., Rubner M. F., Mayes A. M.: Free energy model for layer-by-layer processing of polyelectrolyte multilayer films. Langmuir, **18**, 9600–9609 (2002).

[100] Hiller J., Mendelsohn J. D., Rubner M. F.: Reversibly erasable nanoporous anti-reflection coatings from polyelectrolyte multilayers. Nature Materials, **1**, 59–67 (2002).

[101] Wang T., Rubner M. F., Cohen R. E.: Manipulating nanoparticle size within polyelectrolyte multilayers via electroless nickel deposition. Chemistry of Materials, **15**, 299–304 (2003).

[102] Michael C., Zhai L., Cohen R. E., Rubner M. F.: Controlled drug release from porous polyelectrolyte multilayers. Biomacromolecules, **7**, 357–364 (2006).

[103] Johal M. S., Casson J. L., Chiarelli P. A., Liu D-G., Shaw J. A., Robinson J. M. Wang H-L.: Polyelectrolyte trilayer combinations using spin-assembly and ionic self-assembly. Langmuir, **19**, 8876–8881 (2003).

[104] Kvien I., Tanem B. S., Oksman K.: Characterization of cellulose whiskers and their nanocomposites by atomic force and electron microscopy. Biomacromolecules, **6**, 3160–3165 (2005).

[105] Barnett K. G., Cosgrove T., Vincent B., Burgess A. N, Crowley T. L., King T., Turner J. D., Tadros T. F.: Neutron scattering, nuclear magnetic resonance, and photon correlation studies of polymers adsorbed at the solid-solution interface. Polymer, **22**, 283–285 (1981).

[106] Cosgrove T., Crowley T. L., Vincent B., Barnett K. G., Tadros T. F.: The configuration of adsorbed polymers at the solid-solution interface. Faraday Symposium Chemical Society, **16**, 101–108 (1981).

[107] Matsumura H., Sugiyama J., Glasser W. G.: Cellulosic nanocomposites. I. Thermally deformable cellulose hexanoates from heterogeneous reaction. Journal of Applied Polymer Science, **78**, 2242–2253 (2000).

[108] Ramos L. A., Ciacco G. T., Assaf J. M., El Seoud A. O., Frollini E.: Studies on dissolution and acetylation of microcrystalline, sisal, and cotton linter celluloses in dmac/licl solvent system. in 'Fourth International Symposium on Natural Polymers and Composites – ISNaPOL, 2002' Sao Pedro, Spain, 42–50 (2002).

[109] Dammstrom S., Salmen L., Gatenholm P.: The effect of moisture on the dynamical mechanical properties of bacterial cellulose/glucuronoxylan nanocomposites. Polymer, **46**, 10364–10371 (2005).

[110] Hull D., Clyne T. W.: An introduction to composite materials. Cambridge University Press, Cambridge (1996).

[111] Nishino T., Matsuda I., Hirao K.: All-cellulose composite. Macromolecules, **37**, 7683–7687 (2004).

[112] Brewer R. J., Bogan R. T.:Cellulose esters, organic . in 'Encyclopedia of Polymer Science and Engineering' (eds.: Mark H. F., Bikales N. M., Overberger C. G., Menges G., Kroschwitz J. I.) Wiley, New York 158–181 (1985).

[113] Serad G. A., Just E. K., Majewicz T. G.: Cellulose esters, fibers. in 'Encyclopedia of polymer science and engineering' (eds.: Kroschwitz J. I., Klingsberg A., Muldoon J., Salvatore A.) Wiley: New York, 200–226 (1985).

[114] Park H-M., Mohanty A., Drzal T. L., Ellen L., Mielewski F., Misra M.: Effect of sequential mixing and compounding conditions on cellulose acetate/layered silicate nanocomposites. Journal of Polymers and the Environment, **14**, 27–35 (2006).

[115] Park H. M., Liang X., Mohanty A. K., Misra M., Drzal L. T.: Effect of compatibilizer on nanostructure of the biodegradable cellulose acetate/organoclay nanocomposites. Macromolecules, **37**, 9076–9082 (2004).

[116] Park H., Mohanty A. K., Misra M., Drzal L. T.: Injection molded 'green' nanocomposite materials from renewable resources. Proceedings of the American Society for Composites 2003, 359–370 (2003).

[117] Park H., Mohanty A. K., Misra M., Drzal L. T.: Sequential mixing methods of environmentally benign nanocomposites from cellulose acetate/plasticizer/organoclay system. ANTEC conference proceedings, **3**, 2922–2926 (2004).

[118] Misra M., Park H., Mohanty A. K., Drzal L. T.: Sustainable nanocomposite materials from cellulosic plastics. Nanotech 2004, **3**, 316–319 (2004).

[119] Choi S., Cho M. S., Lee Y. Nam J. D., Lee J. H., Lee D. H.: Biodegradable cellulose based nanocomposites. in 'Transactions, 7th World Biomaterials Congress, Sydney, Australia' 1297–1301 (2004).

[120] Cho M. S., Choi S. H., Nam J. D., Lee Y.: Preparation and mechanical properties of nanocomposite of cellulose diacetate/montmorillonite. Polymer Korea, **28**, 551–555 (2004).

[121] Wibowo A. C., Misra M., Park H-M., Drzal L. T., Schalek R., Mohanty A. K.: Biodegradable nanocomposites from cellulose acetate: mechanical, morphological, and thermal properties. Composites: Part A, Applied Science and Manufacturing. **37**, 1428–1433 (2006).

[122] Yoshioka M., Takabe K., Sugiyama J., Nishio Y.: Newly developed nanocomposites from cellulose acetate/layered silicate/poly (ε-caprolactone): synthesis and morphological characterization. Journal of Wood Science, **52**, 121–127 (2006).

[123] Cai T., Hu Z., Marquez M.: Synthesis and self-assembly of nearly monodisperse nanoparticles of a naturally occurring polymer. Langmuir, **20**, 7355–7359 (2004).

[124] Zimmermann T., Pohler E., Schwaller P.: Mechanical and morphological properties of cellulose fibril reinforced nanocomposites. Advanced Engineering Materials, **7**, 1156–1161 (2005).

[125] Borges J. P., Godinho M. H, Martins A. F., Stamatialis D. F., de Pinho M. N., Belgacem M. N.: Tensile properties of cellulose fiber reinforced hydroxypropylcellulose films. Polymer Composites, **25**, 102–110 (2004).

[126] Choi Y., Simonsen. J.: Cellulose nanocrystal-filled carboxymethyl cellulose nanocomposites. Journal of Nanoscience and Nanotechnology, **6**, 633–639 (2006).

[127] Choi S. H., Cho M. S., Kim D., Kim J-H., Lee D. H., Shim S. J., Nam J-D., Lee Y.: Nanocomposite of ethyl cellulose using environment-friendly plasticizer. Polymer Korea, **29**, 399–402 (2005).

[128] Dong R., Zhang L., Zhang Z., Xia X.: Structure and properties of regenerated cellulose/tourmaline nanocrystal composite films. Journal of Polymer Science: Part B: Polymer Physics, **42**, 367–373 (2004).

[129] Suber L., Foglia S., Ingo G. M., Boukos N.: Synthesis and structural and morphological characterization of iron oxide-ion-exchange resin and cellulose nanocomposites. Applied Organometallic Chemistry, **15**, 414–420 (2001).

[130] Lu S., Forcada J.: Preparation and characterization of magnetic polymeric composite particles by miniemulsion polymerization. Journal of Polymer Science, Part A: Polymer Chemistry, **44**, 4187–4203 (2006).

[131] Park H-M., Li X., Jin C-Z., Park C-Y., Cho W-J., Ha C-S.: Preparation and properties of biodegradable thermoplastic starch/clay hybrids. Macromolecular Materials and Engineering, **287**, 553–558 (2002).

[132] Park H-M., Lee W-K., Park C-Y., Cho W-J., Ha C-S.: Environmentally friendly polymer hybrids: part I. Mechanical, thermal, and barrier properties of thermoplastic starch/clay nanocomposites. Journal of Mateialr Science, **38**, 909–915 (2003).

[133] Wilhelm H-M., Sierakowski M-R., Souza G. P., Wypych F.: Starch films reinforced with mineral clay. Carbohydrate Polymers, **52**, 101–110 (2003).

[134] Fischer H. R., Fischer S.: Biodegradable thermoplastic material. United States Patent 6811599 (2004).

[135] Fischer H.: Polymer nanocomposites: from fundamental research to specific applications. Materials Science and Engineering, **23**, 763–772 (2003).

[136] De Carvalho A. J. F., Curvelo A. A. S., Agnelli J. A. M. Coimbra M. A.: A first insight on composites of thermoplastic starch and kaolin. Carbohydrate Polymers, **45**, 189–194 (2001).

[137] Chen B., Evans J. R. G.: Thermoplastic starch-clay nanocomposites and their characteristics. Carbohydrate Polymers, **61**, 455–463 (2005).

[138] McGlashan S. A., Halley P. J.: Preparation and characterisation of biodegradable starch-based nanocomposite materials. Polymer International, **52**, 1767–1673 (2003).

[139] Kalambur S. B., Rizvi S. S. H.: Starch-based nanocomposites by reactive extrusion processing. Polymer International, **53**, 1413–1416 (2004).

[140] Pandey J. K., Raghunatha R. K., Pratheep K. A., Singh R. P.: An overview on the degradability of polymer nanocomposites. Polymer Degradation and Stability, **88**, 234–250 (2005).

[141] Wang H., Sun X., Seib P.: Strengthening blends of poly (lactic acid) and starch with methylenediphenyl diisocyanate. Journal of Applied Polymer Science, **82**, 1761–1767 (2001).

[142] Wang H., Sun X., Seib P.: Mechanical properties of poly (lactic acid) and wheat starch blends with methylenediphenyl diisocyanate. Journal of Applied Polymer Science, **84**, 1257–1262 (2002).

[143] Wang H, Sun X, Seib P.: Effect of starch moisture on properties of wheat starch/poly (lactic acid) blend containing methylenediphenyl diisocyanate. Journal of Polymer Environment, **10**, 133–138 (2002).

[144] Zhang J-F., Sun X.: Mechanical and thermal properties of poly (lactic acid)/starch blends with dioctyl maleate. Journal of Applied Polymer Science, **94**, 1697–1704 (2004).

[145] Ke T., Sun X. S.: Starch poly (lactic acid), and poly (vinyl alcohol) blends. Journal of Polymers and the Environment, **11**, 7–14 (2003).

[146] Shogren R. L., Doane W. M., Garlotta D., Lawton J. W., Willett J. L.: Biodegradation of starch/polylactic acid/poly(hydroxyester-ether) composite bars in soil. Polymer Degradation and Stability, **79**, 405–411 (2003).

[147] Croce F., Appetecchi G. B., Persi L., Scrosati B.: Nanocomposite polymer electrolytes for lithium batteries. Nature, **394**, 456–458 (1998).

[148] Bruce P. G.: Solid state electrochemistry. Cambridge University Press, Cambridge **116** (1995).

[149] Jain H., Thomas J. O., Whittingham M. S.: Solid electrolytes: Advances in science and technology. MRS Bulletin, **25**, 11 (2000).

[150] Azizi Samir M. A. S., Chazeau L., Alloin F., Cavaillé J-Y., Dufresne A., Sanchez J-Y., Wieczorek W., Plocharski J., Ciosek M.: POE-based nanocomposite polymer electrolytes reinforced with cellulose whiskers. Electrochimica Acta, **50**, 3897–3903 (2005).

[151] Azizi Samir M. A. S., Alloin F., Wladimir G., Sanchez J-Y., Dufresne A.: Nanocomposite polymer electrolytes based on poly (oxyethylene) and cellulose nanocrystals. Journal of Physical Chemistry: Part B, **108**, 10845–10852 (2004).

[152] Azizi Samir M. A. S., Alloin F., Sanchez J. Y., Dufresne A.: Cellulose nanocrystals reinforced poly (oxyethylene). Polymer, **45**, 4149–4157 (2004).

[153] Azizi Samir M. A. S., Montero M. A., Alloin F., Sanchez J-Y., Dufresne A.: Plasticized nanocomposite polymer electrolytes based on poly (oxyethylene) and cellulose whiskers. Electrochimica Acta, **49**, 4667–4677 (2004).

[154] Azizi Samir M. A. S., Alloin F., Sanchez J. Y., Dufresne A.: Cross-linked Nanocomposite polymer electrolytes reinforced with cellulose whiskers. Macromolecules, **37**, 4839–4844 (2004).

[155] Azizi Samir M. A. S., Alloin F., Sanchez J-Y.: Nanocomposite polymer electrolytes based on poly (oxyethylene) and cellulose whiskers. Cienciae e Tecnologia, **15**, 109–113 (2005).

[156] Azizi Samir M. A. S., Alloin F., Dufresne A.: High performance nanocomposite polymer electrolytes. Composite Interfaces, **13**, 545–559 (2006).

[157] Millon L. E., Wan W. K.: The polyvinyl alcohol-bacterial cellulose system as a new nanocomposite for biomedical applications. Journal of Biomedical Materials Research: Part B, Applied Biomaterials, **79**, 245–253 (2006).

[158] Noishiki Y., Nishiyama Y., Wada M., Kuga S., Magoshi J.: Mechanical properties of silk fibroin-microcrystalline cellulose composite films. Journal of Applied Polymer Science, **86**, 3425–3429 (2002).

[159] Wan Y. Z., Hong L., Jia S. R., Huang Y., Zhu Y., Wang Y. L., Jiang H. J.: Synthesis and characterization of hydroxyapatite-bacterial cellulose nanocomposites. Composites Science and Technology, **66**, 1825–1832 (2006).

[160] Wan Y. Z., Huang Y., Yuan C. D., Raman S., Zhu Y., Jiang H. J, He F., Gao C.: Biomimetic synthesis of hydroxyapatite/bacterial cellulose nanocomposites for biomedical applications. Materials Science and Engineering, **27**, 855–864 (2006).

[161] Zakharov N. A., Ezhova Z. A., Koval E. M., Kalinnikov V. T., Chalykh A. E.: Hydroxyapatite-carboxymethyl cellulose nanocomposite biomaterial. Inorganic Materials, **41**, 509–515 (2005).

[162] Marques P. A. A. P., Trindade T., Neto C. P.: Titanium dioxide/cellulose nanocomposites prepared by a controlled hydrolysis method. Composites Science and Technology, **66**, 1038–1044 (2006).

[163] Allan G. G., Ko Y. C.: The microporosity of pulp. The forces influencing the intra- and interfiber pore structure and pore size distribution in pulp and paper. cellulose. Chemical Technology, **29**, 479–485 (1995).

[164] Allan G. G., Balaban C., Bellefeuille-Williams C. I., Carroll J. P., Dutkiewicz J., Garner B. A., Ko Y. Lee A. W. W., McConnell W. J., Miller J. M., Negri J. M., Tantikulananta J., Raghuraman M., Ritzenthaler P., Sahafi L., Struszczyck H., Yahiaoui A.: The microporosity of pulp. A key to new markets. Tappi Journal, **74**, 83–84 (1991).

[165] Fahmy Y., Mobarak F.: On fine structure of cellulose fibers. Svensk Papperstidn, **74**, 2–9 (1971).

[166] Allan G. G., Carroll J. P., Negri A. R., Raghuraman M.: The microporosity of pulp. the precipitation of inorganic fillers within the micropores of the cell wall. Tappi Journal, **75**, 175–178 (1992).

[167] Tirrell D. A., Donaruma L. G., Turek A. B.: Macromolecules as drugs and as carriers for biologically active materials. The New York Academy of Sciences, New York (1985).

[168] Fahmy T. Y. A., Mobarak F., Fahmy Y., Fadl M. H., El-Sakhawy M.: Nanocomposites from natural cellulose fibers incorporated with sucrose. Wood Science and Technology, **40**, 77–86 (2006).

[169] Laufenberg T. L.: Packaging and lightweight structural composites. in 'Paper and Composites from Agro-Based Resources' (eds.: Rowell R. M., Young R. A., Rowell J.) CRC Press, Boca Raton, 338–349 (1996).

[170] Arvanitoyannis I., Biliaderis C. G., Ogawa H., Kawasaki N.: Biodegradable films made from low-density polyethylene (LDPE), rice starch and potato starch for food packaging applications: Part 1. Carbohydrate Polymers, **36**, 89–104 (1998).

[171] Arvanitoyannis I., Kolokuris I., Nakayama A., Aiba S. I.: Preparation and study of novel biodegradable blends based on gelatinised starch and 1,4-trans-polyisoprene (gutta percha) for food packaging or biomedical applications. Carbohydrate Polymers, **34**, 291–302 (1997).

[172] Ray S. S., Yamada K., Okamoto M., Ueda K.: Polylactide/layered silicate nanocomposite. A novel biodegradable material. Nano Letters, **2**, 1093–1096 (2002).

[173] Ray S. S., Yamada K., Okamoto M., Fujimoto Y., Ogami A., Ueda K.: New polylactide/layered silicate nanocomposites. 3. highperformance biodegradable materials. Chemistry of Materials, **15**, 1456–1465 (2003).

[174] Gaudel-Siri A., Brocorens P., Siri D., Gardebien F., Brédas J-L., Lazzaroni R.: Molecular dynamics study of e-caprolactone intercalated in Wyoming sodium montmorillonite. Langmuir, **19**, 8287–8291 (2003).

[175] Jimenez G., Ogata N., Kawai H., Ogihara T.: Structure and thermal/mechanical properties of poly (ε-caprolactone)-clay blend. Journal of Applied Polymer Science, **35**, 2211–2220 (1997).

[176] Kubies D., Pantoustier N., Dubois P., Rulmont A., Jerome R.: Controlled ring-opening polymerization of e-caprolactone in the presence of layered silicates and formation of nanocomposites. Macromolecules, **35**, 3318–3320 (2002).

[177] Lunt J.: Large-scale production, properties and commercial applications of poly lactic acid polymers. Polymer Degradation and Stability, **59**, 145–151 (1998).

[178] Auras R., Harte B., Selke S.: An overview of polylactides as packaging materials. Macromolecular Bioscience, **4**, 835–864 (2004).

[179] Matos G., Wagner L.: Consumption of materials in the united states 1900–1995. Annual Review of Energy and the Environment, **23**, 107–122 (1998)

eXPRESS Polymer Letters Vol.1, No.9 (2007) 576–584
Available online at www.expresspolymlett.com
DOI: 10.3144/expresspolymlett.2007.79

Elasticity of rubber-like materials measured by AFM nanoindentation

D. C. Lin[1*], *E. K. Dimitriadis*[2], *F. Horkay*[3*]

[1]Laboratory of Integrative and Medical Biophysics, National Institutes of Health, 9 Memorial Drive, Bldg. 9 Rm. 1E118, Bethesda, MD 20892, USA
[2]National Institute of Biomedical Imaging and Bioengineering, National Institutes of Health, 13 South Drive, Bldg. 13 Rm. 3N17, Bethesda, MD 20892, USA
[3]Laboratory of Integrative and Medical Biophysics, National Institutes of Health, 13 South Drive, Bldg. 13 Rm. 3W16, Bethesda, MD 20892, USA

Received 25 May 2007; accepted in revised form 5 July 2007

Abstract. We exploit the force spectroscopy capabilities of the atomic force microscope in characterizing the local elasticity of rubber-like materials. Extraction of elastic properties from force curves usually relies on the linear theory pioneered by Hertz. While the Hertzian force-indentation relationships have been shown to be accurate in modeling the contact mechanics at sufficiently shallow indentation depths, the linear deformation regime of the probed material is exceeded in many practical applications of nanoindentation. In this article, a simple, nonlinear force-indentation equation based on the Mooney-Rivlin model is derived and used to fit data from the indentation of lightly crosslinked poly(vinyl alcohol) gels in equilibrium with water. The extracted values of Young's modulus show good agreement with those obtained by both macroscopic compression testing and by fitting truncated portions of the force curves with the Hertz equation.

Keywords: *mechanical properties, atomic force microscopy, polymer gels, indentation*

1. Introduction

Despite its prevalence in various fields as a technique for measuring the local mechanical properties of elastic materials, the accuracy of indentation testing utilizing the atomic force microscope (AFM: see Figure 1) remains equivocal. Aside from artifacts arising from factors that can affect instrument performance (e.g., drift due to temperature variations), the causes of the ambiguity can be methodological (e.g., uncertainties in determining cantilever bending stiffness and tip dimensions) or analytical (e.g., uncertainties in robustness and accuracy of the data processing method) in nature. With care and the employment of existing technologies, environmental and methodological effects can be minimized. However, the latter cate-

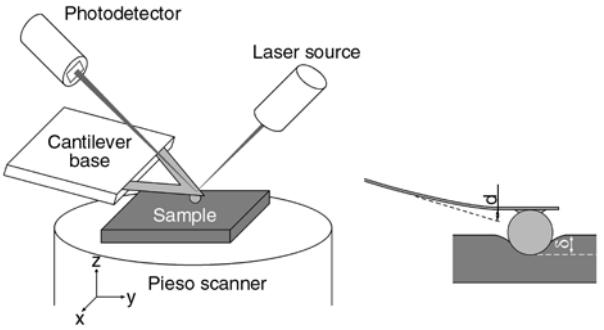

Figure 1. Schematics of the atomic force microscope (left) and indentation of the sample by the tip (right). Displacement control is achieved by moving the sample (as shown) or the cantilever base, usually with piezo tube actuators. Force is inferred from laser-based measurements of cantilever deflection *d*. The indentation depth δ is dependent on both *d* and the vertical displacement of the scanner (or the cantilever base) *z*.

*Corresponding authors, e-mail: lindavid@mail.nih.gov, horkay@helix.nih.gov
© BME-PT and GTE

gory of sources is not as easily addressed because data processing methods are model dependent and no clear performance benchmark exists. Furthermore, indentation at all length scales can deviate significantly from ideal behavior due to tip-sample interactions (e.g., adhesion) and material nonuniformities. This is especially true of gels and other rubber-like materials.

Recently, we developed and validated a robust and comprehensive scheme for extracting Young's moduli from the indentation of soft materials based on linear elastic contact mechanics theory [1, 2]. For a set of poly(vinyl alcohol) – henceforth abbreviated to PVA – gels at different polymer concentrations, Young's moduli agreed well with macroscopic compression tests when indentation strains did not exceed the linear elastic limit. These results are consistent with the generally accepted view that small-strain deformation of many rubber-like materials is virtually a linear elastic process and can be modeled accordingly. Depending on the magnitude of tip-sample interactions, however, it is oftentimes difficult to control the indentation depth of each stroke of the AFM probe. Furthermore, tip-sample interactions often result in decreased signal-to-noise ratios. The effect is usually most pronounced in the vicinity of the tip-sample contact point; under such circumstances, accuracy is adversely affected by limiting the analysis to data points that do not exceed a strain threshold. For materials that exhibit rubber elastic behavior, derivation of a single contact mechanics equation relating force and indentation depth is therefore necessary. Such a model would also be applicable in estimating the large-strain mechanical response of soft biological materials such as cells and tissues, where the use of linear elasticity theory generally leads to significant errors in Young's modulus [3]. In this work, we propose an approximate relationship suitable for the indentation of Mooney-Rivlin materials with spherical probes and test it by fitting to data obtained from the AFM indentation of highly swollen PVA gels. Accuracy of this model is assessed by comparison with results from macroscopic compression tests and from fitting initial, small-strain portions of each dataset with the classical Hertz equation.

2. Theory

The indentation problem is based on the Hertz theory of contact between two elastic spheres in the absence of adhesion [4]. Johnson *et al.* [5] pioneered the theory of adhesive contact, citing evidence of deviation from Hertzian behavior in numerous experiments as the motivation for developing the now well-known Johnson-Kendall-Roberts (JKR) theory. Other contributors to the field include Derjaguin *et al.* [6], Tabor [7], and Maugis [8]. For the purposes of this work, only the Derjaguin-Muller-Toporov (DMT) theory is considered. The JKR and DMT theories were found by Tabor to apply to opposite extremes of the relationship between surface force and sample compliance, with the DMT theory pertaining to relatively stiff samples and weak adhesive forces [7].

The Hertz and DMT equations ((1) and (2)) for the indentation of a linear elastic, infinite half-space with a rigid sphere are [4, 6]:

$$F = F_n + F_{ad} = \frac{4ER^{1/2}\delta^{3/2}}{3(1-\nu^2)} \tag{1}$$

$$a = \sqrt{R\delta} \tag{2}$$

where F is the net indentation force, F_n is the applied normal force, F_{ad} is the tip-sample adhesive force (= 0 in the Hertz theory), δ is the indentation depth, a is the contact radius, R is the radius of the sphere, and E and ν are Young's modulus and Poisson's ratio of the indented sample, respectively. In the DMT theory, the constant adhesive force is related to the interfacial energy (γ) by Equation (3):

$$F_{ad} = 2\pi\gamma R \tag{3}$$

According to Yoffe [9], Hertz stated explicitly that Equation (2) applies only to cases in which the contact radius is small relative to the radius of the indenter (i. e., $a/R < 0.1$). In practice, however, contact radii frequently exceed the imposed limit. Experimental and analytical support for applying the equation at large relative contact radii can be found in tests performed by Kumar and Narasimhan [10] and the theoretical studies of Yoffe [9]. In the macroscopic indentation of polymethyl methacrylate samples using stainless steel balls, Kumar and Narasimhan found excellent agreement between measured values of the contact radius and those predicted by Equation (2) for a/R

approaching 0.14. Yoffe developed a first-order correction to the Hertzian contact radius at large indentation depths and demonstrated that the deviation from the Hertz theory as the contact area widened was dependent on ν. As ν approached the incompressibility limit of 0.5, it was found that Equation (2) began to over predict the magnitude of the contact radius. For example, when ν = 0.4, the error in *a* predicted by Equation (2) increased from 1% at $a/R \sim 0.28$ to 6% at $a/R \sim 0.53$. These errors can be considered acceptably small, even at the large strains that are frequently applied in the indentation of polymer gels.

3. Materials and methods

3.1. Sample preparation and testing

PVA solutions were prepared by dissolving PVA (molecular weight 70 000–100 000; Sigma) in deionized water at 99°C to make a stock solution with a concentration of 14% (w/w). Gels were made by crosslinking the PVA solution with glutaraldehyde at pH ~1.5 (adjusted by addition of HCl). To prepare gel samples at two different levels of compliance, the PVA concentration was changed while maintaining a constant crosslink density (one unit of GDA per 100 units of vinyl alcohol). The elastic moduli of these gels differed by roughly an order of magnitude corresponding to the typical range of biological soft tissues such as cartilage. Gel cylinders and thick layers (2 mm to >1 cm) with final PVA concentrations of 6% and 12% (w/w) were cast in molds (1 cm in diameter and 1 cm in height) and 35 mm Petri dishes, respectively. All samples were stored in deionized water until testing.

A bench top materials testing system (Stable Micro Systems, UK) was used to perform displacement-controlled compression of the gel cylinders at a ramp speed of 1 mm/s. The undeformed dimensions of each cylinder were measured prior to compression with a micrometer. The Young's moduli of the PVA gels were calculated from the neo-Hookean equation (4):

$$\sigma = G(\lambda - \lambda^{-2}) \tag{4}$$

where σ is the engineering stress, λ is the compression ratio, and *G* is the shear modulus. In the experiment, λ was varied in the range $0.6 < \lambda < 1$. The absence of volume change and barreling during the compression measurements was checked [1].

Nanoindentation of gels was performed using a commercial AFM (Bioscope I with a Nanoscope IIIA controller, Veeco Instruments, Santa Barbara, CA) seated atop an inverted optical microscope. General-purpose silicon nitride tips were used (model DNP, Veeco). The cantilevers were modified by gluing either a 9.6 μm diameter polystyrene bead or a 5.5 μm diameter glass bead near the tip. The spring constant of each cantilever was determined using the thermal tune method [11]. Multiple force curves for each PVA film were collected using the 'force-volume' mode of the AFM. In this automated raster scanning method, the user defines the size of the square region to be scanned, the resolution, and the relative trigger threshold (i. e., the maximum cantilever deflection). Because the gels were assumed to be relatively homogeneous, the resolution was set to the lowest limit of 16 × 16 indentations covering a 20 μm × 20 μm region. Relative trigger thresholds were set to either 100 or 50 nm.

3.2. Processing of AFM indentation data

An algorithm that we developed previously [1, 2] was used as the basis for automated processing of indentation data. Briefly, the contact point dependent method requires the identification of multiple reference points, shown in Figure 2 for both adhesive and non-adhesive analysis. These points are used to transform the typical raw values of cantilever deflection (*d*) and base displacement (*z*) to applied force and indentation, respectively. The conversions are given by Equations (5), (6) and (7):

$$F_n = k_c(d - d_0); \text{ negligible adhesion} \tag{5}$$

$$F_n = k_c(d - d_1); \text{ significant adhesion} \tag{6}$$

$$\begin{aligned}\delta &= (z - z_0) - (d - d_0) \\ &= (z - d) - (z_0 - d_0) = w - w_0\end{aligned} \tag{7}$$

where k_c is the spring constant of the cantilever, (z_0, d_0) are the coordinates of the contact point, and (z_1, d_1) are the coordinates of the point of zero applied force (see Figure 2). The transformed variable $w = z - d$ is introduced for simplification. The adhesive force is then related to the reference points by Equation (8):

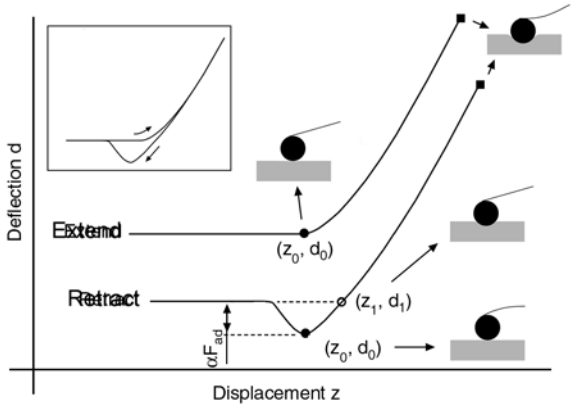

Figure 2. A typical set of deflection-displacement curves in extension and retraction with negligible adhesive interactions in extension and significant adhesion upon retraction. The two curves are offset from each other for clarity; they are plotted without offset in the inset. In extension, only the contact point (z_0, d_0) is required to transform the data to force *vs*. indentation. In retraction, two reference points are needed – the contact point and the point of zero applied force (z_1, d_1). The schematics show the bending of the cantilever at the reference points and at the point of maximum indentation.

$$F_{ad} = k_c(d_1 - d_0) \tag{8}$$

Substitution of Equations (5) through (8) into Equation (1) recasts the force-indentation relation into a form appropriate for fitting the raw data and extracting the values of E.

4. Results and discussion

In this section, we first develop a nonlinear contact mechanics model that describes the force-indentation relationship for rubber-like materials. The derivation is based on the concepts discussed in the theoretical section and on the Mooney-Rivlin formalism. A comparison is then made between the predictions of this model and the experimental data obtained for the PVA hydrogels.

4.1. Formulation of a nonlinear contact mechanics model

The Hertz and DMT equations are based on the theory of linear elasticity and therefore subject to its inherent limitations, including the requirement of geometric (i. e., stress-strain) linearity. As previously mentioned, it may not always be feasible to limit indentation depths to the linear regime. In the realm of rubber elasticity, many phenomenological theories have been developed. One of the simplest and perhaps most well-known of the stress-strain relations derived from these theories is the Mooney-Rivlin equation (9) [12]:

$$\sigma = 2C_1(\lambda - \lambda^{-2}) + 2C_2(\lambda - \lambda^{-3}) \tag{9}$$

where σ is the stress, λ is the extension ratio, and C_1 and C_2 are constants. We wish to use Equation (9) as the basis of a force-indentation relationship. To that end, we define the effective or average stress and strain due to indentation. The indentation stress, σ^*, can be set equal to the mean contact pressure (force over the contact area), given by Equation (10):

$$\sigma^* = \frac{F}{\pi a^2} \tag{10}$$

The indentation strain, ε^*, is defined by Equation (11) [13]:

$$\varepsilon^* = \frac{a}{R} \tag{11}$$

For linear elastic (Hertzian) contact, it can be seen that σ^* and ε^* are linearly proportional, giving a Hookean equation (12) of the form:

$$\sigma^* = \zeta\varepsilon^*, \text{ with } \zeta = \frac{4E}{3\pi(1-\nu^2)} \tag{12}$$

In order to derive force-indentation relations for materials obeying the constitutive Equation (9), disparities in sign conventions for stress and strain between Equations (9) and (12) must first be resolved. In Equation (9), standard engineering convention applies, with stresses and strains positive in tension. This implies that $\lambda > 1$ in tension and $\lambda < 1$ in compression. Because indentation is viewed as a compressive process, the sign convention for σ^* and ε^* are opposite from the standard convention. Replacing σ with $-\sigma^*$ and λ with $(1 - \varepsilon^*)$ in Equation (9) yields Equation (13):

$$\frac{\sigma^*}{\varepsilon^*} = B_1\left(\frac{\varepsilon^{*3} - 3\varepsilon^{*2} + 3\varepsilon^*}{\varepsilon^{*3} - 2\varepsilon^{*2} + \varepsilon^*}\right) + B_2\left(\frac{\varepsilon^{*3} - 3\varepsilon^{*2} + 3\varepsilon^*}{-\varepsilon^{*4} + 3\varepsilon^{*3} - 3\varepsilon^{*2} + \varepsilon^*}\right) \tag{13}$$

where the constants C_1 and C_2 no longer hold the same meaning and have been replaced with $B_1/2$ and $B_2/2$, respectively.

Substitution of Equations (10) and (11) into Equation (13) results in a relationship between indentation force and contact radius. To obtain a more practicable equation in terms of force and indentation, the relationship between contact radius and indentation is required. Assuming that the manner in which a varies with δ is independent of material linearity, we use Equation (2) as a first approximation. Algebraic manipulation yields Equation (14):

$$F = \pi R^{1/2} B_1 \left(\frac{\delta^{5/2} - 3R^{1/2}\delta^2 + 3R\delta^{3/2}}{\delta - 2R^{1/2}\delta^{1/2} + R} \right) + \pi R^{1/2} B_2 \left(\frac{R^{1/2}\delta^{5/2} - 3R\delta^2 + 3R^{3/2}\delta^{3/2}}{-\delta^{3/2} + 3R^{1/2}\delta - 3R\delta^{1/2} + R^{3/2}} \right) \quad (14)$$

where $F = F_{ad} + F_n$ when adhesive interactions are present. At infinitesimal strain or indentation depth, Equation (1) applies, and Equation (14) reduces to Equation (15):

$$B_1 + B_2 = \frac{4E_0}{9\pi(1-\nu^2)} \quad (15)$$

where E_0 is the initial Young's modulus and $\nu = 0.5$ for incompressible materials. Equations (14) and (15) comprise an approximate Mooney-Rivlin contact mechanics model that can be applied to the indentation of rubber-like materials; elastic properties of the samples are represented by the extracted Young's moduli. The model reduces to the neo-Hookean form when $B_2 = 0$.

Justification for the assumption that the contact radius is independent of material linearity can be found in the results of the finite element analyses performed by Mesarovic and Fleck [14] on the indentation behavior of elastic-plastic solids. Such materials undergo strain hardening in compression, as do Mooney-Rivlin solids. Under uniaxial tension, the Ramberg-Osgood hardening relationship employed in the finite element study has the form of Equation (16):

$$\frac{\varepsilon}{\varepsilon_0} = \frac{\sigma}{\sigma_0} + \left(\frac{\sigma}{\sigma_0} \right)^m \quad (16)$$

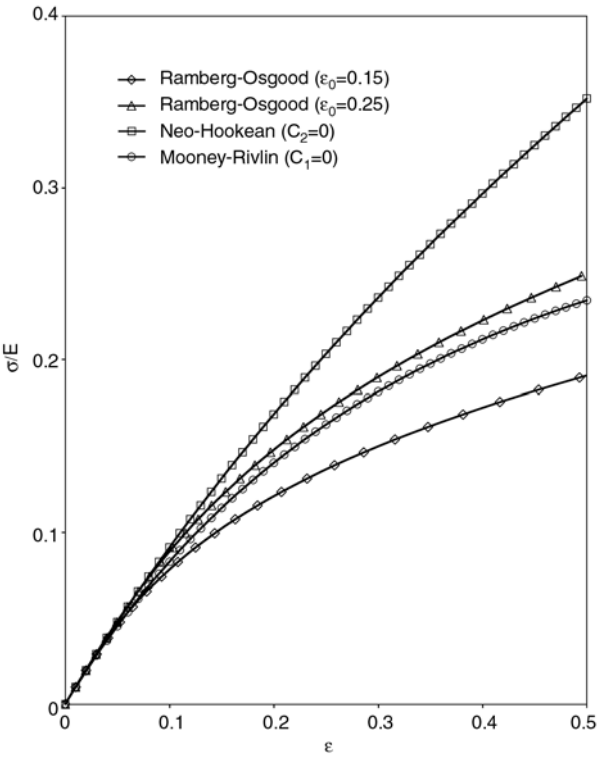

Figure 3. Comparison of the Ramberg-Osgood elastic-plastic hardening equation and the Mooney-Rivlin equation in tension. Normalized engineering stress-strain curves, where σ is stress, E is Young's modulus, and ε is strain, are shown for different cases of the two relationships. Following Mesarovic and Fleck, a hardening exponent of 3 is used in the Ramberg-Osgood equation [14]. Yield strains (ε_0) of 15% and 25% are shown. The two extreme cases of the Mooney-Rivlin equation, given by Equation (9), are plotted: $C_2 = 0$ (representative of a neo-Hookean solid) and $C_1 = 0$.

where ε_0 and σ_0 are the strain and stress at the yield point, respectively. The strain-hardening exponent m defines the deformation behavior, with $m = 1$ representing linear elastic response and $m \to \infty$ corresponding to elastic-ideally plastic response; an intermediate value of $m = 3$ was used by Mesarovic and Fleck in their study. The mathematical similarity between the Mooney-Rivlin and Ramberg-Osgood equations is demonstrated in Figure 3, where stress-strain curves are shown for a typical hardening material with linear Young's modulus of 100 kPa and a linear strain limit of approximately 15%. Mesarovic and Fleck found that the contact radius followed the form of Equation (2) beyond the yield point; with further indentation, contact radii predicted by Equation (2) became increasingly smaller than the actual values. This likely due to the

Table 1. Young's moduli of PVA gels from compression and AFM indentation (mean ± SD)

%	Macro. [kPa]	Small strain, linear elastic		Large strain, Mooney-Rivlin	
		Extend [kPa]	Retract [kPa]	Extend [kPa]	Retract [kPa]
6	21.51 ± 0.59	16.55 ± 2.74	19.39 ± 3.26	18.23 ± 2.38	19.51 ± 4.69
12	115.50 ± 1.86	113.66 ± 6.06	108.98 ± 9.17	115.82 ± 7.21	110.08 ± 13.17

permanent pile-up of material around the indenter, which is typically associated with the indentation of elastic-plastic materials such as metals [15, 16].

4.2. Comparison of the model with experimental results

Results of the macroscopic compression and AFM indentation tests are summarized in Table 1. There is generally good agreement between the macroscopic Young's moduli and values obtained from the small strain and large strain analyses of the AFM indentation data. Adhesion during indentation was evident only in the retraction strokes, prior to tip-sample separation. The small strain analysis was performed by truncating the datasets at an indentation strain of about 15% and applying Equation (1). The large strain analysis using Equation (14) was performed without data truncation.

In fitting the macroscopic compression data with Equation (9) over a large range of λ ($0.6 < \lambda < 1$), it was found that $C_2 \sim 0$ within the experimental error. This is consistent with the macroscopic, neo-Hookean behavior of PVA gels tested under similar conditions [17, 18] and of lightly crosslinked, highly swollen gels in general [12, 19]. Values of the Mooney-Rivlin fitting parameters B_1 and B_2 from fitting of the indentation data with Equation (14) are summarized in Table 2. At the microscopic length scale probed by the AFM, the large variability in B_2 may reflect inhomogeneities due

Table 2. Mooney-Rivlin fitting coefficients for large strain analysis (mean ± SD)

%	Extend		Retract	
	B_1 [kPa]	B_2 [kPa]	B_1 [kPa]	B_2 [kPa]
6	4.92 ± 0.97	–1.49 ± 0.55	8.08 ± 2.28	–4.09 ± 1.49
12	39.60 ± 4.46	–17.76 ± 3.15	43.48 ± 10.20	–21.50 ± 7.32

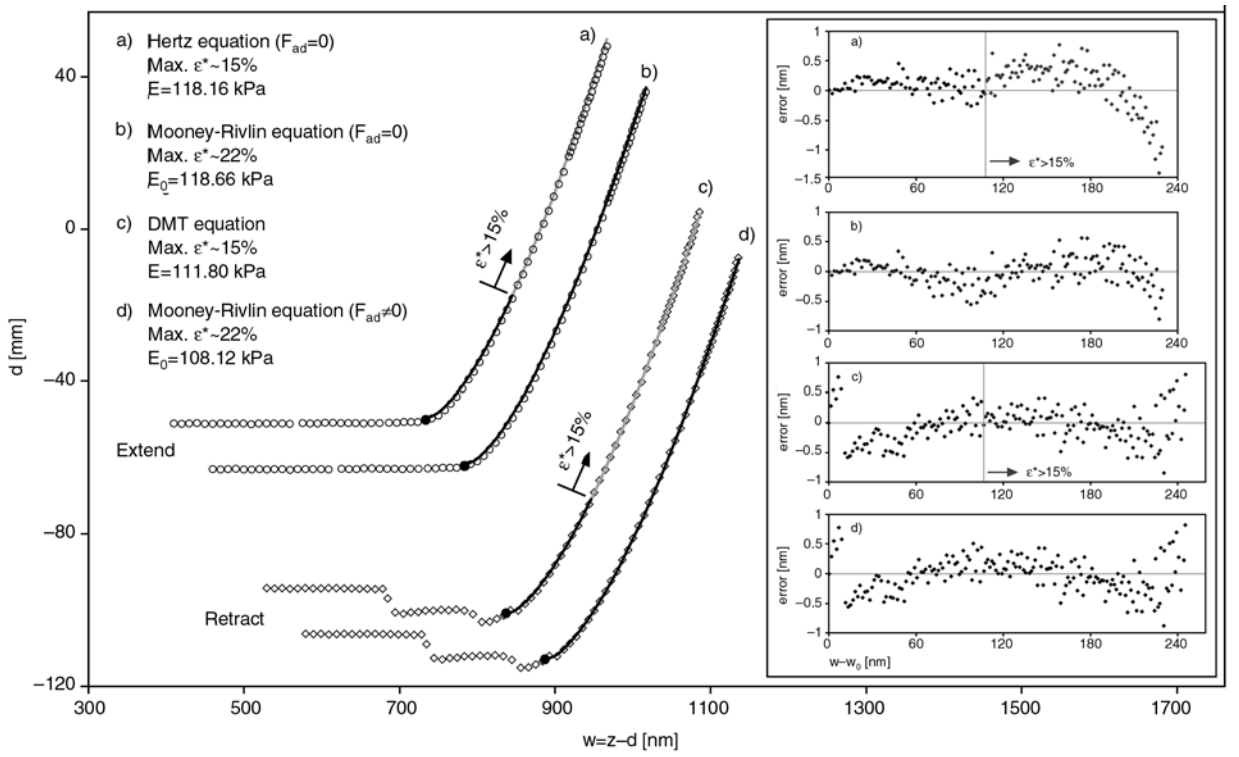

Figure 4. Sample dataset from the indentation of the 12% gel. *d* is the cantilever deflection and *z* is the base displacement. The extension and retraction curves (every fifth point is plotted) are offset from one another and each is shown with the small strain linear elastic fit and the large strain Mooney-Rivlin fit. The linear elastic fits have been extended beyond 15% strain for comparison (extended portions are shown in gray). Plots of the residual errors for each fit are displayed in the inset.

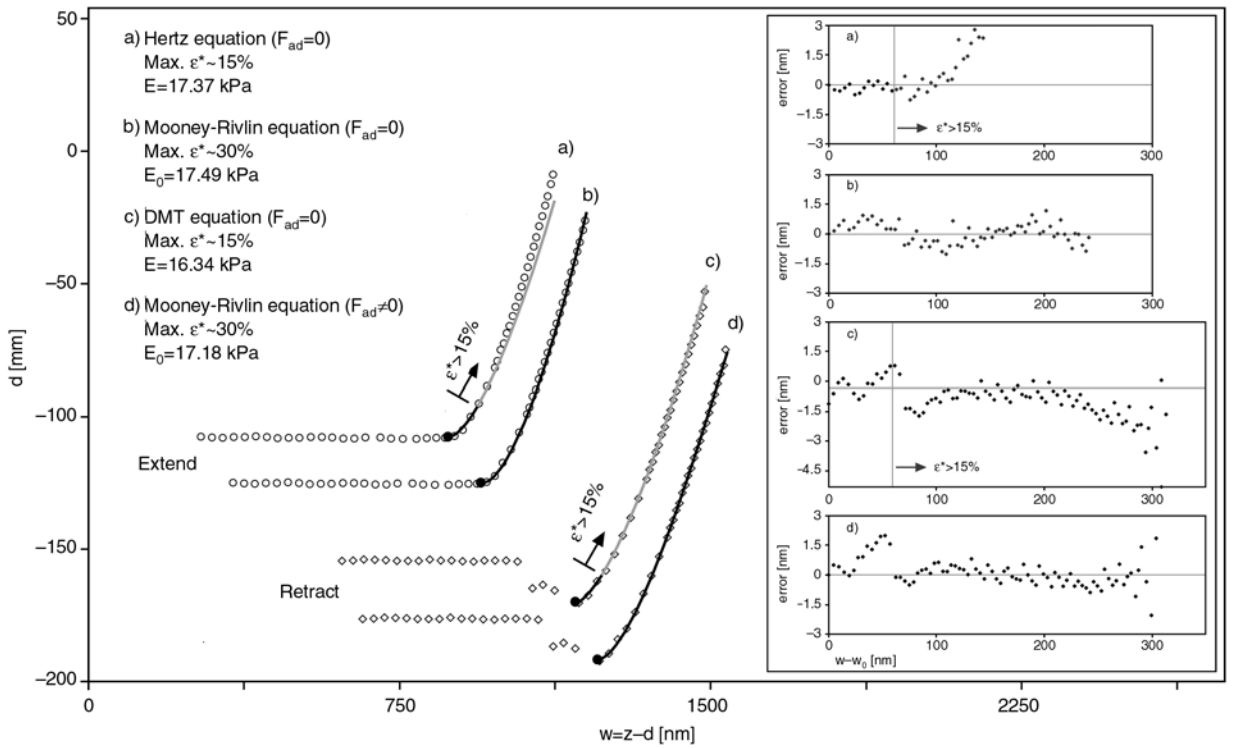

Figure 5. Sample dataset from the indentation of the 6% gel. *d* is the cantilever deflection and *z* is the base displacement. The extension and retraction curves (every fifth point is plotted) are offset from one another and each is shown with the small strain linear elastic fit and the large strain Mooney-Rivlin fit. The linear elastic fits have been extended beyond 15% strain for comparison (extended portions are shown in gray). Plots of the residual errors for each fit are displayed in the inset.

likely to local differences in polymer concentration. Equation (14) therefore allows us to detect these structural nonuniformities and quantifies the local deviation from neo-Hookean behavior. It should be mentioned that the Mooney-Rivlin formalism is not a constitutive material law since the values of the material constants may depend on the mode of deformation. Hence, extreme caution should be exercised when applying Equations (9) and (14).

Strains at maximum indentation depth were approximately 22% and 30% for the 12% and 6% gels, respectively. The 12% gel exhibited a linear regime that was significantly wider than that of the 6% gel, as illustrated by the examples in Figures 4 and 5. In fact, the residual errors shown in Figure 4 indicate that the 12% gel behaved linearly up to the maximum indentation depth. Strain hardening in the 6% gel is manifested in the poor fit of Equation (1) to the data beyond ~15% strain, as shown in Figure 5. Regardless of the degree of nonlinearity at maximum indentation depth, Equation (14) was found to be a good fit of both extension and retraction data. Compared to the small strain, linear analysis using Equation (1), the large strain analysis using Equation (14) yielded smaller differences between Young's moduli in extension and retraction. We attribute the improved agreement to the inclusion of more data points in the large strain analysis.

Synthetic gels prepared by the crosslinking of polymer chains in solution can be considered isotropic and homogeneous at macroscopic length scales. However, at the submicron level probed by the AFM, spatial variations in mechanical properties due to local concentration nonuniformities become detectable. In biological materials, such variations are much more pronounced, even over regions as small as a few tens of square nanometers. AFM nanoindentation has therefore become a powerful technique for generating elasticity maps of living cells [20–25] and the extracellular matrix [26–31]. To illustrate the differences between relatively homogeneous synthetic polymer gels and biological tissues, Young's modulus maps from 6% and 12% PVA gels and from a region of mouse articular cartilage are shown in Figure 6. Over regions of comparable size, local Young's moduli of the PVA gels varied over a much narrower range (approxi-

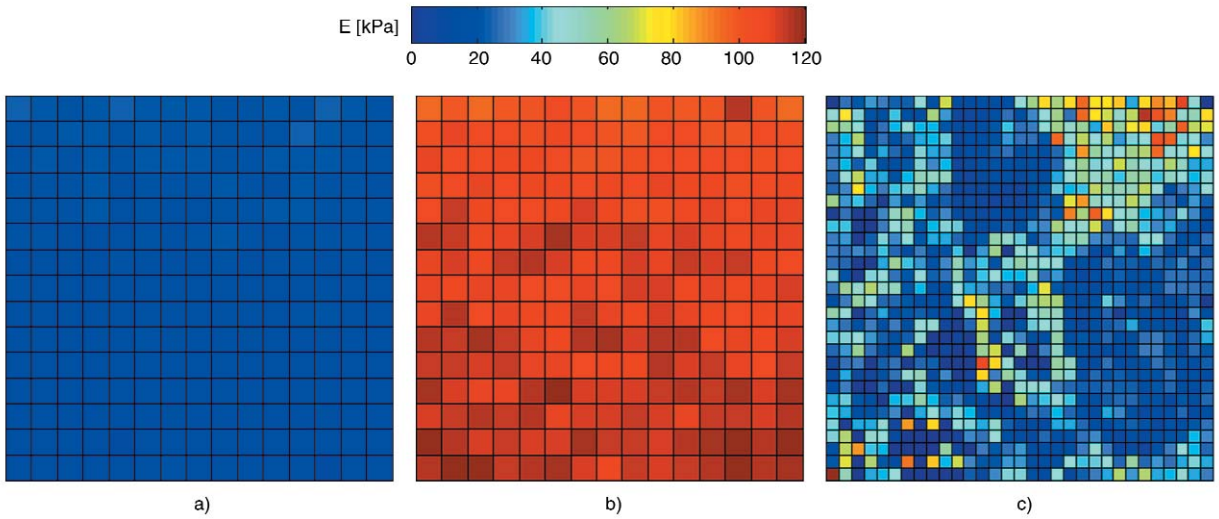

Figure 6. Sample Young's modulus (E) maps from the 'force-volume' indentation of (a) a 6% PVA gel probed using a 5.5 μm glass bead over a 20 μm × 20 μm region at a resolution of 16 × 16, (b) a 12% PVA gel probed using a 9.6 μm polystyrene bead over a 20 μm × 20 μm region at a resolution of 16 × 16 and, (c) a one-day old mouse articular cartilage sample of approximately 60 μm thickness probed using a 5 μm polystyrene bead over a 30 μm × 30 μm region at a resolution of 32 × 32. The shapes of the force-indentation curves were similar in all cases. Identical color maps are used to compare the degree of inhomogeneity between the samples. The soft regions in the cartilage (E < 25 kPa) indicate the presence of several cells.

mately 16 to 24 kPa for the 6% gel and 90 to 120 kPa for the 12% gel) than in the cartilage (< 1 to 120 kPa). The variability in stiffness in the cartilage corresponds to a high degree of local inhomogeneity, which is a characteristic feature of many biological tissues.

5. Conclusions

In rubber-like materials, measurements of elastic moduli using the AFM have been mostly limited to indentation in the linear stress-strain regime. While small strain nanoindentation is practicable in many situations, excessive noise in the vicinity of the contact point can hinder and even preclude its accuracy in other cases. Hence, an easily implemented, large strain contact mechanics model is desirable. The Mooney-Rivlin force-indentation relationship introduced here satisfies this criterion and was shown to be accurate in modeling the indentation behavior of swollen PVA gels. In the AFM probing of any material that exhibits rubber elasticity, it can be applied without the need to limit indentation strains to the linear regime.

Acknowledgements

This work was supported by the Intramural Research Program of the National Institutes of Health/National Institute of Child Health and Human Development.

References

[1] Lin D. C., Dimitriadis E. K., Horkay F.: Robust strategies for automated AFM force curve analysis – I. Non-adhesive indentation of soft, inhomogeneous materials. Journal of Biomechanical Engineering, **129**, 430–440 (2007).

[2] Lin D. C., Dimitriadis E. K., Horkay F.: Robust strategies for automated AFM force curve analysis – II. Adhesion-influenced indentation of soft, elastic materials. Journal of Biomechanical Engineering, in press (2007).

[3] Costa K. D., Yin F. C. P.: Analysis of indentation: implications for measuring mechanical properties with atomic force microscopy. Journal of Biomechanical Engineering, **121**, 462–471 (1999).

[4] Johnson K. L.: Contact mechanics. Cambridge University Press, Cambridge (1985).

[5] Johnson K. L., Kendall K., Roberts A. D.: Surface energy and the contact of elastic solids. Proceedings of the Royal Society of London, Series A: Mathematical, Physical and Engineering Sciences, **324**, 301–313 (1971).

[6] Derjaguin B. V., Muller V. M., Toporov Y. P.: Effect of contact deformations on the adhesion of particles. Journal of Colloid and Interface Science, **53**, 314–326 (1975).

[7] Tabor D.: Surface forces and surface interactions. Journal of Colloid and Interface Science, **58**, 2–13 (1976).
[8] Maugis D.: Adhesion of spheres: The JKR-DMT transition using a Dugdale model. Journal of Colloid and Interface Science, **150**, 243–269 (1992).
[9] Yoffe E. H.: Modified Hertz theory for spherical indentation. Philosophical Magazine, **50**, 813–828 (1984).
[10] Kumar M. V., Narasimhan R.: Analysis of spherical indentation of linear viscoelastic materials. Current Science, **87**, 1088–1095 (2004).
[11] Burnham N. A., Chen X., Hodges C. S., Matei G. A., Thoreson E. J., Roberts C. J., Davies M. C., Tendler S. J. B.: Comparison of calibration methods for atomic-force microscopy cantilevers. Nanotechnology, **14**, 1–6 (2003).
[12] Treloar L. R. G.: The Physics of Rubber Elasticity. Oxford University Press, Oxford (1975).
[13] Lee K. S., Wuttiphan S., Hu X., Lee S. K., Lawn B. R.: Contact-induced transverse fractures in brittle layers on soft substrates: a study on silicon nitride bilayers. Journal of the American Ceramics Society, **81**, 571–580 (1998).
[14] Mesarovic S. D. J., Fleck N. A.: Spherical indentation of elastic-plastic solids. Proceedings of the Royal Society of London, Series A: Mathematical, Physical and Engineering Sciences, **455**, 2707–2728 (1999).
[15] Bolshakov A., Pharr G. M.: Influences of pile-up on the measurement of mechanical properties by load and depth sensing indentation techniques. Journal of Materials Research, **13**, 1049–1058 (1998).
[16] McElhaney K. W., Vlassak J. J., Nix W. D.: Determination of indenter tip geometry and indentation contact area for depth-sensing indentation experiments. Journal of Materials Research, **13**, 1300–1306 (1998).
[17] Horkay F., Nagy M.: Elasticity of swollen polyvinyl alcohol and poly(vinyl acetate) networks. Polymer Bulletin, **3**, 457–463 (1980).
[18] McKenna G. B., Horkay F.: Effects of crosslinks on the thermodynamics of poly(vinyl alcohol) hydrogels. Polymer, **35**, 5737–5742 (1994).
[19] Dusek K., Prins W.: Structure and elasticity of non-crystalline polymer networks. Advances in Polymer Science, **6**, 1–102 (1969).
[20] A-Hassan E., Heinz W. F., Antonik M. D., D'Costa N. P., Nageswaran S., Schoenenberger C., Hoh J. H.: Relative microelastic mapping of living cells by atomic force microscopy. Biophysical Journal, **74**, 1564–1578 (1998).
[21] Almqvist N., Bhatia R., Primbs G., Desai N., Banerjee S., Lal R.: Elasticity and adhesion force mapping reveals real-time clustering of growth factor receptors and associated changes in local cellular rheological properties. Biophysical Journal, **86**, 1753–1762 (2004).
[22] Domke J., Dannohl S., Parak W. J., Müller O., Aicher W. K., Radmacher M.: Substrate dependent differences in morphology and elasticity of living osteoblasts investigated by atomic force microscopy. Colloids and Surfaces B: Biointerfaces, **19**, 367–379 (2000).
[23] Haga H., Sasaki S., Kawabata K., Ito E., Ushiki T., Sambongi T.: Elasticity mapping of living fibroblasts by AFM and immunofluorescence observation of the cytoskeleton. Ultramicroscopy, **82**, 253–258 (2000).
[24] Hofmann U. G., Rotsch C., Parak W. J., Radmacher M.: Investigating the cytoskeleton of chicken cardiocytes with the atomic force microscope. Journal of Structural Biology, **119**, 84–91 (1997).
[25] Touhami A., Nysten B., Dufrene Y. F.: Nanoscale mapping of the elasticity of microbial cells by atomic force microscopy. Langmuir, **19**, 4539–4543 (2003).
[26] Allen D. M., Mao J. J.: Heterogeneous nanostructural and nanoelastic properties of pericellular and interterritorial matrices of chondrocytes by atomic force microscopy. Journal of Structural Biology, **145**, 196–204 (2004).
[27] Hu K., Radhakrishnan P., Patel R. V., Mao J. J.: Regional structural and viscoelastic properties of fibrocartilage upon dynamic nanoindentation of the articular condyle. Journal of Structural Biology, **136**, 46–52 (2001).
[28] Patel R. V., Mao J. J.: Microstructural and elastic properties of the extracellular matrices of the superficial zone of neonatal articular cartilage by atomic force microscopy. Frontiers in Bioscience, **8**, 18–25 (2003).
[29] Radhakrishnan P., Lewis N. T., Mao J. J.: Zone-specific micromechanical properties of the extracellular matrices of growth plate cartilage. Annals of Biomedical Engineering, **32**, 284–291 (2004).
[30] Stolz M., Raiteri R., Daniels A. U., VanLandingham M. R., Baschong W., Aebi U.: Dynamic elastic modulus of porcine articular cartilage determined at two different levels of tissue organization by indentation-type atomic force microscopy. Biophysical Journal, **86**, 3269–3283 (2004).
[31] Tomkoria S., Patel R. V., Mao J. J.: Heterogeneous nanomechanical properties of superficial and zonal regions of articular cartilage of the rabbit proximal radius condyle by atomic force microscopy. Medical Engineering and Physics, **26**, 815–822 (2004).

eXPRESS Polymer Letters Vol.1, No.9 (2007) 585–593
Available online at www.expresspolymlett.com
DOI: 10.3144/expresspolymlett.2007.80

Complexes of heavy metals with nitrogen containing copolymers – electrochemical and physicomechanical properties

*S. Ch. Turmanova**

Department of Materials Science, Bourgas Assen Zlatarov University, Y.Yakimov Str. 1, Bourgas 8010, Bulgaria

Received 21 May 2007; accepted in revised form 8 July 2007

Absrtact. Metal complexes were synthesized on the basis of the copolymers of radiation grafted poly-4-vinylpyridine onto polyethene and polytetrafluoroethene. The formation of the complexes was carried out in solutions of the following salts: $FeCl_3 \cdot 6H_2O$, $CoCl_2 \cdot 6H_2O$, $VOSO_4 \cdot 5H_2O$, $Na_2MoO_4 \cdot 2H_2O$ and $Na_2WO_4 \cdot 2H_2O$. The introduction of metal ions depended on the degree of grafting of 4-vinylpyridine and it was found to be from 0.03 to 14.96 and from 0.11 to 34.48 mg metal ions per g of polymer carrier for polytetrafluoroethene and polyethene, respectively. The influence of the metal ion nature on the electrochemical characteristics of nitrogen-containing copolymers was studied. The specific electric resistance of the polymer metal complexes was found to depend on the nature of the metal ion and its content in the complex.
The metal complexes obtained had lower electric resistance than the initial copolymers. This can be explained with the fact that the chelate agents (salts of metals with variable valence) have free ions and electron mobility which improve the electric conductivity of the materials obtained and have a good prospect in many fields as functional polymer. The tensile characteristics of the polymer complexes of heavy metals were also affected by the nature and contents of the ions introduced.

Keywords: *mechanical properties, poly(ethene), polytetrafluoro(ethene), metal complexes, electrochemical properties*

1. Introduction

Recently, the polymer-metal complexes attracted the interest of many researchers due to their valuable electric, mechanical and thermal properties and the possibilities for their use as immobilized catalysts in various processes. The use of polymer carrier allows combining the properties of the matrix with the complex-forming ability of the ligands and reveals new perspectives for the design of new materials with an interesting complex of properties.
Radiation initiated grafting is a wide field of polymer chemistry with numerous potential applications of industrial interest. 4-vinylpyridine (4VP) is a monomer polymerizing under initiation by radiation. The surface modification of polymer materials by radiation grafting of this monomer provides possibilities to prepare grafted polymers. Poly-4-vinylpyridine (P4VP) and its copolymers are known for their versatility of the possible applications. The copolymer materials based on P4VP are used as membranes for retention of heavy metals [1–3], carriers for immobilization of biologically active substances [4], preparation of polymer adsorbents [5], polymer metal complexes with catalytically active centers [6–9] etc.
The grafted poly-4-vinylpyridine forms stable complexes with transition metal ions and ions of metals of higher valence. The presence of nitrogen containing functional groups leads to formation of metal complexes when treated with solutions of heavy metal salts. The reactions of co-ordination of

*Corresponding author, e-mail: sturmanova@btu.bg
© BME-PT and GTE

the polymer ligands with metal ion and the formation of new structures have been studied mainly by spectroscopic methods [10–12]. The introduction of a metal in the polymer chain provokes changes in polymer behavior and its surface morphology. The polymer-metal complexes contain polymer ligand which has specific structure where the central metal ions are surrounded by different polymer chains. [13].

In the present work, a modern method was used to obtain nitrogen containing copolymers – radiation grafting – which does not require the presence of initiators, allows carrying out the process in wide temperature interval and at high rates. The latter can be easily controlled by varying the dose rate. Besides, the method of radiation grafting ensures purity of the copolymers obtained.

The metal complexes of the nitrogen containing copolymers synthesized by the method described above were studied in the reaction of cyclohexene oxidation with *tert*-butylhydroperoxide [14].

The present paper reports for the preparation of the metal complexes of radiation grafted nitrogen containing copolymers. The aim of the paper is to determine the electrochemical and physicochemical properties of the complexes between polyethene or polytetrafluoroethene and grafted poly-4-vinylpyridine with salts of $FeCl_3 \cdot 6H_2O$, $CoCl_2 \cdot 6H_2O$, $VOSO_4 \cdot 5H_2O$, $Na_2MoO_4 \cdot 2H_2O$ and $Na_2WO_4 \cdot 2H_2O$, as well as to discuss their possible use in electronics.

2. Experimental part

2.1. Materials

Nitrogen containing copolymers with different degrees of grafting of 4VP onto films (40 μm) of low density polyethene (LDPE) 'Ropoten T' trade FV 03-223, commercial product of Lukoil Neftochim Co, Bourgas and polytetrafluoroethene (PTFE) 'Ftoroplast-4P', product of ONPO 'Plastpolymer', Russia and 4-vinylpyridine (4VP) (BASF, Germany). All other reagents used $FeCl_3 \cdot 6H_2O$, $CoCl_2 \cdot 6H_2O$, $VOSO_4 \cdot 5H_2O$, $Na_2MoO_4 \cdot 2H_2O$ and $Na_2WO_4 \cdot 2H_2O$, HNO_3 (Fluka, Switzerland), were analytical grade.

2.2. Preparation of graft copolymers

The poly-4-vinylpyridine copolymers (LDPE-*graft*-P4VP and PTFE-*graft*-P4VP) were obtained by radiation graft-copolymerization of 4-vinylpyridine (BASF, Germany) onto polyethene and polytetrafluoroethene films using the direct method of batch irradiation with post-effect. The irradiation was carried out with γ-rays from ^{60}Co source at dose rate of 3.5 KGy/h and doses from 1 to 35 KGy [15].

The polymer films were immersed in 240 cm^3 of 40 mass% methanol solution of the corresponding monomer placed in 250 cm^3 glass reactor. The grafting copolymerization was carried out in inert medium. The polymerization time was 2 h after each exposition and polymerization temperature was 288 K. Mohr's salt in concentration 1.5 mass% vs the methanol-monomer solution was used as inhibitor of the homopolymerization. After irradiation, the films were washed with methanol and extracted with methanol for 24 h to remove unreacted 4-vinylpyridine and its homopolymer. The copolymers obtained were dried in vacuum at 343 K until constant mass. The nitrogen containing copolymers used for the formation of complexes were with grafting degrees of 4VP from 17.1 to 74.5 mass% for polyethene and from 0.7 to 13.4 mass% for polytetrafluoroethene, respectively.

2.3. Synthesis of grafted copolymer-metal complexes

The preparation of grafted copolymer-metal complexes was carried out by treatment with 0.4 mass% aqueous solutions of $FeCl_3 \cdot 6H_2O$, $CoCl_2 \cdot 6H_2O$, $VOSO_4 \cdot 5H_2O$, $Na_2MoO_4 \cdot 2H_2O$ and $Na_2WO_4 \cdot 2H_2O$ for 12 h at 296 K under continuous stirring. The complexes of Mo^{6+} and W^{6+} were prepared in aqueous-acid solutions with pH 2.5 [16].

The treated copolymer-metal complexes were dried under vacuum at 323 K to constant mass.

2.4. Determination of metal ions content in the polymer complexes

The amount of metal ions bonded to the polymer matrix was determined spectrophotometrically on a UV/VIS Spectrometer UNIGAN 8625 at the wavelengths (λ_{max} [nm]). The amount of Mo, Co and W,

were determined spectrophotometrically by complexation with potassium rhodanide: Mo – λ = 460 nm, Co – λ = 620 nm and W – λ = 405 nm, respectively. The amount of Fe, V and Cu, were determined spectrophotometrically by complexation with sulfosalicylic acid, hydrogen peroxide and ammonia at: λ = 470 nm, λ = 450 nm and λ = 570 nm, respectively.

2.4.1. Determination of the amount of cobalt in the polymer complexes

To draw a standard curve, a standard solution containing 0.4769 g $CoSO_4 \cdot 7H_2O$ in 1000 cm^3 H_2O was prepared. The extinctions of 8–10 samples with different cobalt concentrations were measured at λ_{max} = 620 nm.

The extraction of Co^{2+} from the polymer metal complex was carried out as follows: exact amount of the sample was inundated with 10 cm^3 1n H_2SO_4 for 24 h. Then, 1g KCNS and 10 cm^3 CH_3COCH_3 were added to 10 cm^3 of the solution studied. The mixture was homogenized and the extinction at λ_{max} = 620 nm was measured.

2.4.2. Determination of the amount of iron contained in the polymer complexes

To obtain the standard straight line, a 1 cm^3 standard solution containing 0.1 mg Fe^{3+} was prepared. For this purpose, 0.49 g $FeCl_3 \cdot 6H_2O$ was dissolved in 1000 cm^3 H_2O. The extinctions of 8–10 samples containing different amounts of iron were measured at λ_{max} = 470 nm.

The iron was extracted from the polymer complex using HCl. Exactly measured sample was inundated with 10 cm^3 aqueous solution of HCl (1:3), then 5 cm^3 10 mass% solution of sulphosalicyl acid $C_7H_6O_6S \cdot 2H_2O$ were added, followed by 5 cm^3 buffer solution ($2NH_3$:$3H_2O$) to stop the observed change of solution shade. Fe^{3+} was determined as iron disalcylate. The solution volume was increased to 50 cm^3 by adding distilled water, it was homogenized and the intensity of the coloring at λ_{max} = 470 nm was measured.

2.4.3. Determination of the amount of tungsten in the polymer complexes

The standard straight line was drawn by preparing standard solution containing 0.178 g $Na_2WO_4 \cdot 2H_2O$ in 1000 cm$^3 \cdot H_2O$. The extinctions of 8–10 samples containing different amounts of tungsten were measured at λ_{max} = 405 nm.

Tungsten was extracted from the polymer complex by adding 20 cm^3 aqueous solution of HCl (1:1). Then, 5 cm^3 $SnCl_2$, 0.2 cm^3 $TiCl_3$ and 5 cm^3 20 mass% KCNS solutions were added. The solution volume was increased to 50 cm^3 by adding distilled water and the extinction at λ_{max} = 405 nm was measured.

2.4.4. Determination of the amount of molybdenum in the polymer complexes

The interaction between the molybdenum salts with rodanide ions in the presence of a reducing agent gives several molybdenum-rodanide complexes, among which $Mo(CNS)_5$ has the most intense color. Therefore, aqueous solution of ammonium paramolybdate $(NH_4)_6Mo_7O_{24} \cdot 4H_2O$ with concentration of 0.184 g/l was prepared from which 1–10 drops were taken and added into 100 cm^3 measuring flask. Then 35 cm^3 HCl (1:3), 3 cm^3 20 mass% solution of KCNS, 1g KJ and 1 cm^3 freshly prepared 1 mass% solution of $Na_2S_2O_3$ were added. The flask was vigorously agitated after adding each solution. The solution volume was increased to the mark by adding HCl and the extinction was measured after 10 min. Standard straight line was drawn describing the dependence between the extinction and mol concentration in the range 1–10 mg/l. Further, exactly measured sample was placed in 100 cm^3 flask and 35 cm^3 aqueous solution of HCl (1:3) were added. The solution was stored for 24 h to eluate Mo, then it was treated by the method described above. The extinction was measured at λ_{max} = 460 nm.

2.4.5. Determination of the amount of vanadium in the polymer complexes

In acidic medium, vanadium interacts with H_2O_2 to form yellow-orange complex. The standard solution was prepared as follows: 0.1786 g V_2O_5 (obtained by heating NH_4VO_3 at 500–550°C) was dissolved in small excess of NaOH, then it was neutralized with H_2SO_4 and distilled water was added to reach solution volume of 1000 cm^3. From this solution,1–8 cm^3 were pipetted into 50 cm^3 measuring flask and 40 cm^3 solution of 1n H_2SO_4

and 1 cm^3 3 mass% solution of H_2O_2. They were filled up to the mark with distilled water and, after 10–15 min, the extinction was measured by UV/VIS Spectrometer UNIGAN 8625 at wavelength λ_{max} = 450 nm. Standard straight line describing the dependence between the extinction and vanadium concentration was drawn.

After the extraction of vanadium from the polymer complex with 40 cm^3 1n H_2SO_4 for 24 h, vanadium concentration was determined by the method described above. The extinction was measured at λ_{max} = 450 nm.

2.5. Analyses of the metal complexes of the radiation grafted copolymers

2.5.1. Specific electric resistance

The specific electric resistance (R [ohm·m]) was determined by the mercury contact method [17]. The complexes fixed between the two compartments of a laboratory cell filled with mercury. The contact area of samples with mercury was 10^{-4}·m^2. Platinum electrodes were connected to a conductometer (OK-102/1, Hungary) The specific electric resistance (R) was calculated as the reciprocal value of the electric conductivity (γ) (Equations (1) and (2)):

$$R = \frac{1}{\gamma}\,[\Omega\cdot m] \tag{1}$$

$$\gamma = \frac{\chi d}{F}\cdot 10^4\ [S/m] \tag{2}$$

where γ – specific electric conductivity [S/m]; χ – measured electric conductivity [S]; d – thickness of the metal complexes of the radiation grafted copolymers [m].

2.5.2.Tensile properties

The tensile strength (σ [MPa]) and elongation (ε [%]) of wet film samples and metal complexes were determined according to ASTM D882 on an 'Instron' 4203 instrument at temperature of 293 K and velocity of 100 mm/min (for PTFE) and 50 mm/min (for LDPE).

2.5.3. Thermal analysis

The thermal properties of the polymers and their metal complexes were determined on an OD-102 derivatograph type, system F. Paulik–J. Paulik–L. Erdey (MOM, Budapest, Hungary) by TG curves and following conditions: rate of heating 6 K/min, temperature range 293–873 K, amount of samples 100±0.5 mg in air medium.

3. Results and discussion

Radiation initiated graft polymerization is of scientific interest in polymer chemistry due to the possibilities it offers for practical implementation of the materials obtained.

By direct irradiation from ^{60}Co γ-source, copolymers based on LDPE-*graft*-P4VP and PTFE-*graft*-P4VP were synthesized with degrees of 4VP grafting from 17.1 to 74.5% and from 0.7 to 13.4%, respectively. Methanol solution of the monomer with concentration 40 mass% was used. The basic characteristics of the copolymers synthesized as ion-exchange membranes were reported in previous papers [15].

An interaction was carried out between part of the copolymers synthesized and aqueous solutions of $FeCl_3{\cdot}6H_2O$, $CoCl_2{\cdot}6H_2O$, $VOSO_4{\cdot}5H_2O$, $Na_2MoO_4{\cdot}2H_2O$ and $Na_2WO_4{\cdot}2H_2O$ to obtain metal pyridine complexes.

Poly-4-vinylpyridine, when grafted onto LDPE and PTFE films, acts as a chelate center for some ions of transition metals (Fe^{3+} and Co^{2+}) and high valency ions (VO^{2+}, MoO_2^{2+} and WO_2^{2+}).

The mechanism of the formation of the 'polymer ions' by the reaction of molybdenyl, vanadyl and tungstenyl ones with –O– atoms was studied and described in our earlier paper [16].

The solution of $Na_2MoO_4{\cdot}2H_2O$ in aqueous solution gives molybdenyl Mo (VI) anions according to the following reaction:

$$Na_2MoO_4 \rightleftarrows 2Na^+ + MoO_4^{2-}$$

By acidic hydrolysis of the molybdenyl ions, 'polymer' anions formed following the reactions :

$$7MoO_4^{2-} + 8H^+ \rightleftarrows Mo_7O_{24}^{6-} + 4H_2O$$

$$8MoO_4^{2-} + 12H^+ \rightleftarrows Mo_8O_{26}^{4-} + 6H_2O$$

In acidic solutions, the 'polymer anions' depolymerize to form molybdenyl cation MoO_2^{2+} along the reaction:

$Mo_7O_{24}^{6-} + 20H^+ \rightleftarrows 7MoO_2^{2+} + 10H_2O$

$Mo_8O_{26}^{4-} + 20H^+ \rightleftarrows 8MoO2^{2+} + 10H_2O$

The solution of $Na_2WO_4 \cdot 2H_2O$ in acidic aqueous solutions lead to formation of tungstenate cations (WO_2^{2+}) according to similar reactions.

It is well known that vanadium ions form complex compounds with donor atoms like nitrogen, oxygen or sulfur. In aqueous solutions of vanadylsulfate, vanadium exists in the form of vanadyl (VO^{2+}) cation [18].

$VOSO_4 \rightarrow VO^{2+} + SO_4^{2-}$

In most cases, the co-ordination number of vanadium is five or six. Many complex compounds containing VO^{2+} are blue or purple colored and most often, the bidentate ligands form complexes in ratio 2:1 with VO^{2+}.

The metal complexes are formed by bonding the polymer ligands with the metal ions through a reaction between the copolymer containing donor atoms (in this case, N– atoms) and the metal ions (Fe^{3+}, Co^{2+}, VO^{2+}, MoO_2^{2+} and WO_2^{2+}). Based on our previous studies [14] and literary data [10, 19], the probable co-ordination structure of the compounds obtained is shown in Figures 1 and 2.

The amount of Fe^{3+}, Co^{2+}, VO^{2+}, MoO_2^{2+} and WO_2^{2+} in the polymer complexes was determined spectrophotometrically and the results are presented in Table 1. As can be seen, the vanadyl ions showed the highest affinity to co-ordination: 34.48 and 14.96 mg metal/g polymer carrier for LDPE-*graft*-P4VP (P = 74.5%) and PTFE-*graft*-P4VP (P = 13.4%), respectively. The amount of the metal

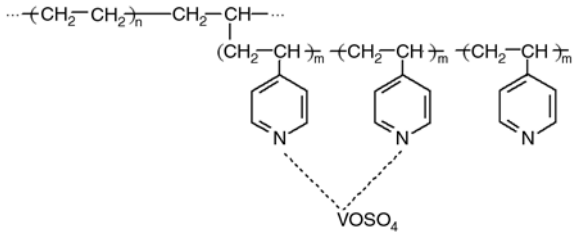

Figure 1. 1-Intramolecular co-ordination structure of PE-*graft*-P4VP-VO^{2+}

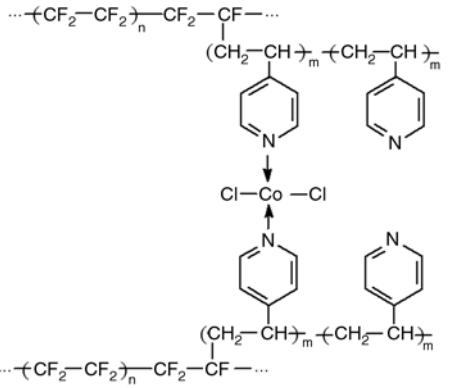

Figure 2. 2-Intermolecular co-ordination structure of PTFE-*graft*-P4VP-Co^{2+}

ions bonded to the nitrogen ligand increased with the increase of the grafting degree. The co-ordination structure of the metal complexes was analyzed using IR, Moessbauer spectroscopy and EPR in our earlier paper [14].

The content of hydrophilic groups in the grafted polymer-metal complexes stipulates their swelling in electrolytes and has strong effect on their specific electric conductivity. Figure 3. shows the semi-logarithmic dependence of the specific electric resistance (R [ohm·m]) of some of the materials obtained on the degree of grafting (P) of 4VP.

Table1. Content of metal ions in PE-*graft*-P4VP and PTFE-*graft*-P4VP [mg metal/g] polymer carrier

Polymer carrier Degree of grafting P [%]	Co^{2+}	Fe^{3+}	MoO_2^{2+}	VO^{2+}	WO_2^{2+}
PE-graft-P4VP					
17.1	0.21	2.45	3.09	18.12	0.11
35.1	0.44	3.13	4.11	23.89	0.49
39.2	0.51	3.98	4.39	26.77	0.54
66.2	0.67	4.56	4.87	29.98	0.78
69.0	0.78	4.88	4.98	32.15	0.86
74.5	0.93	5.30	5.15	34.48	1.03
PTFE-graft-P4VP					
0.7	0.08	0.03	0.11	0.98	0.02
6.5	0.56	0.14	1.56	1.87	0.12
8.2	0.87	0.45	5.67	5.98	0.25
13.4	1.45	0.72	10.93	14.96	0.53

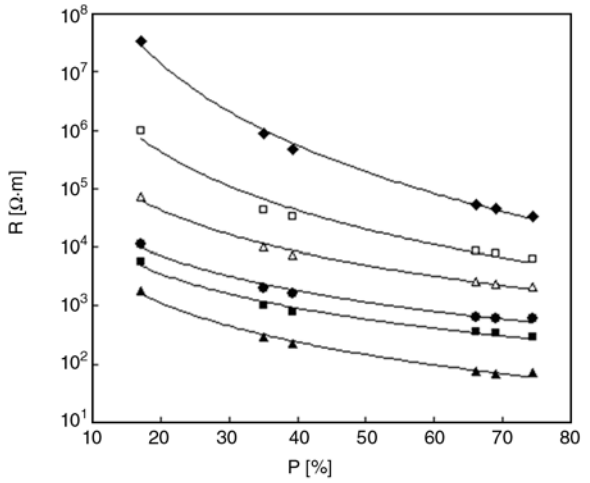

Figure 3. Dependence of the specific electric resistance (R [Ω·m]) of PE-*graft*-P4VP films (♦) and their metal complexes with Co^{2+} (□), WO_2^{2+} (Δ), MoO_2^{2+}(●), Fe^{3+} (■) and VO^{2+} (▲) on the degree of grafting of 4VP (P [%])

The change of the values of the specific electric resistance of the different complexes can be explained also with the affinity of each metal ion to formation of complexes. The metal ion changes the number of hydrophilic groups in the film and, as a result, affects materials resistance. The influences of the metal ion nature and degree of oxidation to R can be described as follows: LDPE-*graft*-P4VP > LDPE-*graft*-P4VP-Co^{2+} > LDPE-*graft*-P4VP-WO_2^{2+} > LDPE-*graft*-P4VP-MoO_2^{2+} > LDPE-*graft*-P4VP-Fe^{3+} > LDPE-*graft*-P4VP-VO^{2+}.

It can be seen from the figure that, at a grafting degree of 45%, R of the metal complexes of Fe^{3+}, Co^{2+}, MoO_2^{2+}, WO_2^{2+} and VO^{2+}, changed within the interval 10^2–10^4 Ω·m, depending on ion nature. Probably, ion associates formed at higher degrees of grafting, which are responsible for the electrochemical properties of the materials. The values of R of LDPE-*graft*-P4VP changed from 10^8 to 10^5 for degrees of grafting of 4VP from 17.1 to 74.5%. The higher electric conductivity observed (up to several orders) for the metal complexes compared to the initial copolymers were stipulated by the number and the distribution of the easier ionizing groups in the complexes. The highest electric conductivity showed the metal complexes of the copolymers with VO^{2+}. The materials obtained had lower electric resistance than that of the initial unmodified copolymers. These results can be explained with the fact that the chelating agents (salts of metals of variable valence) have free ions and electron mobility which improve their electric conductivity. Similar investigation on the specific electric resistance of metal complexes based on poly-4-vinylpyridine grafted onto polytetrafluoroethene films were also carried out. For polytetrafluoroethene, which is an excellent dielectric, the values of the specific electric resistance changed from 10^8 for the initial copolymer PTFE-*graft*-P4VP to 10^3 Ω·m for the metal complexes with transition metals and the metals with variable valence (Table 2).

The data from DTA analyses of the grafted copolymers of PE with degree of P4VP grafting 74.5%, PTFE with degree of P4VP grafting 8.1% and their metal complexes showed that the thermooxidative destruction occurs in two stages: primary thermooxidative destruction of the side chains of grafted P4VP followed by destruction of PE or PTFE polymer matrix. The complexes of all samples did not form a separate phase which would have its own stage of decomposition and, therefore, had similar melting temperatures. The starting decomposion temperature of PE and PTFE metal complexes with W and V was by 15–20 K higher than that of the initial copolymers with the same degree of P4VP grafting – Table 3. It could be suggested that 'cross-linking' takes place between the metal ions and the polymer carrier. For the complexes of PE-*graft*-P4VP with W and Mo, the first exothermal peak of destruction was shifted to higher temperatures (545–558 K), than that of the initial PE-*graft*-P4VP (520 K). This exothermal peak is due to the primary oxidation of PE, where hydroperoxides are accumulated without weight loss. Therefore, the complexes had the necessary

Table 2. Dependence of the specific electric resistance of PTFE-graft-P4VP films and their metal complexes on the degree of grafting of 4VP

Degree of grafting [%]	Specific electric resistance [Ω·m]					
	PTFE-graft-P4VP	PTFE-graft-P4VP-Co^{2+}	PTFE-graft-P4VP-Fe^{3+}	PTFE-graft-P4VP-VO^{2+}	PTFE-graft-P4VP-MoO_2^{2+}	PTFE-graft-P4VP-WO_2^{2+}
6.5	$>1.0\cdot10^{10}$	$>1.0\cdot10^{8}$	$1.4\cdot10^{7}$	$4.4\cdot10^{5}$	$2.6\cdot10^{6}$	$7.3\cdot10^{6}$
8.2	$5.0\cdot10^{9}$	$5.0\cdot10^{6}$	$1.5\cdot10^{5}$	$8.1\cdot10^{3}$	$5.3\cdot10^{4}$	$5.0\cdot10^{4}$
13.4	$1.3\cdot10^{7}$	$1.3\cdot10^{5}$	$1.3\cdot10^{5}$	$6.1\cdot10^{3}$	$4.1\cdot10^{4}$	$2.2\cdot10^{4}$

Table 3. Thermal properties of PE-*graft*-P4VP and PTFE-*graft*-P4VP copolymers and their metal complexes with grafting degree 74.5% and 8.1%

Metal complex	T_m [K]	Primary oxidation destruction ΔT [K]	Main chain destruction ΔT [K]	$T_{first\ exothermal\ peak}$ [K]
PE-*graft*-P4VP	381	494–684	684–771	520
PE-*graft*-P4VP-VO^{2+}	383	509–687	687–773	527
PE-*graft*-P4VP-WO_2^{2+}	390	514–689	689–775	545
PE-*graft*-P4VP-MoO_2^{2+}	393	504–693	693–775	558
PE-*graft*-P4VP-Fe^{3+}	390	505–691	691–772	527
PE-*graft*-P4VP-Co^{2+}	385	498–688	688–770	539
PTFE-*graft*-P4VP	604	522–634	634-853	–
PTFE-*graft*-P4VP-VO^{2+}	610	537–652	652–868	–
PTFE-*graft*-P4VP-WO_2^{2+}	615	549–660	660–872	–
PTFE-*graft*-P4VP-MoO_2^{2+}	612	530–662	662–870	–
PTFE-*graft*-P4VP-Fe^{3+}	610	526–654	654–865	–
PTFE-*graft*-P4VP-Co^{2+}	608	587–658	658–867	–

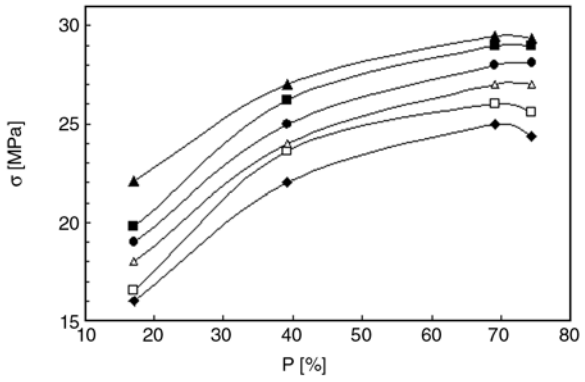

Figure 4. Dependence of the tensile strength (σ [MPa]) of LDPE-*graft*-P4VP films (♦) and their metal complexes with Co^{2+} (□), WO_2^{2+} (Δ), MoO_2^{2+}(●), Fe^{3+} (■) and VO^{2+} (▲) on the degree of grafting of 4VP (*P* [%])

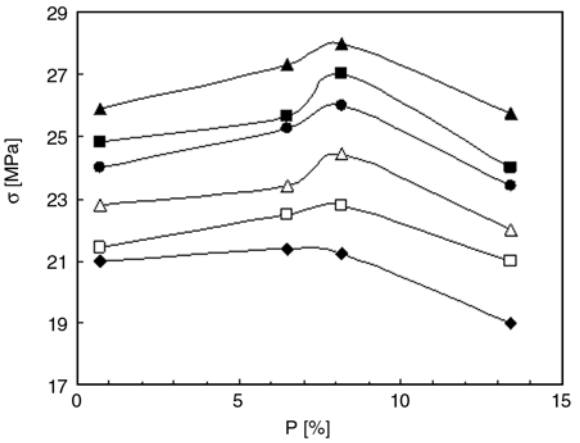

Figure 5. Dependence of the tensile strength (σ [MPa]) of PTFE-*graft*-P4VP films (♦) and their metal complexes with Co^{2+} (□), WO_2^{2+} (Δ), MoO_2^{2+}(●), Fe^{3+} (■) and VO^{2+} (▲) on the degree of grafting of 4VP (*P* [%])

thermal stability and could be used as catalysts in reactions carried out in the temperature interval 293–383 K and 293–526 K (for metal complexes based on of PE and PTFE, respectively).

The physicomechanical properties of LDPE-*graft*-P4VP and PTFE-*graft*-P4VP copolymers and their complexes with heavy metals are illustrated in Figures 4–7, respectively.

The metal complexes of LDPE-*graft*-P4VP showed clearly a tendency to increase of σ from 25 to 29 MPa at grafting degrees *P* = 60%. This increase was probably due to the formation of intermolecular associates (clusters) and additional 'cross-linking' of polymer molecules by the metal ions. At grafting degrees higher than 69% (higher content of metal ions, respectively), the mechanical strength slightly decreased. This observation can be explained with the simultaneous effects of the following factors: heterogeneity of the process of grafting, generation of stresses within the polymer matrix and decrease of the grafted layer thickness. Besides, the tensile strength of the grafted copolymers and their metal complexes measured at *P* = 69.0% changed in the following order: LDPE-*graft*-P4VP < LDPE-*graft*-P4VP-Co^{2+} < LDPE-*graft*-P4VP-WO_2^{2+} < LDPE-*graft*-P4VP-MoO_2^{2+} < LDPE-*graft*-P4VP-Fe^{3+} < LDPE-*graft*-P4VP-VO^{2+}. These results correlate well with the stability of the chelate complexes.

The metal complexes of PTFE-*graft*-P4VP showed increased strength at increased content of bonded metal (degree of grafting, respectively). Processes of radiation destruction were observed in this polymer because of the high irradiation doses, which worsened its mechanical properties. The nature of the metal ion involved exerted effect on the

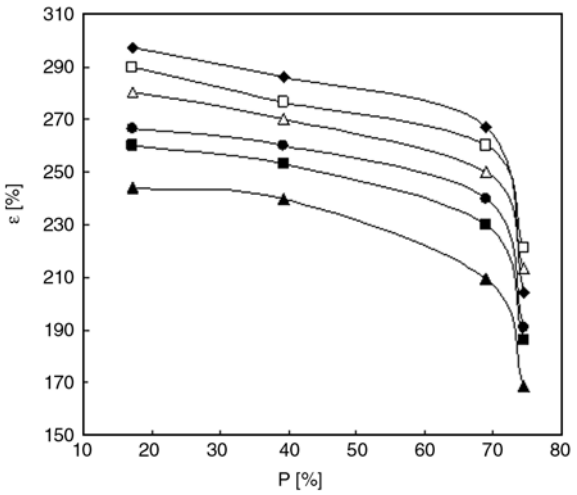

Figure 6. Dependence of the elongation (ε [%]) of LDPE-*graft*-P4VP films (♦) and their metal complexes with Co^{2+} (□), WO_2^{2+} (Δ), MoO_2^{2+}(●), Fe^{3+} (■) and VO^{2+} (▲) on the degree of grafting of 4VP (*P* [%])

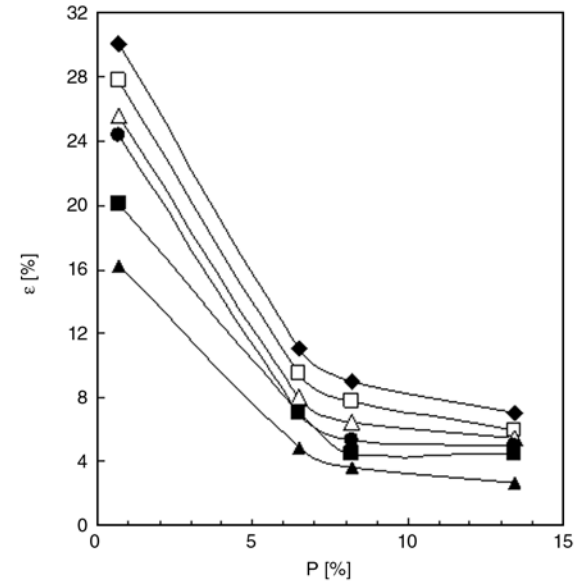

Figure 7. Dependence of the elongation (ε [%]) of PTFE-*graft*-P4VP films (♦) and their metal complexes with Co^{2+} (□), WO_2^{2+} (Δ), MoO_2^{2+}(●), Fe^{3+} (■) and VO^{2+} (▲) on the degree of grafting of 4VP (*P* [%])

mechanical strength in the following order: PTFE-*graft*-P4VP < PTFE-*graft*-P4VP-Co^{2+} < PTFE-*graft*-P4VP-WO_2^{2+} < PTFE-*graft*-P4VP-MoO_2^{2+} ≤ PTFE-*graft*-P4VP-Fe^{3+} < PTFE-*graft*-P4VP-VO^{2+}.

For all the polymer complexes studied, the elongation decreased with the increase of the degree of grafting which can be explained with the formation of physical nodes of ion associates. Another probable reason for the loss of elasticity could be related to the formation of cross-linked intra- and intermolecular structures involving the heavy metal ions present in the material. The elongation at break (ε [%]) of all the metal complexes studied decreased with the increase of the degree of grafting. It changed from 290 to 170% for the complexes of LDPE-*graft*-P4VP and from 28 to 4% for the metal complexes of PTFE-*graft*-P4VP (remaining almost the same at degree of grafting 5%) – Figures 6 and 7.

4. Conclusions

Metal complexes of radiation-grafted nitrogen-containing copolymers were obtained using radiation grafted poly-4-vinylpyridine onto films of polyethene and polytetrafluoroethene by forming complexes with solutions of the following salts: $FeCl_3 \cdot 6H_2O$, $CoCl_2 \cdot 6H_2O$, $VOSO_4 \cdot 5H_2O$, $Na_2MoO_4 \cdot 2H_2O$ and $Na_2WO_4 \cdot 2H_2O$. The introduction of metal ions in the copolymers was found to be from 0.03 to 34.48 mg metal/g and depended on the ion nature and its content in the complex. The formation of complexes with metal ions improved the electrochemical properties of the films compared to the initial copolymers. The materials obtained had electric resistance ranging from 10^8 to 10^3 Ω·m. The mechanical strength was found to increase to 29 MPa at grafting degree of 69.0% for the metal complexes of LDPE-*graft*-P4VP and to 27.5 MPa at grafting degree 8.2% for metal complexes of PTFE-*graft*-P4VP. For all the polymer metal complexes studied, the increase of the amount of metal ions in the polymer matrix resulted in a decrease of the elongation at break.

References

[1] Kariduraganavar M. Y., Nagarale R. K., Kittur A. A., Kulkarni S. S.: Ion-exchange membranes: preparative methods for electrodialysis and fuel cell applications. Desalination, **197**, 225–246 (2006).

[2] Nagarale R. K., Gohil G. S., Shahi V. K.: Recent developments on ion-exchange membranes and electro-membrane processes. Advances in Colloid and Interface Science, **119**, 97–130 (2006).

[3] Nasef M. M., Hegazy E. A.: Preparation and applications of ion exchange membranes by radiation-induced graft copolymerization of polar monomers onto non-polar films. Progress in Polymer Science, **29**, 499–561 (2004).

[4] Godjevargova T., Dayal R., Turmanova S.: Gluconic acid production in bioreactor with immobilized glucose oxidase plus catalase on polymer membranes adjacent to anion-exchange membrane. Macromolecular Bioscience, **4**, 950–956 (2004).

[5] Hegazy E. A., El-Gammal B., Khalil F. H., Mabrouk T. M.: Evaluation of anionic-and cationic-supported hydrogel membranes for sorption of Th(IV) ions from nitric acid medium. Journal of Applied Polymer Science, **102**, 320–332 (2006).

[6] Stamenova R., Tsvetanov C., Vassilev K., Tanielyan S., Ivanov S.: Polymer-supported molybdenum and vanadium catalysts for epoxidation of alkenes by alkyl hydroperoxides. Journal of Applied Polymer Science, **42**, 807–812 (1991).

[7] Cheng K. W., Chan W. K.: Morphology of rhenium complex-containing polystyrene-block-poly(4-vinylpyridine) and its use as self-assembly templates for nanoparticles. Langmuir, **21**, 5247–5250 (2005).

[8] Xi X., Liu Y., Shi J., Cao S.: Palladium complex of poly(4-vinylpyridine-*co*-acrylic acid) for homogeneous hydrogenation of aromatic nitro compounds. Journal of Molecular Catalysis A: Chemical, **192**, 1–7 (2003).

[9] Fernando H. L., Uzcátegu G. C., Ortega M. C., Rivas A. B., Yanez J. E., Alvarez J.; Pardey A. J., Longo C.: Hydroesterification and hydroformylation of 1-hexene catalyzed by rhodium complexes immobilized on poly(4-vinylpyridine). Catalysis Today, **107**, 273–281 (2005).

[10] El-Sawy N. M., Ali Z. I.: Iron(III) complexed with radiation-grafted acrylic acid onto poly(tetrafluoroethylene-co-perfluorovinyl ether) films. Journal of Applied Polymer Science, **103**, 4065–4071 (2007).

[11] El-Sawy N. M., Al Sagheer F.: Radiation-induced graft polymerization of acrylic acid onto poly(tetrafluoroethylene-perfluorovinyl ether) copolymer films: complexation with some transition metals and biological activity. European Polymer Journal, **37**, 161–166 (2001).

[12] El-Sawy N. M.: Complexation of rhodium on radiation-grafted acrylic acid onto poly(tetrafluoroethylene-perfluorovinyl ether) copolymer films. Journal of Applied Polymer Science, **67**, 1449–1455 (1998).

[13] Abdel-Ghaffar M., Hegazy E. A., Dessouki A. M., El-Assy N. B., El-Sawy N. M.: Radiation-induced graft polymerization of acrylic acid onto fluorinated polymers-II.Graft copolymer-metal complexes obtained by radiation grafting onto poly(tetrafluoroethylene-perfluorovinyl ether) copolymer. International Journal of Radiation Applications and Instrumentation, Part C: Radiation Physics and Chemistry, **38**, 369–375 (1991).

[14] Turmanova S., Vassilev K., Boneva S.: Preparation, structure and properties of metal-copolymer complexes of poly-4-vinylpyridine radiation-grafted onto polymer films. Reactive and Functional Polymers, in press (2007).

[15] Kostov G. K., Turmanova S. C.: Radiation-initiated graft copolymerization of 4-vinylpyridine onto polyethylene and polytetrafluoroethylene films and anion-exchange membranes therefrom. Journal of Applied Polymer Science, **64**, 1469–1475 (1997).

[16] Turmanova S., Vassilev K., Atanassov A.: Synthesis and properties of metal complexes of radiation grafted carboxyl containing copolymers. Journal of Applied Polymer Science, **102**, 1658–1665 (2006).

[17] Subrahmanyan V., Lakshminarayanaiah N.: A rapid method for the determination of electrical conductance of ion-exchange membranes. Journal of Physic Chemistry, **72**, 4314–4315 (1968).

[18] Clark R., Brown D.: The chemistry of vanadium, niobium and tantalum. Pergamon Press, Elmsford (1973).

[19] Hegazy E. A., Dessouki A. M., El-Sawy N. M., Abd El-Ghaffar M. A.: Radiation-induced graft polymerization of acrylic acid onto fluorinated polymers-II. Graft copolymer-metal complexes obtained by radiation grafting onto poly(tetrafluoroethylene-ethylene) copolymer. Journal of Polymer Science, Part A: Polymer Chemistry, **31**, 527–533 (1993).

eXPRESS Polymer Letters Vol.1, No.9 (2007) 594–603
Available online at www.expresspolymlett.com
DOI: 10.3144/expresspolymlett.2007.81

Copolymers of N-(4-bromophenyl)-2-methacrylamide with 2-hydroxyethyl methacrylate

*C. Soykan**, *A. Delibaş, R. Coşkun*

Department of Chemistry, Faculty of Science and Arts, University of Bozok, Yozgat, Turkey

Received 1 June 2007; accepted in revised form 8 July 2007

Abstract. The radical-initiated copolymerization of N-(4-bromophenyl)-2-methacrylamide (BrPMAAm) with 2-hydroxyethylmethacrylate (HEMA) was carried out in 1,4-dioxane solution at 70°C using 2,2'-azobisisobutyronitrile (AIBN) as an initiator with different monomer-to-monomer ratios in the feed. The copolymers were characterized by FTIR, ^{1}H- and ^{13}C-NMR spectral studies. Gel permeation chromatography was employed for estimating the weight average ($\overline{M}_w$) and number average ($\overline{M}_n$) molecular weights and polydispersity index (PDI) of the copolymers. The copolymer composition was evaluated by nitrogen content (N for BrPMAAm-units) in polymers, which allowed the determination of reactivity ratios. Monomer reactivity ratios for BrPMAAm (M_1)-HEMA (M_2) pair were determined by the application of conventional linearization methods such as Fineman-Ross (F-R), Kelen-Tüdős (KT) and Extended Kelen-Tüdős (EKT) and a non-linear error invariable model method using a computer program RREVM. The characterizations were done thermogravimetric analysis (TGA). The antimicrobial effects of polymers were also tested on various bacteria, and yeast.

Keywords: *thermal properties, N-(4-bromophenyl)-2-methacrylamide, monomer reactivity ratios, antimicrobial effects*

1. Introduction

Several studies have been done in our laboratories on the synthesis of N-monosubstituted acrylamides [1–3] and their radical copolymerization with commercial monomers. These studies clearly show that the nature as well as position of the substituent had a large effect on monomer reactivity ratios, glass transition temperatures and antimicrobial properties. Copolymers with reactive or functional monomers are gaining importance steadily. The potentially wide range of applications for functionalized polymeric materials has made these materials important. 2-Hydroxyethyl methacrylate (HEMA) hydrogels are materials with a large number of biomedical applications, such as contact lenses, artificial implants, drug delivery systemes [4, 5], due to their biocompatibility, hydrophilicity, softness, high water content and permeability. Considerable work on polymers and copolymers of HEMA has been published in the recent years [6–8]. The understanding of copolymerization kinetics has gained great importance in recent decades. Because of this fact, the prediction of monomer reactivity ratios becomes a valuable quantitative aspect. Moreover, copolymerization is an important and useful way to develop new materials. Copolymerization modulates both the intramolecular and intermolecular forces exercised between like and unlike polymer segments. Therefore, properties such as the glass transition temperature, melting point, solubility, crystallinity, permeability, adhesion, elasticity, and chemical reactivity may be varied within wide limits [9]. Most existing procedures for calculating reactivity ratios can be classified as linear least-squares (LLS), and non-linear least-squares (NLLS) methods. It is accepted that LLS methods such as those proposed by Finemann and

*Corresponding author, e-mail: soykan@erciyes.edu.tr
© BME-PT and GTE

Ross [10], and by Kelen and Tüdős [11], can only be applied to experimental data at sufficiently low conversion, because the calculation is based on the differential copolymerization equation [12]. The extended Kelen-Tüdős method [13] involves a rather more complex calculation.

We report here the homopolymer and copolymers of BrPMAAm with HEMA using different feed ratios. The copolymer composition was determined by elemental analysis. The effect of BrPMAAm content on the thermal properties of resulting copolymers was investigated. Homopolymer and copolymers were also tested for their antimicrobial properties against microorganisms such as *Staphylococcus aureus COWAN I, Bacillus subtilis ATCC 6633, Escherichia coli ATTC 25922, Klebsiella pneumonia FMCS, Pseudomonas aeruginosa DSM 50071, and yeast, Candida tropcalis ATCC 13803, Candida globrata ATCC 66032, and Candida albicans CCM 314.*

2. Experimental

2.1. Materials

BrPMAAm monomer was prepared as reported [14]. 2-hydroxyethyl methacrylate (HEMA) was purchased from Merck which was purified by vacuum distillation at 68°C/7 mmHg. α,α'-azobisisobutyronitrile (AIBN) was recrystallized from chloroform-methanol. 1,4-dioxane, diethylether, (Merck), were analytical grade commercial products and used as received.

2.2. Copolymerization

Homo- and copolymerization reactions were carried out in 1,4-dioxane using 2,2'-azobisisobutyronitrile (AIBN) as an initiator. Predetermined quantities of BrPMAAm, 2-hydroxyethyl methacrylate (HEMA), 1,4-dioxane (4 mol·l^{-1}), and AIBN were mixed in a round-bottomed flask equipped with mechanical stirrer and reflux condenser. The initiator concentration was $12 \cdot 10^{-3}$ mol·l^{-1}. The solution was purged with nitrogen for about 10 min, and the reaction mixtures were purged again for several minutes prior to heating. The reaction mixture was heated to 70°C with constant stirring. The mixtures were then cooled to room temperature and slowly poured, with constant stirring, into a large excess of diethylether that was used as a nonsolvent. Solid polymers were purified by repeated precipitation with the diethylether from solution in 1,4-dioxane and finally dried under vacuum.

2.3. Characterization techniques

Infra-red spectra were measured on a Jasco 460 Plus FT-IR spectrometer. ^{1}H- and ^{13}C-NMR spectra of the polymers were recorded in DMSO-d_6 with tetramethylsilane as the internal standard using a Gemini Varian 200 MHz NMR spectrometer. Thermal data were obtained by using a Setaram Labsys TG-DSC/DTA thermobalance in N_2 atmosphere. Elemental analyses were carried out by a LECO CHNSO-932 auto microanalyser. Molecular weight; ($\overline{M}_w$ and $\overline{M}^n$) of the polymers were determined using Waters 410 gel permeation chromatography equipped with a differential refractive index detector and calibrated with polystyrene standards.

3. Results and discussion

3.1. Copolymer characterization

The copolymerizations of BrPMAAm with HEMA can be represented according to Figure 1.

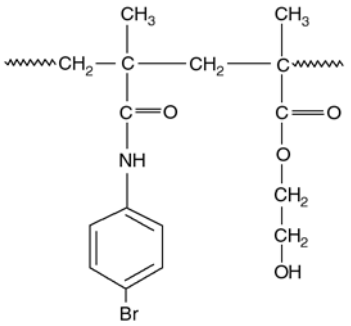

poly(BrPMAAm-co-HEMA)

Figure 1. The structure monomeric units of the copolymer

3.1.1. FTIR spectrum

The FTIR spectra of the homo- and copolymer are shown in Figure 2. The FTIR spectra confirmed the structure of polymers in all aspects. In the FTIR spectra (a) of HEMA; the broad band at 3500 cm^{-1} is the most characteristic for hydroxyl group at HEMA units. A strong band at at 1740 cm^{-1} which is attributed to the ester carbonyl of HEMA units. The other characteristic bands confirmed the structure of HEMA polymers in all aspects. In the FTIR

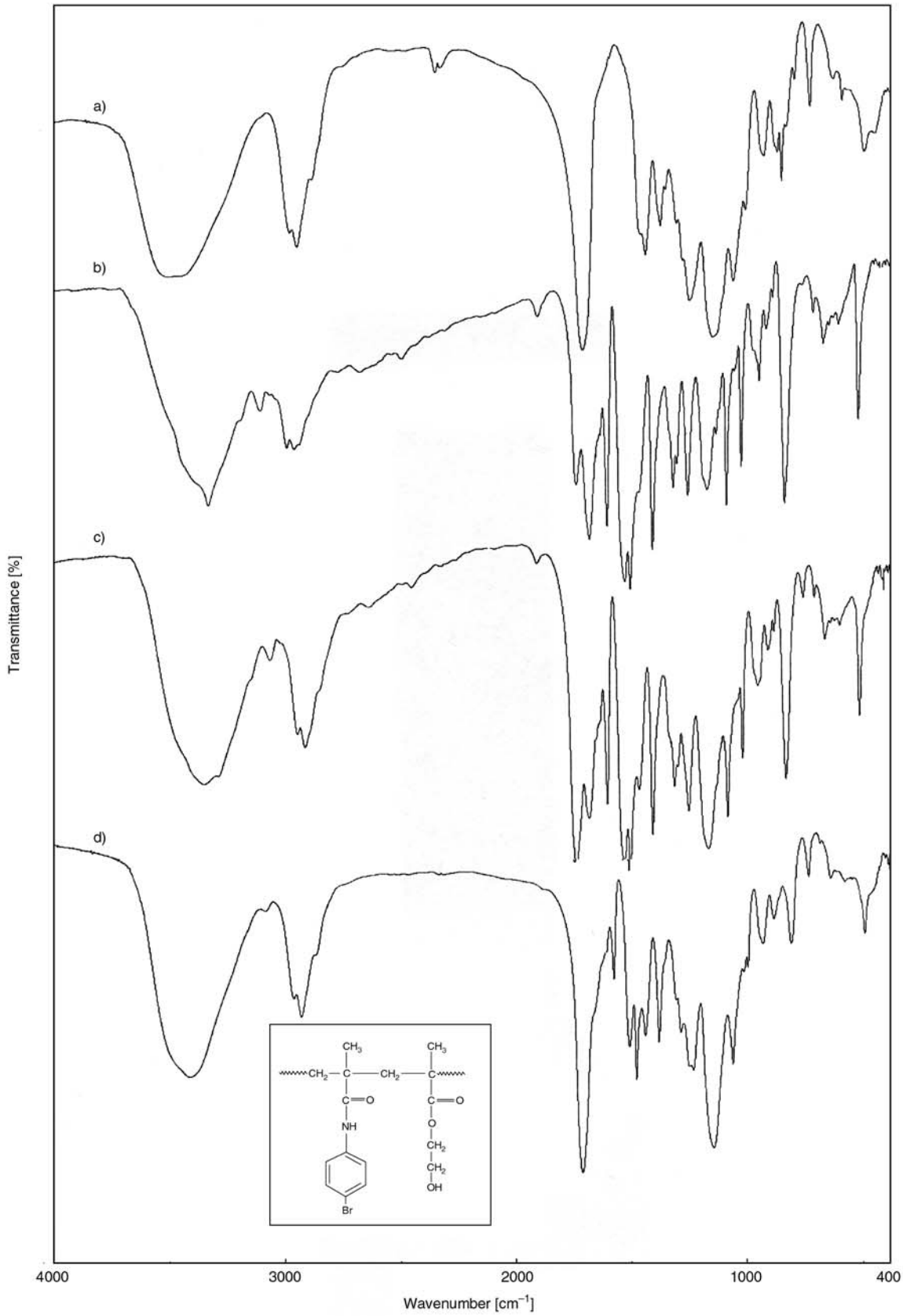

Figure 2. FTIR spectrum of a) poly(HEMA), b) poly(BrPMAAm-co-HEMA) (0.64:0.36), c) poly(BrPMAAm-co-HEMA) (0.28:0.72), and d) poly(BrPMAAm)

spectra of (b, c and d) the band at 3320 cm^{-1} (–NH in the BrPMAAm unit) is the most characteristic for the polymer. The peak at 3050 cm^{-1} corresponds to the C–H stretching of the aromatic system. The symmetrical and asymmetrical stretching bands due to the methyl and methylene groups are observed at 2985, 2940 and 2865 cm^{-1}. The peak at 1740 cm^{-1} is attributed to the ester carbonyl stretching of HEMA units. The absorption at 1700 cm^{-1} could be assigned for a complex stretching vibrations of C=O and C–N, while the strong absorption at 1300 cm^{-1} could be attributed predominantly to C–O stretching. The broad band at 1440 cm^{-1} could be due to the C–N scissoring vibration of the –N–C=O group. The ring breathing vibrations of the aromatic nuclei are observed at 1600, 1505 and 1470 cm^{-1}. The asymmetrical and symmetrical bending vibrations of methyl groups are seen at 1455 and 1380 cm^{-1}. The C–H and C=C out of plane bending vibrations of the aromatic nuclei are observed at 790 and 565 cm^{-1}, respectively.

3.1.2. ^{1}H-NMR spectrum

The ^{1}H-NMR spectra of the copolymer poly(BrPMMAm-co-HEMA) (0.61:0.39) and its assignments are shown in Figure 3a. The chemical shift assignments for the copolymers were based on the chemical shifts observed for the respective homopolymers. The resonance signals at 9.88 ppm correspond to the NH protons of the BrPMAAm unit. The aromatic protons show signals between 7.62 and 7.20 ppm. The spectrum shows two signals at 4.81 and 4.02 ppm, which are due to $–CH_2CH_2–OH$ group at HEMA units. The backbone methylene groups show signals at 1.54–2.01 ppm. The signals obtained at 1.22 and 1.10 ppm are due to the α-methyl protons of both the monomer units.

3.1.3. ^{13}C-NMR spectrum

The proton decoupled ^{13}C-NMR spectrum of the copolymer poly(BrPMMAm-co-HEMA) (0.61:0.39) and its assignments are shown in Figure 3b. The amide carbonyl of BrPMAAm appeared at 166.1 ppm while the ester carbonyl of HEMA appeared at 168.6 ppm. The aromatic carbons of BrPMAAm unit in copolymer appeared at 142.2, 136.3, 127.4 and 124.0 ppm, respectively. The hydroxyethyl carbon atoms of HEMA unit appeared at 64.4, 66.4 ppm, respectively. The signals due to the backbone methylene carbon atoms are observed at 58.2 and 56.0 ppm, while those of the tertiary carbons is observed at 45.1 and 43.3 ppm. The α-methyl carbon atoms of both monomeric units give a series of resonance signal at 18.2 ppm.

3.1.4. Molecular weights of the polymers

The molecular weights of the polymers were determined by gel permation chromatography (GPC) with polystyrene and tetrahydrofuran as the standard and solvent, respectively. The weight average ($\overline{M}_w$) and number average ($\overline{M}_n$) molecular weights and the polydispersity indexes (PDI); ($\overline{M}_w/\overline{M}_n$) of polymer samples are presented in Table 1. The

Table 1. Summary of composition and molecular weights of the Poly(BrPMAAm-co-HEMA) systema

Sample	$M_{BrPMAAm}$[b]	M_{HEMA}[c]	N [%][d]	Conv. [%][e]	$m_{BrPMAAm}$[f]	m_{HEMA}[g]	$\overline{M}_w \cdot 10^{-4}$	$\overline{M}_n \cdot 10^{-4}$	PDI[h]
Copoly-1	0.10	0.90	0.541	9.6	0.05	0.95	3.22	1.73	1.86
Copoly-2	0.20	0.80	1.439	8.2	0.14	0.86	2.88	1.65	1.75
Copoly-3	0.30	0.70	2.264	10.8	0.24	0.76	2.44	1.28	1.90
Copoly-4	0.40	0.60	2.553	7.3	0.28	0.72	2.70	1.63	1.66
Copoly-5	0.50	0.50	3.257	11.2	0.39	0.61	3.10	1.80	1.72
Copoly-6	0.60	0.40	3.598	7.3	0.45	0.55	3.08	1.73	1.78
Copoly-7	0.70	0.30	4.103	10.5	0.54	0.46	2.92	1.50	1.94
Copoly-8	0.75	0.25	4.437	7.6	0.61	0.39	2.56	1.50	1.70
Copoly-9	0.80	0.20	4.561	9.4	0.64	0.36	3.44	1.83	1.88
Copoly-10	0.90	0.10	4.974	8.7	0.74	0.26	2.78	1.65	1.68
Poly(BrPMAAm)	1.0	–	–	88.4	1.0	–	2.80	1.52	1.84
Poly(HEMA)	–	1.0	–	88.6		1.0	3.04	1.69	1.80

[a]Polymerization conditions: 1,4-dioxane solution (4 mol·l^{-1}); temperature:70±1°C; initiator:AIBN (0.1%, based on total molar of monomers) ($12 \cdot 10^{-3}$ mol·l^{-1}). [b]The molar fraction of BrPMAAm at feed. [c]The molar fraction of HEMA at feed. [d]Determined by elementeal analysis. [e]Determined by gravimetrically. [f]The molar fraction of BrPMAAm in copolymer, obtained from elementel analysis. [g]The molar fraction of HEMA in copolymer, obtained from elementel analysis. [h]Poly dispersity index.

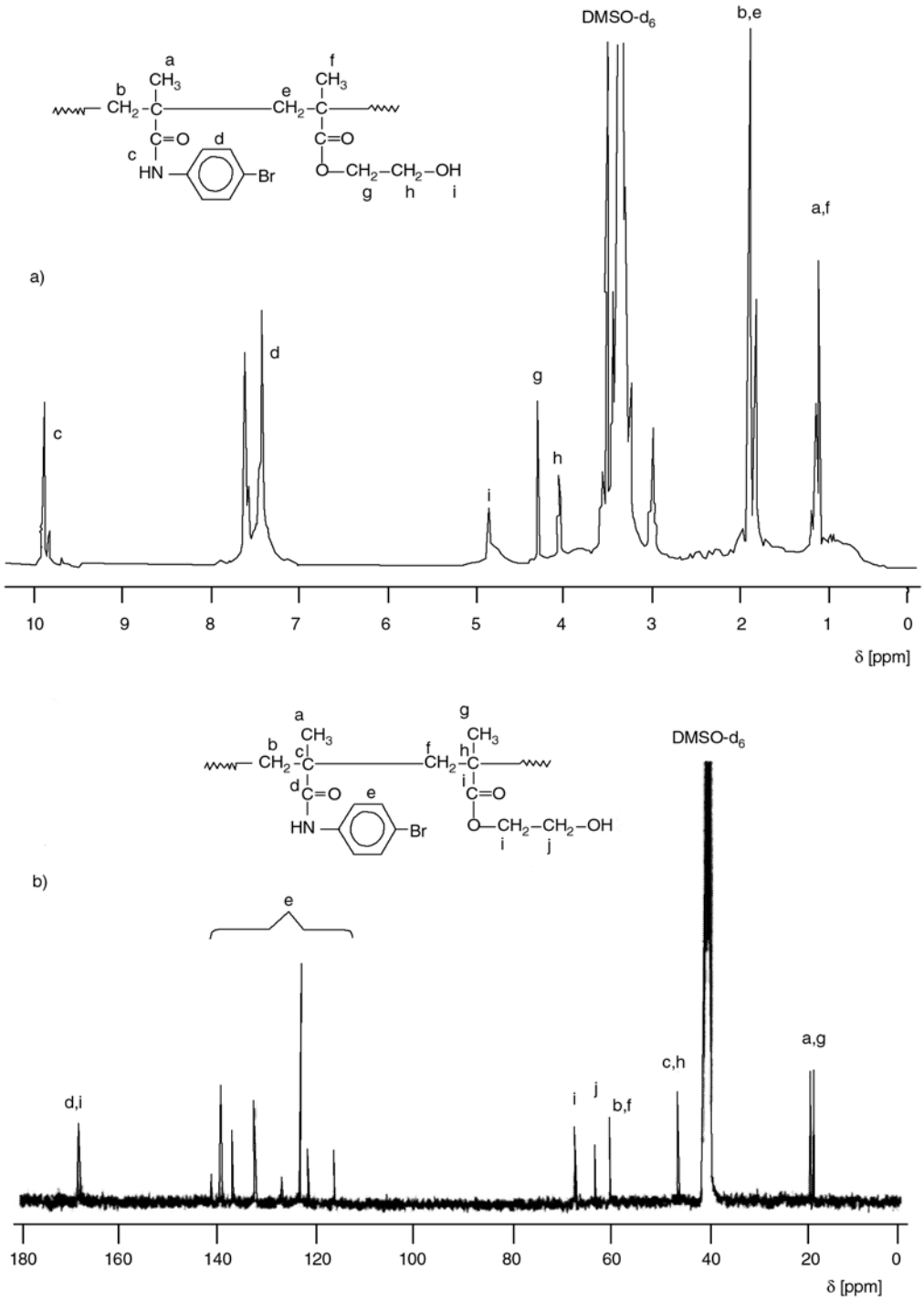

Figure 3. a) ^{1}H-NMR spectra and b) ^{13}C-NMR spectra of copoly(BrPMAAm-co-HEMA); m_1:m_2: (0.61:0.39)

polydispersity index of the polymers ranges between 1.66 and 1.94. The theoretical values of PDI for polymers produced via radical recombination and disproportionation are 1.5 and 2.0, respectively [15]. This suggests that polymers were produced mainly via termination of growing chain by disproportionation.

3.2. Copolymer composition and monomer reactivity ratios

The monomer reactivity ratios for the copolymerization of BrPMAAm with HEMA were determined from the monomer feed ratios and the copolymer composition. The classical approach for acquiring copolymer data was to isolate the copolymers from each of 10 feed compositions at early

conversions and analyze the copolymer compositions by elemental analyses. The analytical data for copolymerization of BrPMAAm with HEMA as an example are illustrated in Table 1. The plot of the mole fractions of BrPMAAm (M_1) in the feed *vs.* that in the copolymer (m_1) is shown in Figure 4. It clearly indicates that the composition of BrPMAAm in the copolymer is always lower than that in the feed. The Fineman-Ross (FR) [10], and Kelen-Tüdős (KT) [11] and Extended Kelen-Tüdős (EKT) [13] methods were used to determine the monomer reactivity ratios. The graphical plots concerning the methods previously reported are given in Figures 5, 6 and 7; whereas the reactivity ratios are summarized in Table 2. The monomer reactivity ratios determined by conventional linearization methods are only approximate and are usually employed as good starting values for non-linear parameter estimation schemes. In the determination of the monomer reactivity studies, the curves of the F-R, K-T and ext.K-T methods are quite different from straight lines, because, these methods are conventional linearization methods.

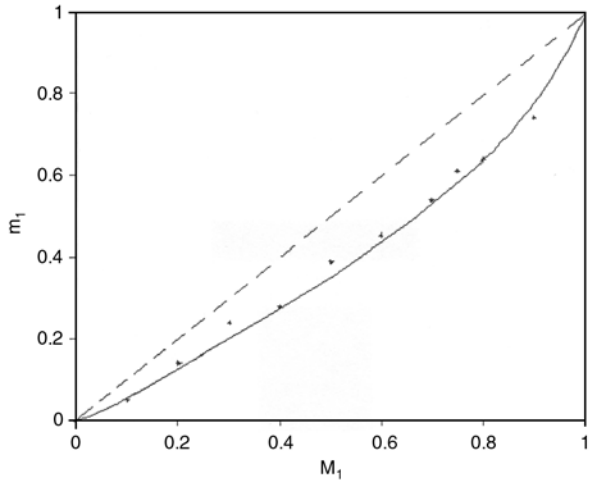

Figure 4. Copolymer composition diagram for poly(BrPMAAm-co-HEMA) system. (M_1: Feed composition in mole fraction for BrPMAAm; m_1: Copolymer composition in mole fraction for BrPMAAm).

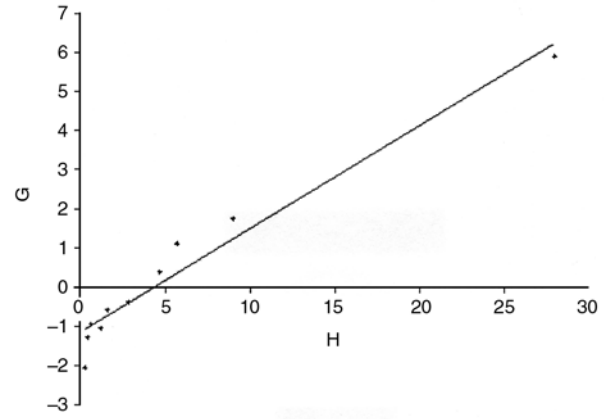

Figure 5. FR plots for determining monomer reactivity ratios in copolymerization of BrPMAAm (M_1) and HEMA (M_2) data of elemental analysis

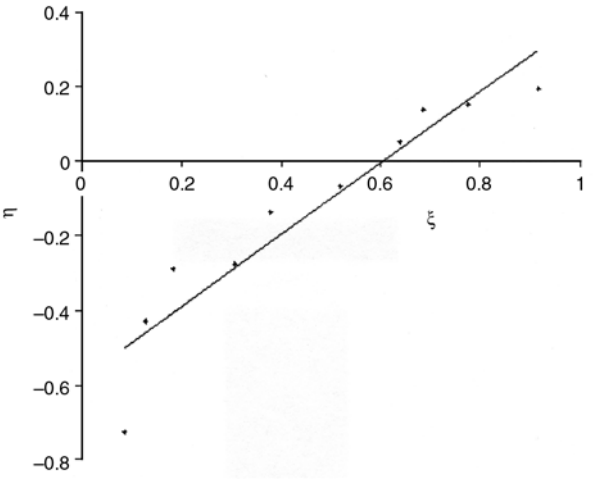

Figure 6. KT plots for determining monomer reactivity ratios in copolymerization of BrPMAAm (M_1) and HEMA (M_2) data of elemental analysis

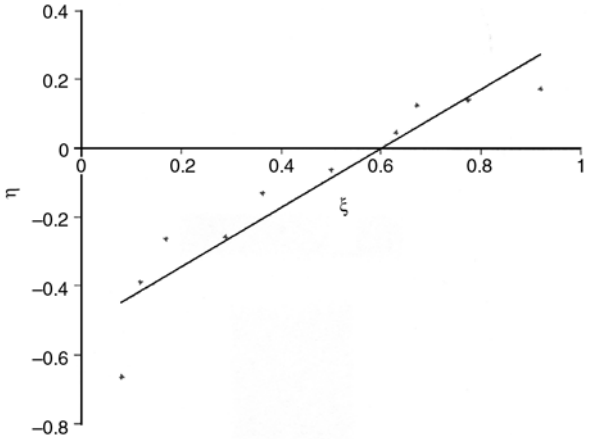

Figure 7. Ext.KT plots for determining monomer reactivity ratios in copolymerization of BrPMAAm (M_1) and HEMA (M_2) data of elemental analysis

Table 2. Comparison of the monomer reactivity ratios of BrPMAAm with HEMA by various methods

System	Methods	r_1	r_2	$r_1 \cdot r_2$	$1/r_1$	$1/r_2$
Copoly(BrPMAAm-HEMA)	F-R	0.2668	1.1374	0.3034	3.7481	0.8792
	K-T	0.3790	1.5178	0.5752	2.6385	0.6588
	Ext.K-T	0.3488	1.5275	0.5328	2.8669	0.6547
	RREVM	0.4587	1.6100	0.7385	2.1800	0.6211

To determine more reliable values of monomer reactivity ratios, a non-linear error-in-variables model (EVM) method is used utilizing the computer program, RREVM [16]. Various statistical treatments of the feed and copolymer compositions can be used to determine monomer reactivity ratios. The nonlinear methodology used selected values of r_1 and r_2, where the sum of the squares of the differences between the observed and the computed polymer compositions was minimized. With this criterion for the nonlinear least-squares method of analysis, the values for the monomer reactivity ratios were unique for a given set of data. The program produces monomer reactivity ratios for the monomers in the system with a 95% joint confidence limit determination. The joint confidence limit is a quantitative estimation of the validity of the results of the experiments and the calculations performed. This method of data analysis consists of obtaining initial estimates of the monomer reactivity ratios for the system and experimental data of comonomer charge amounts and comonomer amounts that have been incorporated into the copolymer, both in molar fractions. Tidwell and Mortimer [17] produced a nonlinear least-squares method that allowed rigorous applications of statistical analysis for reactivity ratios r_1 and r_2. This method is a modification or extension of the curve-fitting model and allows the calculations to be quantitatively analyzed. Extensive calculations are needed, but a computer program by Polic *et al.* [16] permits rapid data analysis of the nonlinear calculations. The 95% joint confidence regions for the determined r_1 and r_2 values using RREVM are shown in Figure 8. The r_1 and r_2 values from methods such as F-R, K-T, EKT and RREVM are presented in Table 2.

The microstructure of a polymeric material plays an important role in the behavior of the material toward a variety of biological systems and could be especially important in copolymerizations with monomers of different reactivities [18]. This implies that the type of copolymer prepared (i. e., random, alternating, or block) may affect the response elicited by the material in a biological environment. Monomer reactivity ratios provide a tool for estimating the average compositions of copolymers and the relative placement of reactive or functional monomers along the polymer chain [18]. The reactivity ratio values are also valuable

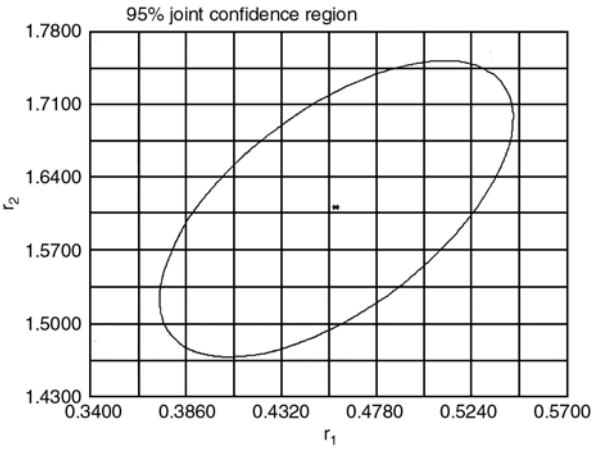

Figure 8. 95% joint confidence region of r_1 and r_2 values by RREVM for BrPMAAm-HEMA copolymer system

because the final composition of a copolymer is not simply dependent on the amounts of the two monomers present; this is especially true for monomers displaying substantial differences in the copolymerization rates. The final composition of a copolymer also depends on the method of monomer introduction, that is, whether the monomers are added all at once or incrementally over the course of the copolymerization. Both the composition and placement of monomers are dependent on the relative reactivity of each monomer in the system toward the growing polymer radicals, and vice versa.

The product of r_1 is less than 1 and r_2 is greater than 1, which indicates that the system leads to random distribution of monomer units with a longer sequence of HEMA units in the copolymer chain. Generally, neutral olefin molecules and those olefin molecules containing moderately electron-donating or electron-withdrawing groups favor free radical polymerization. HEMA consists of an electron-withdrawing ester group and an electron-donating methyl group and attached to an olefin molecule, while BrPMAAm consists of electron withdrawing phenyl amide group and an electron-donating methyl group attached to an olefin molecule. But the net charge on the HEMA molecule is less when compared to BrPMAAm, and therefore, the reactivity of HEMA is more than that of BrPMAAm. Moreover, the relative reactivity of the comonomers has to be decided not only in terms of the electronic effects, but also of the steric effects and the overall polarity of the molecule.

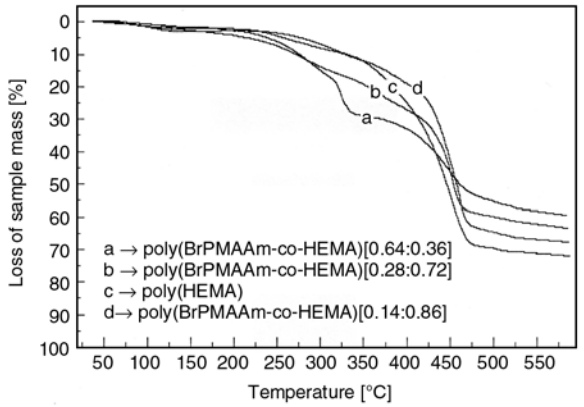

Figure 9. TGA curves of the investigated homo-and copolymers

3.3. Thermal properties

As evidenced from Figure 9, TGA curves have characteristic three-step decomposition regions. The first weight loss region appears around 50–150°C associated with dehydration of partially degradated of amide groups; secondary weight loss occurring around 150–300°C can be related to possible decarboxylation and/or other reactions of side-chain units. At last weight loss around 315–450°C indicates the main-chain degradation reactions and breakdown of the polymer backbone[18]. Copolymers show a high thermal stability which increases with increasing HEMA content in copolymers.

3.4. Antimicrobial screening

The biological activities of polymers were tested against different microorganisms using DMSO as the solvent. The sample concentrations was 100 μg. In this study, *Staphylococcus aureus COWAN I*, *Bacillus subtilis ATCC 6633, Escherichia coli ATTC 25922, Klebsiella pneumonia FMCS, Pseudomonas aeruginosa DSM 50071 have been used as bacteria, Candida tropcalis ATCC 13803, Candida globrata ATCC 66032, and Candida albicans CCM 314* as yeast.

The antibiotic sensitivities of the polymers were tested by using the antibiotic disk assay as described [19]. Muller-Hinton Agar 1.0% (w/v) beef extract, 2.0% (w/v) bactopeptone, 1.0% (w/v) glucose, 2.0% (w/v) agar was purchased from Difco. 1.5 ml of each prepared different cell culture was transferred into 20 ml of Muller-Hinton Agar (MHA) and mixed gently. The mixture was inoculated into the plate. The plates were rotated firmly and allowed to dry at room temperature for 10 minutes. Prepared antibiotic disks (100 μg) were placed on the surface of the agar medium [20]. The plates were kept at 5°C for 30 minutes then incubated at 35°C for 2 days. If a toxic compound leached out from the disc the microbial growth was inhibited around the sample. The width of this area expressed the antibacterial or antifungal activities by diffusion. The zones of inhibition of the microorganism growth of the standard samples, investigated polymers were measured with a millimeter ruler at the end of incubation period. The data reported in Table 3 are the average data of three experiments. The results were standardized against Kanamycin and Amphicillin under the same conditions. The results show that the investigated polymers have good biological activity comparable with control drugs such as Kanamycin (KAN) and Amphicillin (AMP). The first six copolymers showed good antimicrobial activities. Inhibition zone was significantly increased with HEMA content. In the case of bacteria and yeast, all copolymers allowed least growth (40–50%) were exhibited, because 2-hydroxyethyl methacrylate (HEMA) exhibits bio-

Table 3. Antimicrobial activity of compounds

	E.coli	Kleb.	Pseudo	Staph	Bacill	C.glo	C.tro	C.albi
Copoly-1	9	11	11	11	10	15	17	15
Copoly-2	8	10	11	11	9	10	11	10
Copoly-3	8	10	10	11	8	8	10	10
Copoly-4	8	8	8	10	8	8	9	8
Copoly-5	8	8	–	–	8	8	9	8
Copoly-6	8	–	–	–	8	8	8	8
Copoly-7	–	–	–	–	8	–	8	–
Copoly-8	–	–	–	–	–	–	–	–
Copoly-9	–	–	–	–	–	–	–	–
Copoly-10	–	–	–	–	–	–	–	–
KAN	20	19	21	21	22	22	22	21
AMP	19	19	23	22	21	21	22	23

compatibility, hydrophilicity, softness, high water content and permeability.

4. Conclusions

Poly(BrPMAAm) and the copolymers of BrPMAAm with HEMA were synthesized by free radical polymerization in 1,4-dioxane at 70°C. Characterization of copolymers were performed by FT-IR, ^{1}H-NMR and ^{13}C-NMR techniques. The r_1 value is less than 1, and r_2 is greater than 1. This indicates that the system forms a random copolymer with a longer sequence of HEMA units in the copolymer chain. The antimicrobial activity on the homo- and copolymers of BrPMAAm with HEMA was investigated. As the percentage of HEMA in the copolymers increases, the effectiveness of the copolymers to inhibit the growth of the microorganisms increases. It is to be remembered that the conformation the polymers acquired under experimental conditions is a factor for their antigrowth activity.

Acknowledgements

Author wish to thanks the financal support provided by the Erciyes University Research Fund (Project No: EÜBAP-FBT-05-44).

References

[1] Soykan C., Güven Ş, Coşkun R.: 2-[(5-methylisoxazol-3-yl)amino]-2-oxo-ethyl methacrylate with glycidyl methacrylate copolymers: Synthesis, thermal properties, monomer reactivity ratios and antimicrobial activity. Journal of Polymer Science, Part A. Polymer Chemistry, **43**, 2901–2911 (2005).

[2] Erol İ., Soykan C.: Free-radical-initiated copolymerization of 2-(2-naphthylamino)-2-oxo-ethyl methacrylate with methyl methacrylate and styrene. Polymer International, **53**, 1235–1244 (2004).

[3] Erol İ., Soykan C., Türkmen H., Tufan Y.: Synthesis and characterization of novel methacrylates derived from morpholine and pyrrolidine: The determination of kinetic parameters with thermogravimetric analysis. Journal of Macromolecular Science, Part A: Pure Applied Chemistry, **40**, 1213–1225 (2003).

[4] Lee P. I., Kim C. J.: Probing the mechanisms of drug release from hydrogels. Journal of Control Release, **16**, 229–236 (1991).

[5] San Román J., Madruga E. L.: Radical copolymerization of acrylic-monomers. III. stereochemical configuration of methyl methacrylate-phenyl acrylate copolymers. European Polymer Journal, **18**, 481–486 (1982).

[6] Yamashita Y., Ito K., Mizuno H., Okada K.: Synthesis of amphiphilic graft copolymers from polystyrene macromonomer. Polymer Journal, **14**, 255–260 (1982).

[7] Kumakura M., Fujimura T., Kaetsu I.: Initial stage in radiation polymerization of hydroxyethyl methacrylate water-system at low-temperatures. European Polymer Journal, **19**, 621–626 (1983).

[8] Choudhary M. S., Varma I. K.: Copolymers of 2-hydroxyethyl methacrylate and alkyl methacrylates 1: synthesis and characterization. Journal of Polymer Science: Polymer Chemistry Edition, **23**, 1917–1929 (1985).

[9] Kuo S. W., Kao H. C., Chang F. C.: Thermal behavior and specific interaction in high glass transition temperature PMMA copolymer. Polymer, **44**, 6873–6882 (2003).

[10] Finemann M., Ross S. D.: Linear method for determining monomer reactivity ratios in copolymerization. Journal of Polymer Science, **5**, 259–262 (1950).

[11] Kelen T., Tüdős F.: Analysis of the linear methods for determining copolymerization reactivity ratios. I. A new improved linear graphic method. Journal of Macromolecular Science: Pure and Applied Chemistry, **9**, 1–27 (1975).

[12] Mahdavian A. R., Abdollahi M., Mokhtabad L., Ziaee F.: Kinetic study of radical polymerization. V. Determination of reactivity ratio in copolymerization of acrylonitrile and itaconic acid by ^{1}H-NMR. Journal of Macromolecular Science: Pure and Applied Chemistry, **43**, 1583–1596 (2006).

[13] Tüdős F., Kelen T., Turcsányi B., Kennedy J. P.: Analysis of the linear methods for determining copolymerization reactivity ratios. VI. A comprehensive critical reexamination of oxonium ion copolymerizations. Journal of Polymer Science: Polymer Chemistry Edition, **19**, 1119–1132 (1981).

[14] Delibaş A., Soykan C.: Novel copolymers of N-(4-Bromophenyl)-2-methacrylamide with 2-acrylamido-2-methyl-1-propanesulfonic acid. Journal of Macromolecular Science: Pure and Applied Chemistry, **44**, 969–975 (2007).

[15] Teramachi S., Hasegawa A., Akatsuka M., Yamashita A., Takemoto N.: Molecular weight distribution and correlation between chemical composition and molecular weight in a high-conversion copolymer of styrene-methyl acrylate. Macromolecules, **11**, 1206–1210 (1978).

[16] Polic A. L., Duever T. A., Penlidis A.: Case studies and literature review on the estimation of copolymerization reactivity ratios. Journal of Polymer Science, Part A: Polymer Chemistry, **36**, 813–822 (1998).

[17] Tidwell P. M., Mortimer G. A.: An improved method of calculating copolymerization reactivity ratios. Journal of Polymer Science, Part A, **3**, 369–387 (1965).

[18] Aguilar M. R., Gallardo A., del Mar Fernandez M., San Roman J.: In situ quantitative H-1 NMR monitoring of monomer consumption: A simple and fast way of estimating reactivity ratios. Macromolecules, **35**, 2036–2041 (2002).

[19] Zhang C., Easteal A. J.: Study of poly(acrylamide-co-2-acrylamido-2-methylpropane sulfonic acid) hydrogels made using gamma radiation initiation. Journal of Applied Polymer Science, **89**, 1322–1330 (2003).

[20] Chan E. C. S., Pelczar M. J., Krieg N. R.: Agar-diffusion method. In 'Laboratory exercises in microbiology' (Eds.: Chan E. C. S., Pelczar M. J., Krieg N. R.) 225–232, McGraw-Hill, New York, USA (1993).

eXPRESS Polymer Letters Vol.1, No.9 (2007) 604–607
Available online at www.expresspolymlett.com
DOI: 10.3144/expresspolymlett.2007.82

Synthesis of gold nano-plates by mercaptide thermolysis in poly(vinyl acetate)

G. Cardone[1], G. Carotenuto[2], A. Longo[1], P. Perlo[3], L. Ambrosio[2]*

[1]Department of Materials and Production Engineering. University 'Federico II' of Naples. Piazzale Tecchio, 80 – 80125 Napoli, Italy
[2]Institute of Composite and Biomedical Materials. National Research Council. Piazzale Tecchio, 80 – 80125 Napoli, Italy
[3]FIAT Research Center, Strada Torino, 50 – 10043 Orbassano, TO Italy

Received 26 May 2007; accepted in revised form 9 July 2007

Abstract. Triangular gold nano-plates have been synthesized by thermal decomposition of Au(I) dodecyl-mercaptide (i. e., $AuSC_{12}H_{25)}$ dissolved in poly(vinyl acetate). Such special shape was achieved because of the ability of polymer side-groups (i. e., the acetate groups) to be selectively absorbed on the most acid faces of the growing gold nanocrystals, thus inhibiting crystal development along these crystallographic directions. Nano-plates had an average edge length of ca. 30 nm and a thickness of a few nanometers.

Keywords: *nanomaterials, triangular nano-plates, mercaptides, thermolysis, shape-control*

1. Introduction

Physical properties of nano-sized metals, like surface plasmon resonance, luminescence, superparamagnetism, etc., are strictly related to the microstructure [1]. Consequently, the characteristics of nanoscopic metals can be simply tuned by modifying their morphology (i. e., the particle size and shape). Size-control has represented the first approach to achieve specific physical characteristics, but also shape-control can be used for the same purpose [2]. The dependence of physical properties on particle shape makes this second approach as the most convenient to tailor specific nanostructure properties. In the last decades, shape-control has represented a great challenge for researchers working in the nanoscience area, but it is quite difficult to obtain and it has been achieved only in few cases by solution-chemistry routes based on adequate capping agents [2].

Recently, a novel *in situ* chemical route for the synthesis of metal nanoparticles confined in polymeric matrices has been developed [3]. Such approach is based on the thermal decomposition of special metal precursors (namely homoleptic mercaptides) dissolved into a polymeric medium. In this paper, the isothermal decomposition of gold dodecyl-mercaptide in poly(vinyl acetate) at a temperature of 160°C has been investigated. This polymeric growth medium for the metal phase has shown a certain ability to influence crystal development, originating a differential growth in the crystallographic directions. In particular, the polymer side-groups are selectively adsorbed on specific crystal faces (the most acid one) [4], thus inhibiting the development of these crystal faces, while the less-acid faces may grow by progressive deposition of gold atoms. However, such selective 'poisoning-effect' produced by the poly(vinyl acetate) side-groups can be well evidenced only after that a significant growth of gold crystals has occurred. Con-

*Corresponding author, e-mail: giancaro@unina.it
© BME-PT and GTE

sequently, the formation of simple polyhedral structures (nano-prisms) is observed in the system when gold nanocrystals have reached a size of several tens of nanometers. To the best of our knowledge, it is the fist time that a solid-state approach for the shape-controlled synthesis of triangular gold nanoplatelets has been described.

2. Experimental

The thermolytic organic precursor used to generate gold atoms inside the polymeric phase was Au(I) dodecyl-mercaptide (i. e., $AuSC_{12}H_{25}$) [5]. This chemical compound was synthesized by treating an ethanol solution of gold tetracholoauric acid ($HAuCl_4$, Aldrich) with an ethanol solution of 1-dodecane-thiol ($C_{12}H_{25}SH$, Aldrich) at room temperature under stirring. The obtained light-yellow solid precipitate was separated by vacuum-filtration, purified by washing with acetone, and then dissolved/dispersed in a chloroform solution of poly(vinyl acetate) (M_w = 245 000 g·mol^{-1}, Aldrich). Thin films of dry poly(vinyl acetate)/gold-mercaptide blends, containing 10% by weight of mercaptide, were obtained by solution casting from chloroform: it is worth to mention that the chloroform evaporation rate is a parameter to be set as well in order to achieve an homogeneous spatial distribution of the mercaptide inside the polymeric matrix . Gold nano-crystals were generated in the polymer phase by thermal decomposition of gold mercaptide under isothermal conditions. In particular, the heat treatment was performed at a temperature of 160°C. To avoid temperature gradients in the thermally annealed blends, the specimens were shaped in form of films which were placed between two preheated metallic plates (at ca. 160°C) to have the same temperature value on both specimen surfaces.

The obtained polymer-embedded nano-crystals were characterized by Transmission Electron Microscopy (TEM, Philips EM2085), Atomic Force Microscopy (AFM, Nanoscope IIIA, Digital Instruments), X-Ray Diffraction (XRD, Rigaku DMAX-III C), and Optical Spectroscopy (UV-Vis-NIR Spectrophotometer, HP 8453).

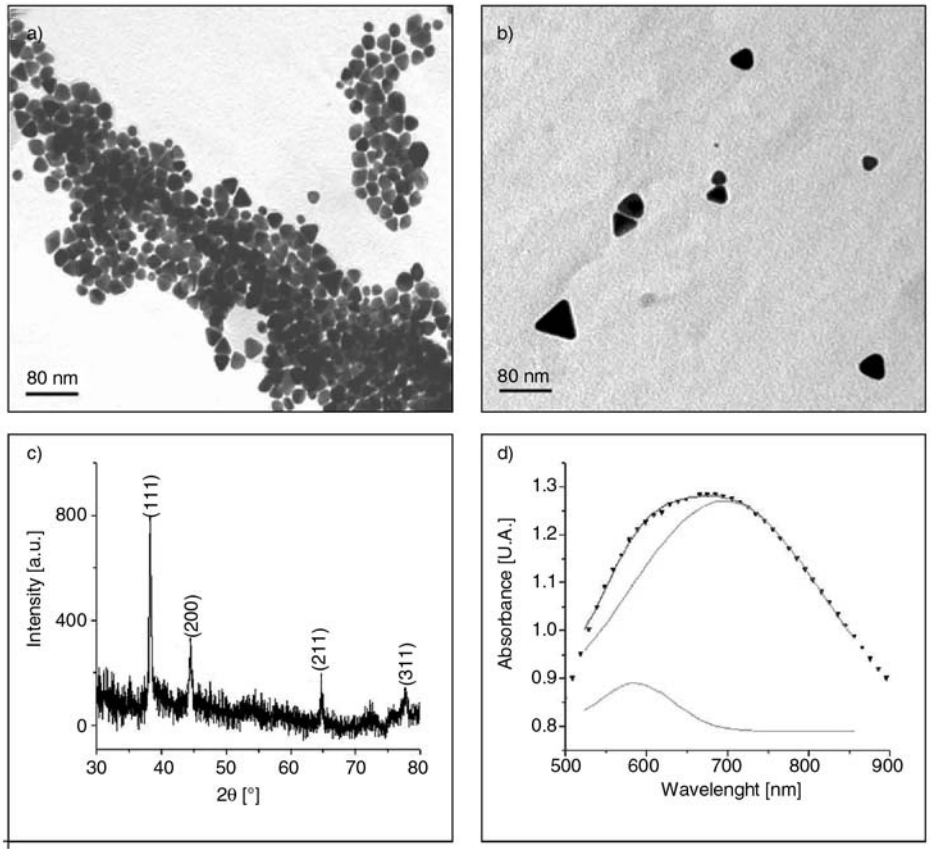

Figure 1. Gold nano-crystals characterization data: TEM-micrograph of variously shaped nano-crystals after separation/fractioning by centrifugation (a), TEM-micrograph of some isolated triangular nano-plates (b), XRD-diffraction pattern (c), and UV-Visible spectrum (d) (experimental data (▲); experimental Gaussian fit (solid black line); deconvolution of experimental data (grey lines))

3. Results

Figure 1 shows the microstructure of triangular gold nano-plates which resulted after isothermal annealing of 30 minutes at 160°C. As visible, the particles had a regular shape, consisting of simple polyhedrons, mainly made of triangular and square nano-platelets (prismatic crystals with triangular and square basal-planes). Since an uniform contrast characterized the crystal image, the presence of pyramidal geometry should be excluded. Both isolated and aggregated nanocrystals were present in the films. The average edge length of triangular nano-plates was of ca. 30 nm but a broad size-distribution characterized all samples. The thickness of nano-platelets cannot be estimated from TEM pictures but it was established by Atomic Force Microscopy (AFM). In particular, polymer-embedded gold nano-crystals were dissolved in chloroform and separated by centrifugation (6,000 rpm). Nanocrystals were dispersed in chloroform and a suspension drop was placed on a mica film for AFM observation. A thickness of ca. 2 nm can be measured by AFM investigation of the aggregated triangular nano-crystals, as the Figure 2 shows. In addition to the large nano-crystals, a low percentage of spherical gold clusters with a size inferior to 10 nm was also present in the samples.

Figure 1c shows the XRD-spectrum of polymer-embedded nano-plates. Owing to the amorphous nature of poly(vinyl acetate), only the diffraction pattern of gold phase was visible. The spectrum included tight peaks since the metallic phase had an average size of several nanometer tens. The most intensive peak was corresponding to the *[111]* plane, which is therefore the most developed crystallographic direction of triangular nano-plates [6]: such structural feature is quite common for metallic nano-plates, in fact similar structures have been found in the cases of silver, nickel, and copper nano-plates [7].

Optical properties of gold nano-crystals have been studied after their extraction from the polymeric matrix. To limit light-scattering phenomena produced by the large crystals, which significantly decreased the signal to noise ratio, optical spectra were recorded from quite dilute suspensions in chloroform. Figure 1d shows the typical optical spectrum of a gold nano-plate sample. The spectrum included a quite broad and intensive absorption band located at about 600 nm, which is

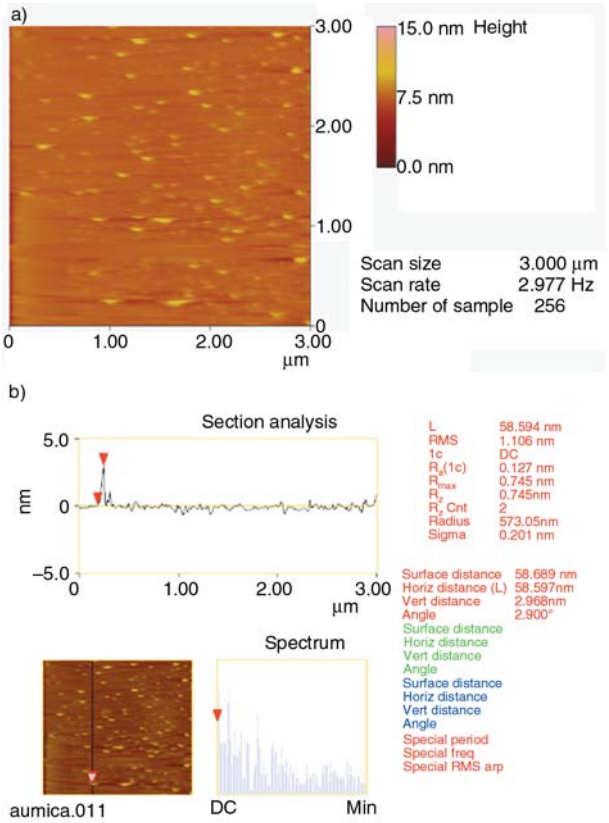

Figure 2. AFM image of gold nano-plates (a) and section analysis (b)

produced by the surface plasmon resonance of the nano-sized metallic phase. The convolution of this broad signal gives two distinct absorption bands. The band located at 580 nm can be attributed to the surface plasmon absorption of the low percentage of spherical nanoparticles present in the sample, whereas the absorption peak located at ca. 700 nm should be assigned to the in-plane quadrupole mode of gold triangular nano-plates [8].

4. Discussion

In general, an aspect of a fundamental importance to achieve nano-sized metal phases is to prevent aggregation in the produced solid. Particle aggregation can be avoided by generating the metal in a high viscous medium. Molten thermoplastic polymers have a very high viscosity and therefore they are ideal matrices for the nucleation/growth of nanometric metals. The polymeric medium should have a glass transition temperature (T_g) lower than the decomposition temperature of the metal precursor. In addition to the high viscosity also a certain ability to be absorbed on the metal surface is required for the polymer, in order to avoid metal

segregation and therefore its aggregation. When the metal phase is generated by thermal decomposition of homoleptic mercaptides, amorphous polystyrene represents a quite good material for cluster formation/growth since the glass transition temperature is not too far below the mercaptide decomposition temperature and the ability for the polymer side-groups to be lightly absorbed on the electrophilic metal surface (probably by π-electron density donation from phenyl groups to the metal). However, the faces of a metal crystal have a different ability to bond nucleophilic species, because the acidity of absorption sites depends on the metal coordination number. The quite low ability of polystyrene side-groups to be absorbed on the crystal faces is not enough to discriminate between them. Owing to the ester functions in the poly(vinyl acetate) side-groups, these molecules are preferentially absorbed on the most acid faces of the metallic crystals. Polymer absorption creates a diffusion barrier on these crystal faces, thus inhibiting their development and simplifying the polyhedral geometry. To observe such a differential growth of the crystal faces a significant crystal development is required. For such a reason, mercaptide should be slowly decomposed to generate the metal atoms required to grow nuclei by surface deposition. In the growth of triangular gold plates, thermal decomposition was performed at 160°C and the annealing treatment required more than 30 minutes to allow significant growth of metal crystals with a differential development of crystal faces. Finally, according to the LaMer model for monodispersed particle formation, a single nucleation stage must take place during the process, and then the generated nuclei should grow by addition of gold atoms to the crystal surface. During the growth stage the most acid faces do not significantly develop because of polymer absorption, leaving to a simple geometrical figure.

5. Conclusions

The possibility to obtain triangular gold nanoplates by an *in situ* synthesis based on mercaptide thermal decomposition in polymer medium has been investigated. The selection of polymer with adequately capping side-groups allows to simplify the shape of polyhedral crystals by inhibiting the development of most acid crystallographic faces. As a result, the poly(vinyl acetate) with has shown to be a good growth medium to achieve triangular nano-plates.

References

[1] Burda C., Chen X.: Chemistry and properties of nanocrystals of different shapes. Chemical Review, **105**, 1025–1102 (2005).

[2] Sun Y. G., Xia Y. N.: Shape-controlled synthesis of gold and silver nanoparticles. Science, **298**, 2176–2179 (2002).

[3] Carotenuto G., Martorana B., Perlo P., Nicolais L.: A universal method for the synthesis of metal and metal sulfide clusters embedded in polymer matrices. Journal of Material Chemistry, **13**, 2927–2930 (2003).

[4] Tannenbaum R., Reich S., Flenniken C. L., Goldberg E. P.: Shape control of iron oxide nanoclusters in polymeric media. Advanced Materials, **19**, 1402–1405 (2002).

[5] Carotenuto G., Longo A., Nicolais L.: Synthesis of molecular gold-clusters with luminescence properties by mercaptide thermolysis in polymer matrices. International Journal of Nanoscience, **6**, 65–69, (2007).

[6] Wiley B., Sun Y., Mayers B., Xia Y.: Shape-controlled synthesis of metal nanostructures: the case of silver. Chemistry-A European Journal, **11**, 454–463 (2005).

[7] Chen S., Carroll D. L.: Synthesis and characterization of truncated triangular silver nanoplates. Nano Letters, **2**, 1003–1007 (2002).

[8] Malikova N., Pastoriza-Santos I., Schierhorn M., Kotov N. A.: Layer-by-layer assembled mixed spherical and planar gold nanoparticles: control of interparticle interactions. Langmuir, **18**, 3694–3697 (2002).

eXPRESS Polymer Letters Vol.1, No.9 (2007) 608–615
Available online at www.expresspolymlett.com
DOI: 10.3144/expresspolymlett.2007.83

Effect of interfacial treatment on the thermal properties of thermal cunductive plastics

*L. M. Zhang, G. C. Dai**

State Key Laboratory of Chemical Engineering, East China University of Science and Technology, 130 Meilong Road, Shanghai 200237, P.R. China

Received 31 May 2007; accepted in revised form 14 July 2007

Abstract. In this paper, ZnO, which is processed by different surface treatment approaches, is blended together with polypropylene to produce thermal conductive polymer composites. The composites are analyzed by Fourier transform infrared (FTIR) spectroscopy and scanning electron microscopy (SEM) to investigate the surface modification of filler, their distribution in the matrix and the condition of two-phase interface. Optimized content of filler surface modifier is investigated as well. The results showed that using low-molecular coupling agent produces positive effect to improve the interface adhesion between filler and matrix, and the thermal conductivity of the composite as well. Macro-molecular coupling agent can strongly improve two-phase interface, but it is not beneficial at obtaining a high thermal conductivity. The blend of ZnO without modification and polypropylene has many defects in the two-phase interface, and the thermal conductivity of the composite is between those of composites produced by previous two approaches. The surface treatment of the filler also allowed producing the composites with lower coefficient of thermal expansion (CTE). As for the content of low-molecular coupling agent, it obtains the best effect at 1.5 wt%.

Keywords: *polymer composites, thermal conductivity, coefficient of thermal expansion, interfacial treatment, coupling agent*

1. Introduction

Thermal conductive polymer composites are normally produced by two approaches: one is to synthesize the polymers [1–2] with enhanced thermal conductivity, the other is to prepare the filled thermal conductive polymer composites [3–5]. In consideration of the difficulty of synthetic techniques, costs and many other factors, the second approach is usually adopted at present. To improve the thermal conductivity of thermal conductive polymer composites, following three approaches are very popular: firstly, it is to develop new type of thermal conductive filler, such as preparing micro-filler [6], highly oriented filler [7], 3D structure carbon fiber [8]; Secondly, it is through the surface modification of filler [9]; Thirdly, it is through the selection and optimization of the conditions of molding and processing.

At present, researches on the structure and performance of the interface of thermal conductive composites are mainly focused on their relationship with the mechanical performance of composite [10, 11], while there are very few reports about whether the two-phase interface conditions may influence the thermal conductivity of composite materials. If the relationship between the two-phase interface and thermal conductivity of materials could be nailed down, it would provide a relevant orientation for the future development of more advanced thermal conductive polymer composite.

This paper stressed the influence of filler particle surface modification on the thermal conductivity of

*Corresponding author, e-mail: gcdai@ecust.edu.cn
© BME-PT and GTE

composite. Several different types of coupling agents were tried to process the surface of filler, and the relationship between the category of coupling agent and the thermal conductivity of materials was investigated. The related principle was studied and the content of coupling agent was optimized as well.

2. Experiment

2.1. Materials

ZnO was obtained from Sinopharm Chemical Reagent Co., Ltd. (China) used for thermally conductive fillers. The matrix is a polypropylene (Y1600) supplied by SINOPEC Shanghai Petrochemical Co., Ltd. (China) (Table 1). The solvent such as iso-propylalcohol and xylene are supplied by Shanghai Dafei Industry & Trade Co., Ltd. Heqiao Branch (China).

2.2. Surface modification

Two different methods were investigated to improve the properties of the interphase.

The first is aluminium and titanium complex coupling agent (OL-AT1618, $Al(OR)_n(OOCR'')_{3-n}$ $Ti(OR')_m(OOCR'')_{4-m}$, Fine Chemicals Department of Shanxi Provincial Institute of Chemical Industry, China, 5 g) was diluted by 50 ml isopropylalcohol, and then it was added to the weighed filler. Subsequently, the filler were processed by high speed stirring at 90°C for 120 minutes. After dried at 120°C for 24 hours, the surface modified fillers with small-molecular coupling agent were obtained.

The second is fillers were modified by the titanate coupling agent (NDZ-132, $(CH_3)_2CHOTi(OOCR)_3$, Nanjing Shuguang Chemical Group Co., Ltd., China) with the same method as mentioned above.

The third is to emulsify 5 ml Silane Coupling Agent (KH550, $NH_2(CH_2)_3Si(OC_2H_5)_3$, Nanjing Shuguang Chemical Group Co., Ltd., China) with 20 ml water by emulsion machine for 30 minutes and then added it to the weighed filler. The mixture was stirred by high speed stirring for 30 minutes, put into the oven drying to constant weight at 120°C so that the surface of the filler could combine to the hydroxyl of silane coupling agent. Then, 5 g maleic anhydride grafted polypropylene wax (MPPW, Product of our lab [12]) was dissolved by 50 ml xylene, and it was added to the Silane Coupling Agent modified filler. Subsequently, the filler were processed by high speed stirring at 90°C for 120 minutes. Finally, the filler was dried at 120°C for 24 hours, which is to prepare the macro-molecular coupling agent surface modified filler (Figure 1).

2.3. Composite sample preparation and testing

A certain amount of filler and matrix in terms of the ratio was weighed. Appropriate processing temperature (190°C) was chosen according to previous experience. They were blended in the mixing mill (SK-160B, Shanghai Rubber Machinery Factory, China) for 15 minutes. Then they were taken out and directly molded a small sample of 50 mm diameter and 5~7 mm thickness. After the upper surface and undersurface of the slab is polished, the thermal coefficient of composites can be obtained by testing with Anter thermal conductivity meter (QUICKLINE-10, ANTER, USA). Thermal conductivity in the Quickline-10 is measured by the ASTM E 1530 guarded heat flow meter method.

Pick a small part from the sample and keep Soxhlet extracting with 1,2,3,4-tetrahydronaphthalene (Sinopharm Chemical Reagent Co,. Ltd., China) for 72 hours. Then, the surface graft situation of the

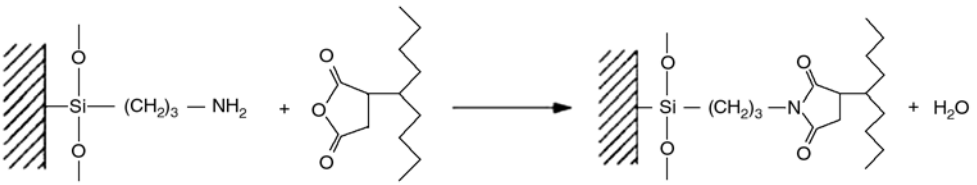

Figure 1. The reaction of the silane coupling agent with maleic anhydride grafted PP wax

Table 1. The property of ZnO and polypropylene

	Density [g/cm³]	Thermal conductivity [W/m·K]	Size [nm]	Shape
ZnO	5.6	29	200±100	grainy
Polypropylene	0.905	0.26	–	–

filler can be observed by FTIR (Magna-IR 550, THERMO NICOLET, USA).

SEM (JSM-6360LV, JEOL, Japan) was used to observe the surface graft layer of the filler and the distribution of the filler in the matrix.

CTE measurements were performed on a thermal expansion instrument (DIL 402 PC, NETZSCH, GER). The samples were heated from 25 to 145°C at a heating rate of 1°C/min. The system works according to the international standards (e.g. DIN 51045 or ASTM 831).

3. Results and discussion

3.1. The influence of different coupling agents on the thermal conductivity of composite materials

Respectively choose untreated ZnO and the ZnO processed by OL-AT1618, NDZ 132 and KH550+ MPPW, and put the filler into the mixing mill together with polypropylene for blending, molding and sampling. Then, the thermal conductivity of the materials can be obtained as shown in Figure 2. The thermal conductivity of composite made by filling polypropylene with ZnO is very low when the content of filler is very low. The difference is not obvious as shown in Table 2. However, the processing is very difficult when the content of filler is too high. Based on the experience of dozens of experiments, a content of 40 vol% is adopted. As the particle diameter of ZnO is relatively small, which is only about 200 nm, a higher content (2 wt%) is adopted for filler surface processing agent.

From Figure 2, it can be known that, when the same content is adopted, the composite material, which is blended with a low-molecular coupling agent modified filler, obtains the optimal thermal conductivity that is 1.10 W/m·K. The composite material filled with untreated ZnO obtains a lower thermal conductivity that is about 0.95 W/m·K. The composite material produced by filling polypropylene with macro-molecular modified ZnO obtains the lowest thermal conductivity that is about 0.90 W/m·K.

3.2. The influence of different contents of coupling agent on the thermal conductivity of the composite material

Choose aluminium and titanium complex coupling agent (OL-AT1618), which is relatively effective in improving the thermal conductivity of material after the filler surface treatment, then process ZnO by different concentrations at 0.5%, 1.0%, 1.5%, 2.0%, 3.0% and 5.0%. Blend the processed filler (40 vol%) and polypropylene (60 vol%) in the mixing mill, and mold to make samples. The thermal conductivities of them are shown as Figure 3.

From Figure 3, it is known that the adding of this coupling agent can considerably improve the thermal conductivity of material. Particularly, only 0.5% will result in an increase on the thermal conductivity by 10%. Then, with the increase of the content of coupling agent, the increase of thermal

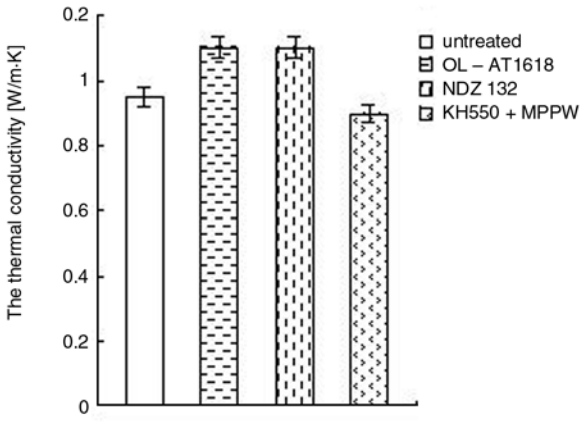

Figure 2. The influence of different filler surface treatment on the thermal conductivity of material

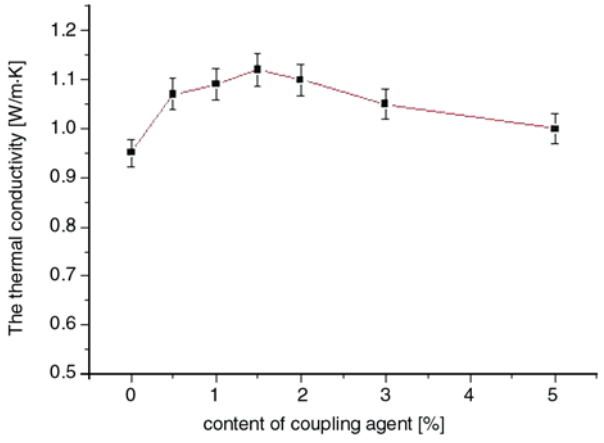

Figure 3. The influence of different content of coupling agent on the thermal conductivity

Table 2. The effect of filler treatment on thermal conductivity of composites in the same filler volume contents (23.4 vol%)

Filler (ZnO)	Untreated	OL-AT1618	NDZ 132	KH550+MPPW
Thermal conductivity [W/m·K]	0.59±0.02	0.63±0.02	0.61±0.02	0.54±0.02

conductivity is slowing down and the thermal conductivity reaches the peak when the content of coupling agent is about 1.5%. After that, the thermal conductivity starts to decrease with the further increase of coupling agent.

For this study, because the adding of low-molecular coupling agent can remarkably improve the adhesion of two-phase interfaces, the concentration of the defects in the composite materials decreases and thus the thermal conductivity of the composite will increase as well by reducing the interfacial phonon scattering between matrix and fillers [13]. Subsequently, with the increase of the content of coupling agent, such kind of improvement keeps going on and the thermal conductivity of composite is increasing slowly. Until the coupling agent finishes the monomolecular layer coverage on filler surface, the composite material obtains the highest thermal conductivity. Thereafter, the further increased coupling agent cannot combine the groups on filler surface. During processing, this part of coupling agent may enter matrix and influence its molecular chain array. Thus, the crystallization of the matrix will change as well so that its thermal conductivity will decrease. As a result, the thermal conductivity of composite will decrease accordingly.

3.3. The FTIR analysis of the surface graft situation of the filler

One gram picked sample was wrapped with filter paper. Then it was put into the Soxhlet extractor with 1,2,3,4-tetrahydronaphthalene. Seventy two hours later, the filler powders were taken out and analyzed with FTIR after drying. In Figure 4, from the top down, there are the FR-IR spectra of ZnO raw material (Spectrum 1), untreated ZnO after extraction (Spectrum 2), ZnO processed with OL-AT1618 after extraction (Spectrum 3), ZnO processed with NDZ 132 after extraction (Spectrum 4), and infrared spectrum of ZnO processed with KH550+MPPW after extraction (Spectrum 5). Spectrum 2 is very similar to spectrum 1, and the PP characteristic bands at 2953 and 2920 cm^{-1} are weak. It shows that the adhesion between untreated ZnO and PP is mainly based on physical interactions, so that the chemical bond in two-phase interface is very weak.

Spectrum 3 exhibits three characteristic bands of CH_3, CH_2, Ti–O at 2926, 2856, 1559 cm^{-1}, respec-

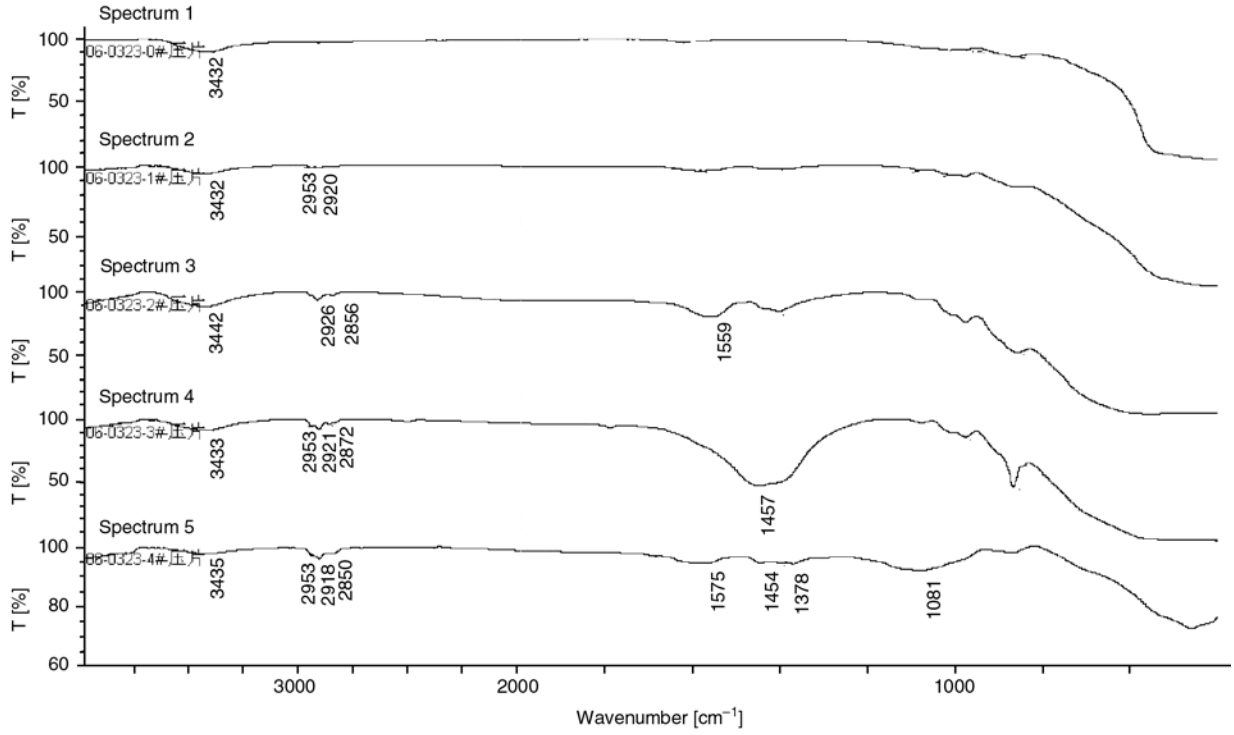

Figure 4. FTIR spectra of extracted fillers. From top down: ZnO raw material (Spectrum1), untreated ZnO after extraction (Spectrum 2), ZnO processed with OL-AT1618 after extraction (Spectrum 3), ZnO processed with NDZ 132 after extraction (Spectrum 4), and infrared spectrum of ZnO processed with KH550+MPPW after extraction (Spectrum 5)

tively, which means the surface of ZnO has combined with OL-AT 1618, while the characteristic band of Al–O bond does not appear because the content of coupling agent is too small.

In spectrum 4 there appears a broad band at 1457 cm^{-1}, which should be the result of overlapping of NDZ132 characteristic bands, such as Ti–O bond, some PP characteristic bands etc. Meanwhile, the characteristic bands of alkyl appear at 2953, 2921, 2872 cm^{-1}, which means the surface of ZnO has grafted NDZ132.

In spectrum 5 there appears the broad band of Si–O at 1081 cm^{-1}. Meanwhile the hydroxyl broad band remarkably weakens at 3435 cm^{-1}, which means lots of hydroxyls on the surface of ZnO chemically bonded KH550. In addition, the MPPW characteristic bands appear at 2953, 2918, 2850, 1454, 1378 cm^{-1} and so on, which means KH550 subsequently reacted with MPPW by chemical bonding and thus realized the task of macro-molecular modification.

3.4. The SEM analysis of filler surface

Figure 5 shows the SEM micrographs of ZnO particles. (a) is raw materials. (b), (c), (d) and (e) are respectively the untreated ZnO, the ZnO processed by OL-AT1618, the ZnO processed by NDZ132, and the ZnO processed by KH550+MPPW, obtained from the blend of ZnO/PP by Soxhlet extraction. As shown by Figure 5, most of the ZnO particle diameters range from100 to 400 nm, which are close to the nano-filler level. Thus, they have considerable surface energy and are quite easy to aggregate, which is approved by the micrograph (a). The surface condition of untreated ZnO, which is obtained from the blend by extraction, is nearly the same as ZnO raw material, and has considerable surface energy as well. Thus, micrograph (a) and micrograph (b) are very similar.

As shown by the FTIR spectrum of samples extracted from the blend, the surface of the ZnO processed by OL-AT1618, NDZ132 contains relevant graft coupling agents, which considerably modified the surface condition of the filler. So the surface energy decreases and the aggregation among particles decreases as well. During the photographing, it can be found that there is no aggregation of a large quantity of particles. Most of the particles are distributed individually as shown in micrograph (c) and (d). So after treatment of filler like this, composites will show better filler dispersion and wettability than in the case of untreated fillers. It's advantageous to improve the thermal conductivity of composite.

However, the ZnO processed by KH550+MPPW is covered by macro-molecular coupling agent on the surface, and even after extraction, there are still lots of macro-molecular chains grafted to the surface of filler. As shown in micrograph (e), after the ZnO is taken out of the extracting device and the solvent is completely dried by volatilization, the particles of ZnO are bonded together by the effect of big molecular chains.

3.5. The distribution of filler in matrix and the two-phase interface

Choose the fracture surface of all samples and the SEM micrographs can be obtained as shown in Figure 6. For untreated ZnO blended with PP, the compatibility between filler and matrix is not ideal. As shown in figure (a), most ZnO particles are directly pulled out of matrix, and the surface of particles is quite smooth and not covered by PP matrix. As for the poor compatibility, there are tiny gaps between filler and matrix, which results in the decrease of the thermal conductibility of composite on account of the interfacial phonon scattering.

Regarding the macro-molecular coupling agent processed ZnO, because the surface of filler is covered by a layer of MPPW, it presents the best compatibility with matrix. It can be seen from the SEM micrograph of figure (d), that the ZnO particles are almost all planted in the PP matrix and there is nearly no filler pulled out of the matrix. As how much the thermal conductive filler can improve the thermal conductivity of composite mainly relies on the thermal conductive network formed by filler in the matrix, when the filler is covered by a layer of polymer matrix, such a layer obviously becomes the thermal resistance layer of the thermal conductive channel, which will definitely reduce the thermal conductivity of composite.

As for ZnO processed by OL-1618 and NDZ132, when it is blended with PP, the compatibility between filler and matrix has been considerably improved. As shown in the figure (b) and (c), most of the ZnO particles on the fracture surface are still in the matrix, even the part exposed outside are covered by some PP matrix. Under such a condition, the ZnO particles can not only form a directly

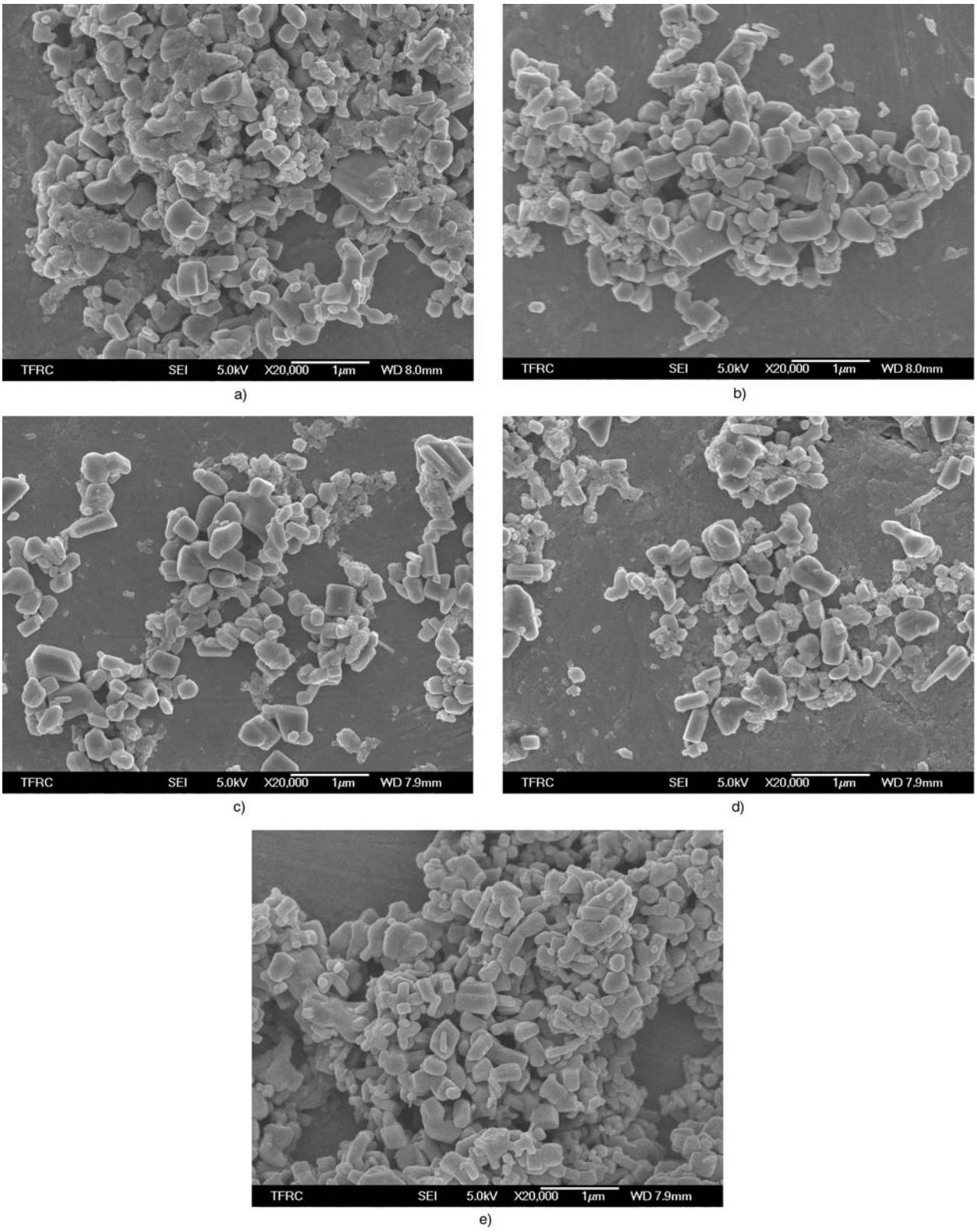

Figure 5. The SEM micrograph of filler. a) material, b) untreated, c) OL-AT 1618, d) NDZ 132, e) KH550+MPPW

interlinked network structure, but also minimized the number of tiny gaps in the interface between filler and matrix. Such a composite material can obtain the optimal thermal transmission effect.

3.6. The CTE of composites containing filler

The effect of filler treatment on CTE of composites is listed in Figure 7. As shown, the CTE of composites have been decreased effectively by treating filler. It is due to increasing wettability and disper-

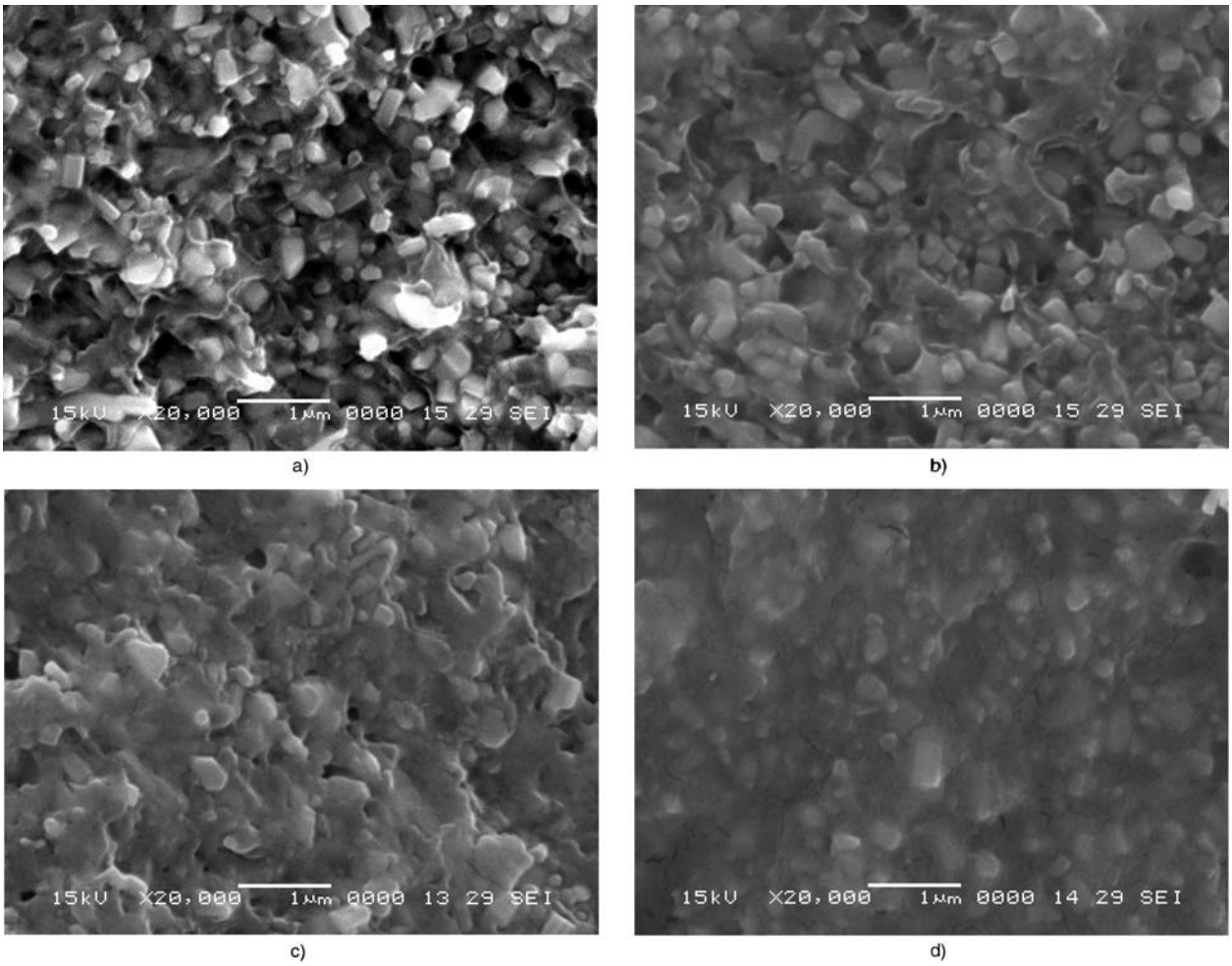

Figure 6. The SEM micrograph of fracture surface. a) untreated, b) OL-AT 1618, c) NDZ 132, d) KH550+MPPW

sion of particle filled composites [14]. There are many tiny gaps between filler and matrix in the untreated ZnO/PP blend, which is the main reason resulting in the larger CTE than the case of the treated. From Table 3, it can be found that the CTE of composites with treated filler decrease about 15% from 25 to 145°C. But the difference between the CTE of composites with filler treated with 3 kinds of coupling agent is approximate. Thus, the better adhesion of two-phase interface, the lower CTE of composites.

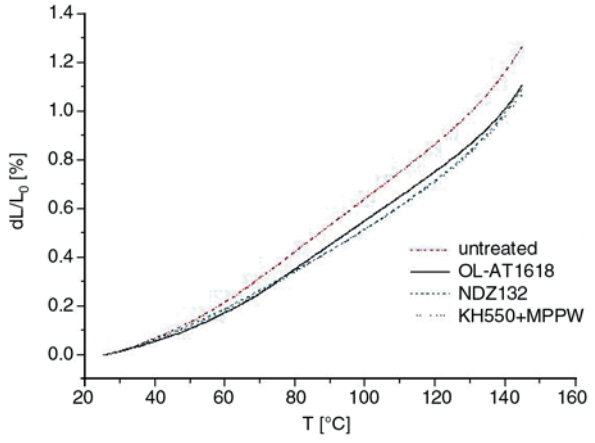

Figure 7. The effect of filler treatment on CTE of composites in the same filler contents (40 vol%)

4. Conclusions

Using low-molecular coupling agents (OL-AT1618, NDZ 132) to modify the surface of ZnO could improve the adhesion of filler and matrix interfaces and reduce the defaults in the two-phase interface so that the thermal conductivity was enhanced by minimizing the interfacial phonon scattering. Unmodified ZnO/polypropylene blend

Table 3. The CTE of composites with treated filler in the same filler contents (40 vol%) from 25 to 145°C

Filler	Untreated	OL-AT1618	NDZ132	KH550+MPPW
CTE $10^{-6}/K^{-1}$	105.7	92.4	91.2	89.2

has got many tiny gaps in the two-phase interface and then resulted in the decrease of thermal conductivity; while using the modification method of covering the surface of ZnO with macro-molecular coupling agent could remarkably improve the adhesion of two-phase interface, but seriously reduced the thermal conductivity of the composite material because of the thermal resistance layer produced by the coverage of polypropylene layer on the surface of filler.

Surface treatment of filler was found to be effective in reducing the CTE at the same filler content.

In the ZnO/polypropylene blend system, the thermal conductivity of composite increased first and then decreased with the increasing content of coupling agent. It reached the optimal value when the content of coupling agent was 1.5 wt% of filler.

References

[1] Armes S. P., Gottesfeld S., Beery J. G., Garzon F., Agnew S. F.: Conducting polymer-colloidal silica composites. Polymer, **32**, 2325–2330 (1991).

[2] Choy C. L., Luk W. H., Chen F. C.: Thermal conductivity of highly oriented polyethylene. Polymer, **19**, 155–162 (1978).

[3] Heiser J. A., King J. A.: Thermally conductive carbon filled nylon 6,6. Polymer Composites, **25**, 186–193 (2004).

[4] Wang Q., Gao J., Hua Z. K.: The high-density polyethylene composites with high thermal conductivity. CN 1246495A, China (2000).

[5] Liu G., Yi G. W.: Study on the plate heat exchangers of fluoroplastics and graphite and their applications. Chemical Equipment Technology, **19**, 26–30 (1998).

[6] Zhu J. R., Zhang X. H., Xu C. X.: Research and applications of thermal conducting polymer. Polymer Materials Science and Engineering, **16**, 17–21 (2000).

[7] Yokota H., Yamada S., Ibukiyama M.: Effect of large β-Si_3N_4 particles on the thermal conductivity of β-Si_3N_4 ceramics. Journal of the European Ceramic Society, **23**, 1175–1182 (2003).

[8] Zhao J. X.: Silicon carbide fibers and their composite. New Carbon Materials, **11**, 15–19 (1996).

[9] Toshiki K.: Polyamide composition for housing of electronic parts. JP 03 79 666, Japan (1991).

[10] Akovali G., Dilsiz N.: Studies on the modification of interphase/interfaces by use of plasma in certain polymer composite systems. Polymer Engineering and Science, **36**, 1081–1086 (1996).

[11] Qian X., Pu Y. Q., Jin Y. D.: Effect of coupling agents on mechanical properties of heat conductive plastics. Plastics, **21**, 20–22 (1992).

[12] Zhao K.: The synthesis and related application about the emulsion of acylate/polyolefin. Post doctor report. East China University of Science and Technology (2004).

[13] Berman R.: Thermal conduction in solids. Clarendon press, Oxford (1976).

[14] Lee G. W., Park M., Kim J., Lee J. I., Yoon H. G.: Enhanced thermal conductivity of polymer composites filled with hybrid filler. Composites, Part A: Applied Science and Manufacturing, **37**, 727–734 (2006).

eXPRESS Polymer Letters Vol.1, No.9 (2007) 616–621
Available online at www.expresspolymlett.com
DOI: 10.3144/expresspolymlett.2007.84

Microhardness investigation on thin films of virgin and electrically aged pure PVF and isomorphic polyblends of PVF/PVDF

A. K. Gupta, R. Bajpai, J. M. Keller*

Department of Post Graduate Studies and Research in Physics & Electronics Rani Durgavati University, Jabalpur, (M.P.), Pin-482001, India

Received 15 May 2007; accepted in revised form 25 July 2007

Abstract. Replacement of conventional materials by polymeric materials (blends/composites) with improved mechanical performance is of immense importance for modern technology. Blending of fluoro polymers can contribute to such synergistic properties. PVDF, as a semi-crystalline fluoro polymer, has been blended with PVF fluoro polymer to form isomorphic polyblend specimens by altering the wt% of PVDF using a solution casting technique. Microhardness investigations have been undertaken using the Vicker's indentation technique; measurements of Vicker's hardness number (H_v) were carried out on virgin (untreated) and electrically stressed pure PVF and PVF/PVDF isomorphic polyblend specimens by a fixed step voltage at a fixed high temperature. The results of variation of H_v as a function of applied load are explained in terms of strain hardening phenomenon in virgin samples along with their mechanical properties. The increase of hardness produced as a result of variation of PVDF wt% within the PVF matrix has been interpreted in terms of a change in chain crosslinking. The observed higher value of hardness number in the case of electrically stressed specimens is suggested to result from modification in inter- and intramolecular interactions in such samples.

Keywords: *polymer blends and alloys, microhardness, mechanical properties, electrical stress, crosslinking*

1. Introduction

Synthetic polymeric materials have been used extensively as electrical insulators because of their high electric strength and good dielectric and mechanical properties [1]. They have also made a great contribution to the miniaturization of electrical equipments [2]. In spite of such wide-spread practical uses, surprisingly little is well understood about the fundamental electrical properties of polymeric materials (electrical conduction, dielectric breakdown etc.). All electrical equipments are subjected to various severe aging effects leading to changes in mechanical behaviour of the polymeric materials. These aging factors are known to contribute more to the deterioration in electrical behaviour during operation than when the device is not in service. When the gradual aging becomes severe, the leakage current tends to increase and arcing discharge may occur. This can be interpreted as an indication of an incipient fault that will eventually lead to device failure. Thus, investigation of the mechanical performance changes is a key issue to anticipate and detect equipment incipient faults and hence its average useful life span.

Fluoropolymers, i. e. poly (vinyl fluoride) (PVF) and poly (vinylidene fluoride) (PVDF) have been used in important specialized applications. Both PVF and PVDF have good weather resistance and their mechanical properties are excellent. The two polymers are known to exhibit co-crystallinity or isomorphism on mixing. Isomorphism is believed

*Corresponding author, e-mail: rahul_jbl2006@yahoo.com
© BME-PT and GTE

to be possible when polymer chains (blend) or monomer units (co-polymers) are similar in conformation and size in the crystalline state [3]. The compatibility and the possibility of improving mechanical performance of these two polymers in blend form are of immense interest.

Microhardness testing is a well-known non-destructive technique to obtain information on structural features and change in mechanical properties of pure polymers and polymer blends [4–9]. Further, the dependence of microhardness on load in (g) was studied using Meyer's law [2] on the prepared polyblend specimens. In the present work the effects of thermal and electrical aging stress on the microhardness behaviour of pure PVF and isomorphic polyblends of PVF and PVDF have been investigated with the view to correlate the changes in mechanical properties with the useful electrical lifetime of the polymeric blend. Vicker's microhardness testing has been employed to measure the microhardness.

2. Experimental

The present investigation was undertaken on laboratory prepared samples.

2.1. Materials

Commercially available polymers of PVF (BDH, UK), with 126 000 M_w and PVDF (Aldrich, USA) with 140 000 M_w, in powder forms were supplied by M/S Redox, Jabalpur and were used without further purification. DMF, methanol and toluene were supplied by E-Merck Chemical Co. and were used as received due to their high purity (over 99%).

2.2. Preparation of samples

The solvent casting technique was utilized to prepare pure and polyblend specimens of PVF and PVDF. The polymers were dissolved in their common solvent dimethylformamide (DMF), at a temperature of 60°C with constant stirring. A known quantity of the homogeneous solution so obtained was poured on a circular glass plate of 4 cm diameter, which was balanced on a mercury pool for uniform thickness of the resulting thin film and the solvent was allowed to evaporate completely in a clean atmosphere inside an oven over nearly 6 hours. Further, for the minimization of DMF, Soxhlet test was carried out. The temperature of the oven was controlled automatically at 60°C. The specimens obtained were in the form of thin films 4 cm in diameter and 150 microns in thickness.

2.3. Soxhlet test

Soxhlet test was performed, to completely remove the DMF solvent from PVF/PVDF polyblend specimens using Soxhlet apparatus. A 30×32 mm specimen was cut from the 150 micron thick specimens and placed in the Soxhlet cavity (which was filled with toluene) and heated. The condensing toluene leaches out the DMF from the samples. This process was repeated for 2 hours, so that maximum solvent would leach out and then the residual toluene was evaporated.

3. Characterization

3.1. Microhardness measurement

Microhardness measurements on various specimens were carried out using Carl Zeiss NU_2 Universal Research Microscope model No. mph-160 with a Vicker's diamond pyramidal indenter attached to it. The Vicker's Hardness Number (H_v) was calculated using the Equation (1):

$$H_v = 1.854 \cdot \frac{L}{d^2} \text{ [MPa]} \quad (1)$$

where L is load in kg and d is diagonal of indentation in mm. Minimum five indentations were obtained at various loads and the average hardness number was calculated.

3.2. Mechanical test

Mechanical characterization of the blend films was carried out according to ASTM test method No. D-638. Crosshead speed was maintained at 5 mm/min at room temperature. The samples were conditioned at 110°C for 24 hours in air before the testing.

The tensile tests were conducted at room temperature on an Universal Testing machine (Model No. 4302). The tests were made on 4 cm^2 size samples. The crosshead speed (initial strain rate) was 5 mm/min and grip length 40 mm. In each case five samples were tested and the average of five readings was taken. The tensile strength, modulus and

elongation at break were measured using the stress-strain curves.

3.3. Thermally and electrically stressed samples

In order to investigate the effect of thermal and electrical aging on the microhardness behaviour of PVF/PVDF isomorphic blends, prepared sample of pure PVF and PVF:PVDF with varying weight percentage (50:50, 70:30 and 90:10) were electrically stressed by applying a voltage of 400 volts at 80°C. Specimens were placed between the two metal electrodes of the measuring cell, which was mounted inside an oven and heated to 80°C. After 30 min, 400 Volts was applied for a time period of 45 minutes while the temperature was maintained at 80°C. The specimen was then slowly cooled to room temperature within 45 minutes, while the electrical field was still on. The total time of application of electric field was kept at 1.5 hr in each case. The electric field was then removed and the thermally and electrically aged specimens were taken out for microhardness measurements.

4. Result and discussion

The Soxhlet extraction was performed to minimize the common solvent (DMF) from the polyblend specimens before characterization. In the Polyblend 50/50, common solvent was found to be minimum in comparison to other samples i. e. 70/30 and 90/10. The variation of Vicker's hardness number (H_v), as a function of applied load (L), is shown in Figure 1 for pure PVF and the isomorphic blends with varying weight percent of PVDF. The increase in the value of H_v, as the load increases can be explained on the basis of strain hardening phenomenon in polymers [2, 3, 10]. There are micromodes of deformation in the polymer chain. When sufficient number of micromodes becomes active, large-scale plastic deformation begins. As the load is increased, the specimen is subjected to greater strain hardening and H_v is increased. Finally, when H_v tends to saturate the polymer specimen is fully strain hardened so no appreciable change in the value of H_v is observed.

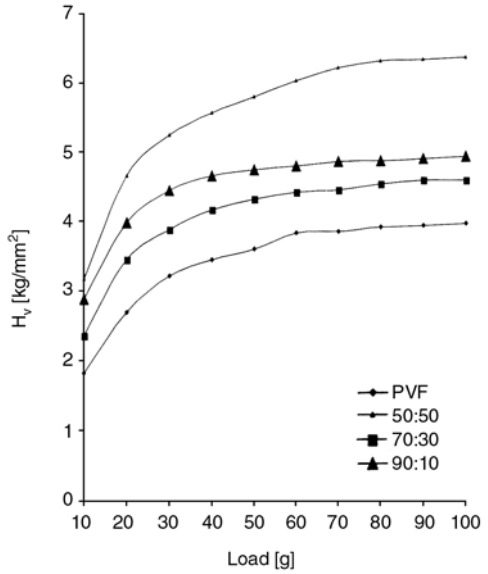

Figure 1. Variation of H_v with load for pure PVF and isomorphic polyblends of PVF:PVDF

4.1. Strain hardening index

The dependence of microhardness on load can be studied using Meyers equation (2):

$$L = a \cdot d^n \tag{2}$$

Taking logarithm of both sides of the Equation (2), we have Equation (3):

$$\log L = \log a + n \cdot \log d \tag{3}$$

where L is load, d is the length of the diagonal, a is a constant representing load for unit dimension and (n) is the logarithm index number, which is the measure of strain hardening from the plots of log$L$ versus log$d$ for pure PVF as shown in Figure 2 and as on for PVF/PVDF isomorphic polyblend specimens. For all specimens, the strain hardening index has two values: one for the low load region ranging

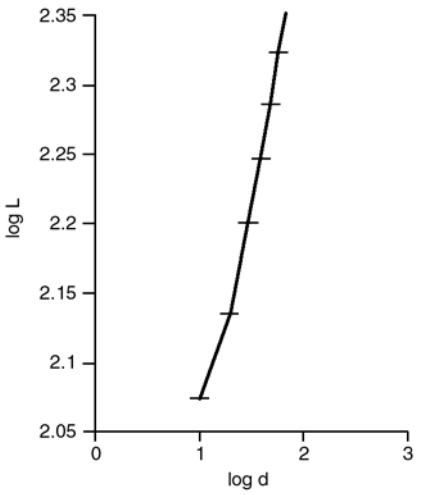

Figure 2. Graph between log$d$ *vs.* log$L$ for pure PVF for calculating values of n

Table 1. Different calculated values of (*n*) for pure PVF and blended specimens (i. e. PVF50:PVDF50, PVF70:PVDF30, PVF90:PVDF10 wt%) in the two load regions are shown

Samples	n (Slope in low regions)	n (Slope in high regions)
Pure PVF	2.93	2.33
PVF50:PVDF50 wt%	3.45	2.74
PVF70:PVDF30 wt%	3.15	2.45
PVF90:PVDF10 wt%	3.33	2.66

10 to 50 g and one for the high load region ranging from 80 to 100 g. The value of *n* is greater for low load than for high load region. In most of the blend specimens, the value of *n* tends to be nearly 2.5 in the high load region. The different values of *n* for pure PVF and PVF/PVDF isomorphic polyblend specimens in the two-load region are listed in Table 1.

Meyer's law indicates that the value of H_v increases continuously with load when n is greater than 2 and the value of *n* approaches 2 in the saturation load region when H_v becomes independent of load. Hence, the logarithmic index number, *n*, can be considered as a measure of strain hardening in different specimens. In fact the different values of n in the different load regions reflect the elastic and plastic characteristics of deformation.

4.2. Mechanical analysis

Generally mechanical properties of any polymeric system depend on the macromolecular segments and crosslinking between the macromolecular units. Tensile properties are basically characterized by measuring yield stress and corresponding elongation at break as function of polymer compositions. Tensile modulus is one of the most important small strain mechanical properties. It is the key indicator of the stiffness or rigidity of the material and quantifies the resistance of the specimens to mechanical deformation in the limit of infinitesimally small deformation. Modulus of any material is approximately proportional to the strength of the link between the atoms in a material and to the number of links per unit of cross-section area. When stress is applied, the weakest link i. e. the non-bonded interchain interaction deform much easily than the strong individual bounded chains. Thus the non-bonded interchain interactions play a crucial role in determining the magnitude of the modulus of the polymeric matrix.

Table 2. Mechanical properties of pure PVF & varying PVDF with different weight percentage in PVF

Sample designation of polyblend specimens	Tensile strength [MPa]	Tensile modulus [GPa]	Elongation [%]
Pure PVF	68.90	13.50	40.76
PVF90:PVDF10 wt%	70.50	14.00	48.00
PVF70:PVDF30 wt%	73.20	16.90	49.23
PVF50:PVDF50 wt%	78.10	18.50	50.98

The results of various mechanical properties of untreated pure PVF and its blended specimens with PVDF in varying weight percentage are given in Table 2. It can be inferred from the table that incorporation of PVDF in different wt% in PVF has significantly affected the tensile properties. PVF with different wt% of PVDF shows the increase in tensile strength (Table 2). Tensile strength was found to be greater then the neat (pure PVF), which shows the influence semi-crystalline behaviour of PVDF and crosslinking within the PVF matrix. The maximum tensile strength was obtained at 50:50 wt%.

4.3. Electrical stress analysis

Figure 3 depicts the variation of H_v as a function of applied load for specimen electrically stressed with a field of 400 kV/cm. It is evident that the microhardness exhibits similar trend as in case of virgin samples. However, the value of H_v is more for these

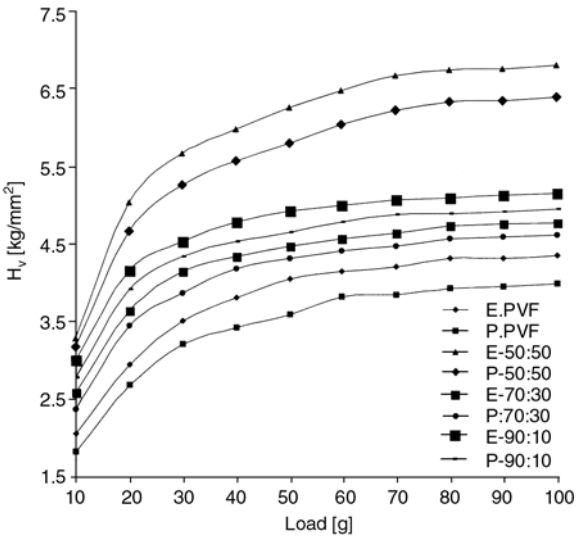

Figure 3. Variation of H_v with load for pure PVF and PVF:PVDF polyblend specimen of virgin and electrically stressed

electrically stressed samples than the virgin samples in each case.

We know that polymers have flexible chains and internal rotation of parts of chain is possible thermally [11, 12]. Owing to thermal motion the spatial arrangement of atoms keep continuously changing leading to different conformations. Each conformation corresponds to a definite value of potential energy of the molecule, which is determined by all the interactions between atoms, electrons, nuclei etc. The energy required by the molecule to move from the position with minimum potential energy to maximum potential energy is called hindrance potential or rotational barrier. If the supply of kinetic energy is small the groups of molecules do not rotate but only vibrate about the position of minimum potential energy executing restricted or retarded internal rotation. Internal rotation is retarded by interaction between atoms not bonded chemically to each other [13]. There may be interaction between atoms of the same chains (intermolecular) or between atoms belonging to units of neighbouring ionic interactions, orientational interactions, deformational interactions and dispersional interactions. Besides intramolecular hydrogen interactions are also possible. Under the influence of an external force field, chain exhibits kinetic flexibility which refers to rate of transition from one position of energy to another, chain can uncoil to a certain extent depending on the relation between the field energy and potential energy barrier. The rate of conformational transformation depends on the ratio of potential energy barrier and the energy of external influence. Thus rotation of units and their passage from one position of potential energy minimum to another can occur only when there is ample supply of energy. Further polymer links can assume only those positions in space allowed by the presence of an interaction. Thus owing to intermolecular interactions a real polymer chain assumes a smaller number of conformations than a freely joined chain. With insufficient supply of energy its units do not rotate but exhibit only torsional vibrations. Polymers with intense torsional vibrations are flexible chain polymers while polymers with hindered rotation of chain parts are called rigid chain polymers. Prior to the application of the electrical stress field the sample were kept maintained at a high temperature for half an hour facilitating thermal movements of chains. Subsequent application of the electrical stress at this elevated temperature and hence the directing action of the applied field acting on the polarizing (moieties) results in polarization of the polymer and this state is frozen in on cooling. It appears that in electrically stressed polarized samples inter- and intramolecular interactions are modified in such a way that steric hindrance of rotation of chain or potential rotational barrier is increased restricting kinetic flexibility of polymer chain. This result in a material, which is hard compared to the virgin untreated sample, which is also assured from the calculated value of (n) for electrically stressed specimens as shown in Table 3 and increase in mechanical strength (Table 4). This explains the increase in the value of H_v observed for electrically stressed samples in the present case.

Table 3. Different calculated values of (n) for electrically stressed pure PVF and blended specimens (i. e. PVF50:PVDF50, PVF70:PVDF30, PVF90:PVDF10 wt%) in the two load regions are shown

Samples	n (Slope in low regions)	n (Slope in high regions)
Pure PVF	2.98	2.39
PVF50:PVDF50 wt%	3.55	2.83
PVF70:PVDF30 wt%	3.24	2.54
PVF90:PVDF10 wt%	3.41	2.76

Table 4. Mechanical properties of electrically stressed pure PVF & varying PVDF with different weight percentage in PVF

Sample designation of polyblend specimens	Tensile strength [MPa]	Tensile modulus [GPa]	Elongation [%]
Pure PVF	70.00	14.00	42.00
PVF90:PVDF10 wt%	71.95	15.70	52.20
PVF70:PVDF30 wt%	74.20	16.90	53.00
PVF50:PVDF50 wt%	79.45	19.20	53.90

5. Conclusions

When both the polymers are blended in equal weight proportion (50:50) microhardness was found to be maximum with improved mechanical properties. The microhardness study on virgin and electrically aged thin film of pure PVF and isomorphic polyblend specimens of PVF and PVDF helps to understand the modification in properties due to inter and intra molecular interactions. The electrically stressed specimens exhibit higher level of microhardness as compare to virgin specimens.

References

[1] Peter A. P., Langford H. D.: Advance materials research. National Academy Press, Washington DC (1987).

[2] Calleja F. J. B., Sanditov D. S., Privalko V. P.: Review: The microhardness of non-crystalline materials. Journal of Material Science, **37**, 4507–4516 (2002).

[3] Calleja F. J. B.: Microhardness studies of chain-extended PE: I. Correlation to microhardness. Journal of Polymer Science Part B: Polymer Physics, **37**, 3151–3158 (1999).

[4] Calleja F. J. B., Cenha A. M.: Structure-microhardness correlation of polymers and blends. in 'Structure development during polymer processing' (ed.: Fakirov S.) NATO Science Series Klumer Academic Publisher, Dordrecht, Vol 370E, 145–162 (2000).

[5] Pandey S., Bajpai R., Datt S. C.: A microhardness test to study plasticization in environmentally affected polypropylene. Polymer Testing, **10**, 111–116 (1991).

[6] Bajpai R., Paliwal P., Datt S. C.: Poly (ethylene oxide)/poly (methalcrylate) blends: crystallization, hardening and microhardness behaviour. Journal of Polymeric Materials, **15**, 329–334 (1998).

[7] Calleja F. J. B., Rueda D. R., Boyanoya M., Fakirov S.: On the relationship between microhardness and crystal perfection of chain extended polyethylene. Journal of Macromolecular Science, Part B: Physics, **42**, 1293–1299 (2003).

[8] Bajpai R., Mishra V., Datt S. C.: Microhardness measurements of poly(methyl methacrylate) and poly(vinylidene fluoride) polyblends. Polymer Testing, **11**, 387–391 (1992).

[9] Zamfirova G., Lorenzo V., Benavente R., Perena J. M.: On the relationship between modulus of elasticity and microhardness. Journal of Applied Polymer Science, **88**, 1974–1798 (2003).

[10] Gupta A. K., Bajpai R., Keller J. M.: Morphological, crystallization and plasticization studies on isomorphic blends of poly (vinyl fluoride) (PVF) and Poly (vinylidene difluoride) (PVDF): using microhardness, XRD and SEM techniques. Journal of Material Science, **41**, 5857–5861 (2006).

[11] Jonscher A. K.: Dielectric relaxation in solids. Chelsea Dielectric Press, London (1983).

[12] Bottcher C. J. F., Bordwijk P.: Theory of electric polarization. Elsevier, Amsterdam, (1978).

[13] Strepikhey A., Derevitskaya V., Slonimsky G.: A first course in polymer chemistry. Mir Publishers, Moscow (1971).

eXPRESS Polymer Letters Vol.1, No.9 (2007) 622–628
Available online at www.expresspolymlett.com
DOI: 10.3144/expresspolymlett.2007.85

Evaluation of mechanical properties of unsaturated polyester-guar gum/hydroxypropyl guar gum composites

M. A. Shenoy[*], *D. J. D'Melo*

Polymer Engineering and Technology Division, University Institute of Chemical Technology, Nathalal Parikh Marg, Matunga (East), Mumbai, India

Received 2 June 2007; accepted in revised form 25 July 2007

Abstract. Guar gum is a natural polysaccharide that has been explored for various applications. However, there is a limited number of studies in which guar gum has been used as a filler in a polymer. The effect of guar gum and its hydroxypropyl derivatives in unsaturated polyester composites were investigated with respect to their mechanical and chemical properties. The effect of hydroxypropylation and the degree of hydroxypropylation on the properties of resultant composites were also studied. It was observed that the inclusion of guar gum and its derivatives resulted in composites with increased solvent resistance and mechanical properties. An increase in the degree of substitution resulted in increased polymer-filler interaction reflected by a positive effect on the mechanical properties of the composites. These results open an avenue for the use of polysaccharides and their derivatives as eco-friendly fillers as a replacement of mineral fillers.

Keywords: *polymer composites, mechanical properties, biodegradable polymers, thermosetting resins, material testing*

1. Introduction

Guar gum is a naturally occurring polysaccharide extracted from the endosperm of *Cyamopsis tetragonalobus* and structurally is a galactomannan with a galactose to mannose ratio of approximately 1:2 [1]. There has been some discussion regarding the distribution of the galactose on the mannose backbone, investigations have indicated that the distribution is not uniform but occurs in blocks with galactose rich and deficient regions [2, 3]. These galactose deficient regions are not soluble in water while the galactose rich portions are extremely soluble, resulting in the polymer forming a colloidal solution in water. In spite of this, guar gum and its derivatives are extremely water soluble, hydrophilic polymers, the solutions of which are highly viscous in nature. This property has allowed these polymers and their derivatives to be commercialized in fields such as textiles [4, 5], foods [6], cosmetics [7], pharmaceuticals [8] and oil recovery and drilling [9, 10].

Unsaturated polyester resins are widely used commercial thermosetting resin which are used neat [11], with fillers [12] and reinforced using fibres [13]. Apart from the addition of a separate phase in the polymer matrix, the unsaturated resins have been modified by the use of various reactive diluents [14], reactants [15] and by tailoring the polymer backbone to suit requirements of various applications [16].

The use of guar gum or its derivatives in polymers matrices as fillers has not been investigated in depth. The use of other naturally occurring, renewable polysaccharides as fillers has been focused on starches [17], lignin [18], wood flour [19] and similar materials in mainly thermoplastic polymers. The few studies where guar gum or its derivatives have been used as fillers include the use of guar gum in a polyurethane-polyacrylonitrile interpene-

[*]Corresponding author, e-mail: mas@udct.org
© BME-PT and GTE

trating network [20] and the incorporation of benzoylated guar gums in a quaternised polysulphone polymer matrix [21]. This study attempts to fill in the lacunae in the information available on the use of guar gum and its derivatives as fillers in an unsaturated polyester matrix.

In this investigation, guar gum and hydroxypropyl guar gums were used as fillers in a conventional unsaturated polyester matrix. The mechanical properties were studied with respect to concentration of fillers added as well as the effect of hydroxy-propylation of the derivatives. Guar gum is obtained from natural sources and is hence a renewable resource, biodegradable and non-toxic. The chemical modification of guar gum, in this case hydroxyl-propylation, is not restricted to the surface of the filler, as in the case treatment of mineral fillers, but occurs throughout the polymer chain and the polysaccharide particle. Thus, the effect of the reaction with guar gum will not only affect the polymer-filler interaction but also change the nature of the filler. We expect any improvement of properties to be solely based on increased physical interaction between filler and polymer and not due to any chemical reaction between the two as is possible in the case of vinyl functionalisation. This paper attempts to investigate the feasibility of using guar gum and hydroxypropyl guar gum as a filler in unsaturated polyester composites, as well as the effect of increasing hydrophobic character of the inherently hydrophilic filler on the properties of the composite.

2. Experimental

2.1. Materials

The unsaturated polyester resin, cobalt octoate (accelerator) and methyl ethyl ketone peroxide (initiator) was obtained from M/s Mechamco Ltd. India. Guar gum (GG) and hydroxypropyl guar gum with a molar substitution of 0.4 (HPG4) and 0.8 (HPG8) was supplied by M/s Lucid Colloids Ltd., India. The properties of guar gum and derivatised guar gum are listed in Table 1 and have been obtained from the datasheet provided by M/s Lucid Colloids Ltd., India.

Table 1. Properties of guar gum and hydroxypropyl guar gum

	GG	HPG4	HPG8
Viscosity (1% solution)	1800 cps	1400 cps	1200 cps
% moisture	5–6	6–7	5–6
Ash content (wt %)	0.8–1.0	1.1–1.3	0.9–1.1
Free propanol (wt %)	–	<0.1%	<0.1%

The shape of the guar gum and hydroxypropyl guar gum particles was estimated using an optical microscope, Olympus BX41. The rheology of the unsaturated polyester-guar gum compositions were studied on a RT10 Rheoviscometer using a C35/2° cone and plate assembly. The readings were measures under constant stress.

2.2. Preparation of composites

The fillers were uniformly dispersed in the unsaturated polyester resin along with the accelerator (0.5% w/w), following which the free radical initiator was added (2% w/w) and thoroughly mixed. The filler was added on weight basis, on parts per hundred grams of resin (phr), i. e. 2.5 phr would refer to 2.5 grams of filler per 100 grams of unsaturated polyester resin. The composition was then deaerated to remove any entrapped air and poured in a metal mold maintained at 30°C. The cure cycle was 30°C/12 hours and 100°C/2 hours. The composites had a thickness of 3 mm±1%.

The composites were machine cut into the respective shapes for testing and the edges were uniformly ground to remove imperfections which could lead to errors in the test results. Prior to testing the samples were allowed to stabilize at 50% humidity and at 30°C for 7 days.

2.3. Testing of composites

The composites were tested for their tensile, flexural and impact properties. The tensile strength and percentage elongation (Specimen Type IV^B) and flexural strength (specimen dimensions 60×25×3 mm) were determined according to ASTM D638 and ASTM D790 respectively on a Universal Tensile Testing Machine, Lloyd LR 50K, UK with a crosshead speed of 6 mm per minute for tensile and 8 mm per minute for the three point bending test. Charpy impact, on notched specimens of dimensions (80×10×3 mm with a 1 mm notch), was carried out on an Avery Denison Impact tester using 2.7 J striker with a striking velocity of 3.46 m/s in accordance with ASTM D256. Tests were carried out on five samples and the averages have been reported as the test results.

Water and toluene absorption were studied using three 1×1×0.3 cm chips and suspending them separately for a period of 7 days in 100 ml solvent at 30°C. After the required amount of time the samples were removed and gently dried using a filter paper to remove water or solvent adhering to its surface. The increase in weight was then estimated and the percentage increase in water or solvent was reported.

3. Results and discussion

Guar gum is a very hydrophilic polymer and while most resins are hydrophobic in nature, the use of guar gum as a filler may result in a composite with increased interfacial tension. The effect of hydroxypropylation on the gaur gum would be to increase the hydrophobic nature of the polymer, while leaving the number of hydroxyl groups per pyranose unit in the polysaccharide constant, leading to increased polymer-filler interaction. This increase in the polymer-filler interaction should be reflected by an increase in the tensile and flexural strength [22] as well in other mechanical and chemical properties. The examination of the particle shape of guar gum using optical microscopy showed that the guar gum particles were highly irregular in shape as seen from Figure 1. Observation of HPG4 and HPG8 showed similar particle shapes and sizes.

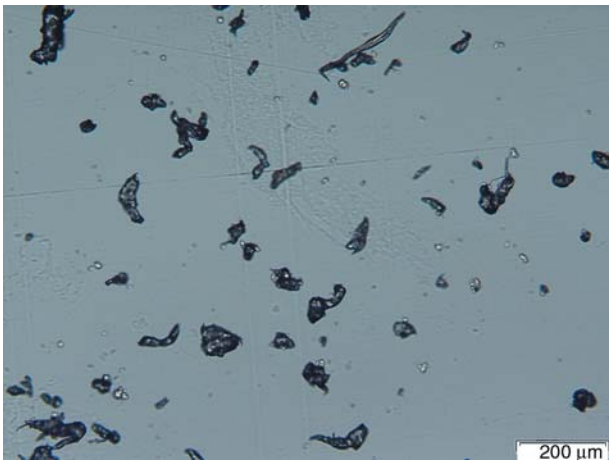

Figure 1. Image of guar gum (GG)

3.1. Rheology

The study of the rheology of the composition was carried out to ascertain the degree of interaction between the uncured resin and the filler. The concentration of filler taken was 2.5 phr. From Figure 2 it becomes apparent that the addition of filler

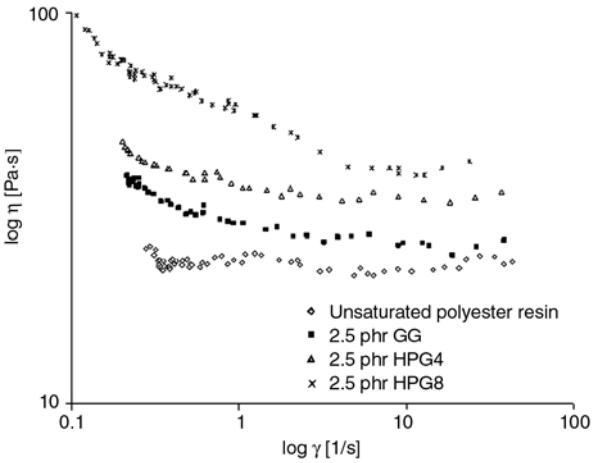

Figure 2. Variation of viscosity with shear rate

in unsaturated polyester resin results in compositions with increased viscosity, which is to be expected and has been reported in a number of studies [23]. Further, the addition of the various fillers results in compositions with varying viscosities. The viscosity of the composition increases with the degree of hydroxypropylation. Thus, HPG8 results in the most viscous composition followed by HPG4 and GG at the same concentrations of filler. The viscosity of the formulations was studied at the same concentration of filler and thus the observed increase in viscosity with degree of hydroxypropylation was due to increased interaction between the filler and polymer. An increase in the interaction between the filler and the polymer would result in an increased resistance to flow on application of shear leading to the increased viscosity. The increase in interaction can be attributed to the increased hydrophobic nature of the filler with increased hydroxypropyl content. The increase in viscosity of a polymer-filler composition through the increase in their interaction keeping other factors such as filler concentration, size, shape, etc. constant has been previously reported [24]. Although the polyester is in its uncross-linked form we assume a similar trend in the interaction between the filler and the cross-linked polyester. Further, evidence of the increased interaction will be obtained from the mechanical properties of the resultant composites.

3.2. Solvent absorption

Unsaturated polyester composites are known for their poor resistance to aromatic solvents, due to the use of styrene as a reactive diluent, which is

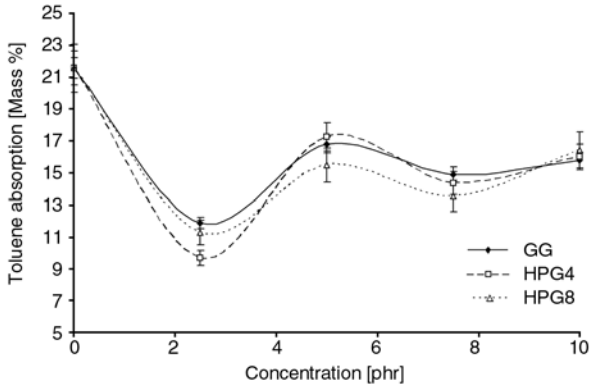

Figure 3. Toluene absorption of unsaturated polyester composites

why toluene was chosen to observe the effect of filler addition on the solvent resistance of the composites. From Figure 3 it becomes apparent that the toluene absorption reduced with the addition of filler. The filler, i. e. GG and HPGs are hydrophilic in nature and their affinity with toluene is quite low. We see that the toluene absorption of the composites do not show significant difference in the absorption behaviour with use of HPG as compared to GG. At a 2.5 phr concentration the composites showed reduced toluene absorption which then increased on further addition and reached a steady state above 5 phr.

Considering the hydrophilic nature of the fillers the water absorption of the resultant composites becomes very important. From Figure 4 we can see that the addition of 2.5 phr GG and HPG8 resulted in composites with reduced water absorption, which then increased with filler concentration. On the other hand the addition of HPG4 based unsaturated polyester composites did not show any significant increase in water absorption. The overall observations show that above the concentration of about 4 phr the addition of GG as a filler resulted in composites with the greatest water absorption as compared to HPGs. This can be explained by the reduction in the hydrophilic character of the substituted guar gums and also by the increased polymer-filler interaction restricting permeability of water in the composite.

3.3. Tensile properties

In general it was observed that there was an increase in the tensile strength of the composites containing fillers as is graphically depicted in Figure 5. Guar gum based composites also showed an increase in the tensile strength, indicating that there was some degree of interaction between the filler and the polymer matrix. The composites based on HPG4 and HPG8 showed increased tensile strength compared to that of GG based unsaturated polyester composites. HPG8 based composites showed the highest tensile strength followed by HPG4 and GG based composites. This can be explained by the increased polymer-filler interaction with increased hydrophobic nature of the filler. The optimum concentration of filler was found to be at 2.5 phr and was found to be the same for GG and HPGs. The decrease in the tensile strength at filler concentrations above 2.5 phr could be due to agglomerate formation which would result in the formation of stress centres in the composite contributing to initiation of catastrophic failure of the composites on the application of stress.

The percentage elongation of the composites showed an initial decrease where they showed an increase in tensile strength i.e. at 2.5 phr followed by a maxima observed at 5 phr as is evident from Figure 6. Above 5 phr the percentage elongation decreased but was still greater than that observed for unfilled unsaturated polyester in the case of

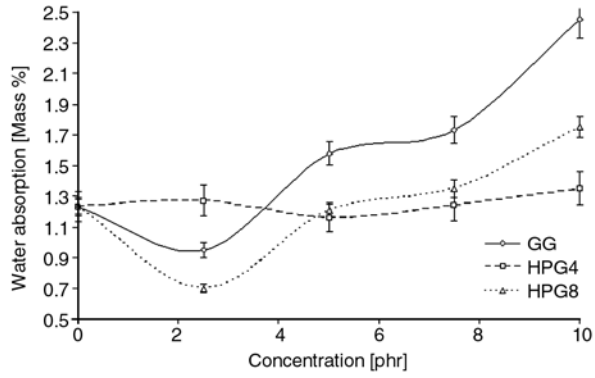

Figure 4. Variation in water absorption

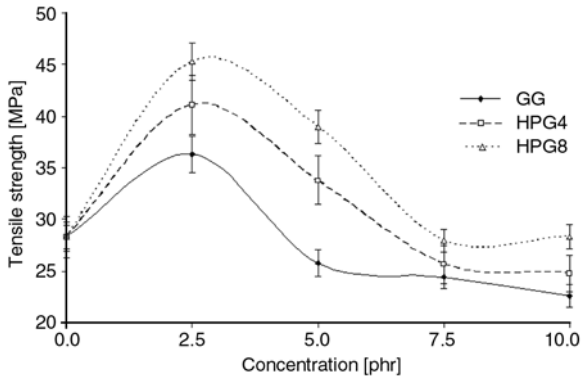

Figure 5. Variation of tensile strength with addition of filler

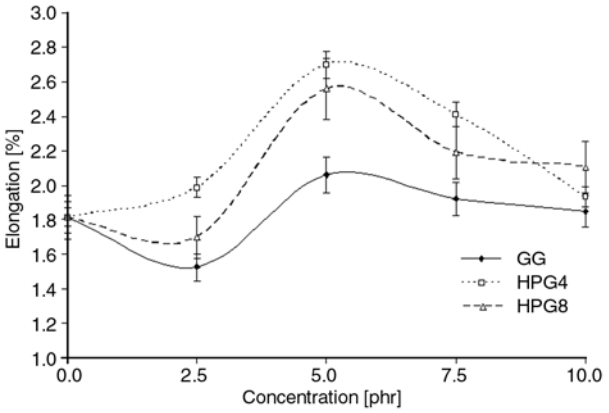

Figure 6. Variation in % elongation

HPG based composites. GG based composites showed percentage elongation almost equivalent to that of the pure unsaturated polyester. As in the case of the tensile strength the composites based on HPG8 showed the greatest increase in the percentage elongation. The initial decrease in the percentage elongation at 2.5 phr could be due to the reinforcing effect of the filler, which resulted in an increase in the tensile strength. At 5 phr and beyond agglomerate formation, which resulted in a decrease in the tensile strength, could be the cause of the anomalous increase in the elongation. The elongation of the composite can also increase as a result of decreasing cross-linking density, however, if that were the case then there should have been a corresponding increase in the toluene absorption by the composites, which was not observed. Hence, a decrease in the cross-linking density as the cause of the increased elongation can be ruled out.

3.4. Flexural properties

The flexural strength of the composites can be seen in Figure 7 where HPGs show an increased flexural strength, with HPG8 again resulting in the composites with greatest flexural strength. HPG8 based composites show a maxima at 5 phr while those based on HPG4 show an almost steady value till 7.5 phr after which it decreases. Guar gum however, results in composites with a continuous decrease in the flexural strength with GG concentration. This trend can again be explained on the basis of increased filler-polymer interaction in the case of HPGs as compared to GG, resulting in composites with reduced internal stresses and reinforcing action of the HPG particles. The decrease in the flexural strength of the composites can be explained on the basis of agglomerate formation at higher concentrations of the filler, which was also reflected in the tensile behaviour of the composites.

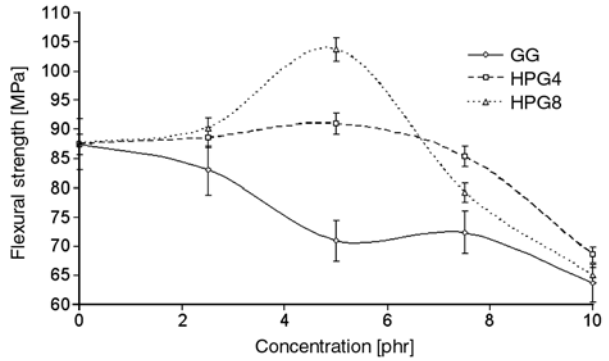

Figure 7. Variation in flexural strength

3.5. Impact properties

Figure 8 shows the impact strength of the composites based on GG and HPG. The impact strength of the HPG based composites showed a maximum at 5 phr with HPG8 surpassing HPG4 based composites. GG resulted in composites with slightly reduced impact strength which remained almost unaffected by the increase in filler concentration. The increased impact strength of the HPG based composites can be explained by increased polymer-filler interaction as compared to GG based composites. The increased impact resistance can be explained by the formation of a tortuous fracture path which retards crack propagation. Further, increased polymer-filler interaction will decrease interfacial tension and reduce chances of crack initiation at the interface. With increasing interfacial interaction there could also be more efficient energy transfer to the filler particles which would help dissipate this energy through breakage of temporary bonds such as hydrogen bonds which are abundantly present in the polymer. All these factors

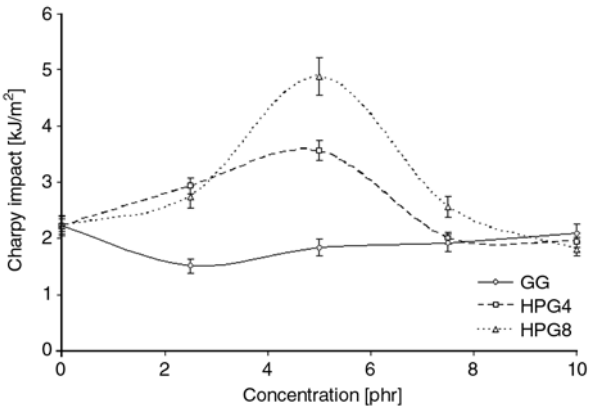

Figure 8. Variation in impact strength

will contribute towards the increased impact resistance of the HPG based unsaturated polyester composites. At higher concentrations due to agglomerate formation, as indicated by the other mechanical properties, the impact resistance of the composites will decrease, which explains the decrease observed after 5 phr in the impact resistance.

From the results we see that guar gum and its derivatives behave as reinforcing fillers. The hydroxypropylation of the guar gum results in increased polymer-filler interaction, both in the uncured resin as well as in the composite as indicated by the increased viscosity of the uncured formulation and improved mechanical and chemical properties of the composites. The improved performance of the hydroxypropyl guar gum fillers has been attributed to an increase in physical interaction. The use of acrylated guar gum derivatives is currently under investigation and preliminary results indicate that the use of acrylated guar gum forms an interpenetrating network. From these results other polysaccharide derivatives, such as ethers, esters and graft copolymers, of commonly available polysaccharides can also be investigated for their use as fillers. These composites can be used in applications where increased mechanical and impact properties are required by the use of an eco-friendly filler.

4. Conclusions

Guar gum and its hydroxypropyl derivatives were found to behave as reinforcing fillers. The increase in the degree of hydroxypropylation of guar gum increased the interaction between the polymer and polysaccharide. The toluene absorption of the composites were observed to decrease with filler addition, on the other hand the water absorption increased at filler concentrations greater than 5 phr. Composites prepared using guar gum and hydroxypropyl guar gum as fillers showed increased mechanical properties. The composites also showed increased elongation at 5 phr. On comparing the efficiency of the fillers it was observed that an increase in the degree of hydroxypropylation resulted in composites with increased mechanical properties. This opens an avenue for the use of similar polysaccharides and their derivatives as fillers in polymer composites with thermoset resins. The advantage of using such materials lies in their inherent bio-degradability, ease of ability from renewable sources and non-toxicity.

References

[1] Wientjes R. H. W., Duits M. H. G., Jongschaap R. J. J., Mellema J.: Linear rheology of guar gum solutions. Macromolecules, **33**, 9594–9605 (2000).

[2] Painter T. J., Gonzalez J. J., Hemmer P. C.: The distribution of d-galactosyl groups in guaran and locust-bean gum: new evidence from periodate oxidation. Carbohydrate Research, **69**, 217–226 (1979).

[3] Grasdalen H., Painter T. J.: N.M.R. Studies of composition and sequence in legume-seed Galactomannans. Carbohydrate Research, **81**, 59–66 (1980).

[4] Sostar S., Schneider R.: A study of fabric stiffness with guar gum in reactive printing. Dyes and Pigments, **41**, 167–175 (1999).

[5] Schneider R., Sostar-Turk S.: Good quality printing with reactive dyes using guar gum and biodegradable additives. Dyes and Pigments, **57**, 7–14 (2003).

[6] Funami T., Kataoka Y., Omoto T., Yasunori G., Asai I., Nishinari K.: Food hydrocolloids control the gelatinization and retrogradation behavior of starch. 2a. Functions of guar gums with different molecular weights on the gelatinization behavior of corn starch. Food Hydrocolloids, **19**, 15–24 (2005).

[7] Maurin V., Beauquey B.: Composition for washing keratin materials, based on a detergent surfactant, a cationic galactomannan gum and an acrylic terpolymer. U. S. Patent 6383993, USA (2002).

[8] Soppimath K. S., Kulkarni A. R., Aminabhavi T. M.: Chemically modified polyacrylamide-g-guar gum-based crosslinked anionic microgels as pH-sensitive drug delivery systems: preparation and characterization. Journal of Controlled Release, **75**, 331–345 (2001).

[9] Moorhouse R., Matthews L. E.: Aqueous based zirconium (IV) crosslinked guar fracturing fluid and a method of making and use therefore. U. S. Patent 6737386, USA (2004).

[10] Mothe C. G., Correia D. Z., de Franca F. P., Riga A. T.: Thermal and rheological study of polysaccharides for enhanced oil recovery. Journal of Thermal Analysis and Calorimetry, **85**, 31–36 (2006).

[11] Ayman M. A., Abdel-Raouf M. E., Elsaeed S. M., Abdel-Azim A. A.: Curable resins based on recycled poly(ethylene terephthalate) for coating applications. Progress in Organic Coatings, **55**, 50–59 (2006).

[12] Lu W., Lin H., Wu D., Chen G.: Unsaturated polyester resin/graphite nanosheet conducting composites with a low percolation threshold. Polymer, **47**, 4440–4444 (2006).

[13] Burgueno R., Quagliata M. J., Mohanty A. K., Mehta G., Drzal L. T., Misra M.: Load-bearing natural fiber composite cellular beams and panels. Composites Part A- Applied Science and Manufacturing, **35**, 645–656 (2004).

[14] Pietschmann N., Stengel K., Hoesselbarth B.: Investigations into vinylogic addition reactions of modified polyester resins. Progress in Organic Coatings, **36**, 64–69 (1999).

[15] Martuscelli E., Musto P., Ragosta G., Scarinizi G.: A polymer network of unsaturated polyester and bismaleimide resins: 1. Kinetics, mechanism and molecular structure. Polymer, **37**, 4025–4032 (1996).

[16] Banu P., Radhakrishnan G.: Unsaturated poly(esterimide)s from hydroxy-terminated polybutadiene, dianhydride and diisocyanate. European Polymer Journal, **40**, 1887–1894 (2004).

[17] Vargha V., Truter P.: Biodegradable polymers by reactive blending trans-esterification of thermoplastic starch with poly(vinyl acetate) and poly(vinyl acetate-co-butyl acrylate). European Polymer Journal, **41**, 715–726 (2005).

[18] Yang H. S., Wolcott M. P., Kim H. S., Kim H. J.: Thermal properties of lignocellulosic filler-thermoplastic polymer bio-composites. Journal of Thermal Analysis and Calorimetry, **82**, 157–160 (2005).

[19] Caraschi J. C., Leao A. L.: Woodflour as reinforcement of polypropylene. Material Research, **5**, 405–409 (2002).

[20] Kumar H., Siddaramaiaha Somashekar R., Ranganathaiah C.: Biodegradation and characterization of guar gum filled polyurethane/polyacrylonitrile semi-interpenetrating polymer network. in 'MACRO 2006 – 9th National conference of polymers for advanced technologies' NCL Pune, India, 1–2 Dec (2006).

[21] Huang Y., Xiao C.: Miscibility and mechanical properties of quaternized polysulfone/benzoyl guar gum blends. Polymer, **48**, 371–381 (2007).

[22] Sen S., Nugay N.: Tuning of final performances of unsaturated polyester composites with inorganic microsphere/platelet hybrid reinforcers. European Polymer Journal, **37**, 2047–2053 (2001).

[23] Joo Y. L., Lee Y. D., Kwack T. H., Min T. I.: Rheology and processing of polycarbonate/carbonate/carbon black composites. in 'Antec '96. Conference Proceedings', Indianapolis, USA, Vol. I., 64–68 (1996).

[24] Clarke J., Freakley P. K.: Reduction in viscosity of an SBR compound caused by mastication and disagglomeration during mixing. Rubber Chemistry and Technology, **67**, 700–715 (1994).

eXPRESS Polymer Letters Vol.1, No.9 (2007) 629–639
Available online at www.expresspolymlett.com
DOI: 10.3144/expresspolymlett.2007.86

Synthesis and properties of epoxy-phenolic clay nanocomposites

M. L. Auad[1], S. R. Nutt[2], V. Pettarin[3], P. M. Frontini[3]*

[1]Auburn University, Polymer and Fiber Engineering Department, 103 Textile Building Auburn, AL 36849, U.S.
[2]University of Southern California, Materials Science Department, Gill Foundation Composites Center 3651 Watt Way, VHE-602 Los Angeles, CA 90089-0241, U.S.
[3]Instituto de Ciencia y Tecnología de Materiales (INTEMA), CONICET Universidad Nacional de Mar del Plata, Juan B. Justo 4302, B7608FDQ Mar del Plata, Argentina

Received 25 May 2007; accepted in revised form 7 August 2007

Abstract. An epoxy-phenolic resin suitable for use as a composite matrix was reinforced with modified nanoclay (montmorillonite type). Characterization by x-ray diffraction and transmission electron microscopy (TEM) demonstrated that intercalated nanocomposites were formed with an inter-gallery distance of approximately 10 nm. The influence of nanoparticles on tensile strength and modulus, fracture toughness, and impact toughness was measured and compared with the unreinforced polymer. The results revealed that the maximum enhancement in stiffness and toughness was achieved with 2.5 wt% filler content. The enhancement in toughness behavior was attributed to the activation of multiple energy-dissipating damage mechanisms in the nanocomposites.

Keywords: *nanocomposites, epoxy-phenolic, layered silicates*

1. Introduction

Polymer/clay nanocomposites offer the possibility of improved properties which cannot be matched by micron-sized filler particles, such as conventional talc and glass fillers [1–5]. Nanocomposites reportedly show enhanced tensile and thermal properties [1–8], heat distortion temperature [1–5], resistance to flammability [9, 10], and reduced permeability to small molecules [4, 11, 12] and solvent uptake [13]. These enhancements are partly attributable to the extremely large particle surface area available for interaction with the polymeric matrix, coupled with a high aspect ratio (between 30 and 2000) [14]. The property improvements resulting from the formation of a nanocomposite occur at relatively low concentrations of clay (generally 2–5 wt%) compared to conventional filled polymer composites, which often contain 20–30 wt% of filler. In addition to enhanced performance, clay nanocomposites are easily extruded or molded to near-net shape, simplifying the manufacturing process.

For the reasons noted above, polymer nanocomposites are likely to find a wide range of new applications in reinforced lightweight structural components, non-linear optics, battery cathodes, nanowires, sensors and other systems. Transportation-oriented applications that require weight savings are also likely, including airplane interiors, fuel tanks, and structural components of air and land vehicles [15].

The two major steps involved in dispersing clay nanoparticles in polymers are intercalation and exfoliation [6]. In the intercalation step, the spacing between individual clay layers increases as polymer chains or monomer molecules diffuse into the

*Corresponding author, e-mail: auad@auburn.edu
© BME-PT and GTE

clay galleries. Intercalation can be facilitated by specific treatments of clay particles with organic modifiers. In exfoliation, the individual clay particles separate from the intercalated tactoids and are dispersed in the matrix polymer, forming a monolithic structure [16].

Up to now, extensive research on general polymer layered silicate nancomposites has been carried out [7, 11, 17, 18]. Epoxy/clay has been one of the most studied systems, where merely intercalated or exfoliated structures were obtained [6, 8, 10]. On the other hand exfoliation has been reported for several polymer matrixes, such as polyimide [4, 7], polyaniline [19], nylon [20] and phenolic [21, 22]. However, there is no reported research on Epoxy-Phenolic/clay system. Compared with the epoxy or phenolic systems, epoxy-phenolic based nanocomposites offer some intriguing benefits, including both flame-resistance and low cost. In addition, phenolic-epoxy networks can exhibit acceptable mechanical properties [23, 24]. Because of the void-free nature of these materials combined with tailored crosslink densities, these thermosets can exhibit toughness comparable to or exceeding untoughened aerospace epoxies while maintaining flame retardant properties approaching those of pure phenolic polymers [23, 24]. For these reasons, E-P resins are also attractive for use in airplane interiors. Adding nano-fillers, such as nanoclay, can greatly improve the mechanical and thermal properties of these systems.

In this work, we report the preparation methods and characterization of epoxy-phenolic clay nanocomposites with varying percentages of nanoclay filler. The intent is to establish the structure-property relations in this system. The nanostructure is verified by x-ray diffraction (XRD) and by transmission electron microscopy (TEM). Mechanical properties and fracture behavior are measured and related to observed microstructures.

2. Experimental

2.1. Materials and sample preparation

A montmorillonite type nanoclay modified with methyl tallow bis-2-hydroxyethyl quaternary ammonium chloride (Southern Clay Products, Cloisite 30B) was selected for this study. Epoxy-phenolic (E-P) networks were synthesized by reacting a novolac type phenolic resin (Georgia Pacific, laboratory grade reagent) and an epoxy resin, diglycidyl ether of bisphenol A (Epon 828, equivalent weight 187 g/eq.), using 0.3 wt% of triphenylphosphine as catalyst (Fluka A. G., analytical reagent). The amount of catalyst added is reported based on the weight of epoxy. The curing E-P reaction proceeds via nucleophilic addition of the phenolic hydroxyl onto the epoxy group [25–27].

As-received clay was dried in a vacuum oven for 24 hours at 100°C, then mixed with different epoxy-to-phenolic ratios as shown in Table 1. To prepare the samples, the epoxy was first dried at 80°C under vacuum for 24 hours. The resulting mixture was blended using an orbital mixer (Keyence) for 30 minutes. After this step, the samples were sonicated at 60°C for 1 hour and placed in an oven for 12 hours at 60°C. Next, the mixtures were blended with the novolac at 140°C for 30 minutes. Finally, the catalyst was added and the mixtures were placed in closed molds. The curing reaction was carried out in a conventional oven at 180°C for 1 hour and at 200°C for 30 additional minutes.

Table 1 provides details of the weights and equivalent weight percentages of epoxy-to-novolac used for this work. Also given in Table 1 are the identification codes assigned to the fabricated materials. Different amounts of clay (0, 1, 2.5, 5 and 10 wt%) were used for sample preparation.

Table 1. E-P formulation

Formulation	E-P [eq./eq.]	E-P [wt %/wt %]
E-P(67/33)	1/1	67/33
E-P(50/50)	1/2	50/50
E-P(35/65)	1/4	35/65

2.2. Characterization

X-ray diffraction patterns were acquired using Cu Kα radiation in the 2θ range 3°–14°, with a scanning rate of 5°/min (Rigaku RV20 diffractometer). Transmission electron microscopy (TEM) was performed at an accelerating voltage of 100 kV (JEOL 100CXII) on ~100 nm thick sections, microtomed from samples containing 2.5 and 5 wt% clay. Micrographs of the fracture surfaces of the different materials were recorded using a scanning electron microscope operated at 15 kV (Cambridge 360 SEM). Fractured specimens were coated with gold to impart electrical conductivity.

2.2.1. Thermal analysis

The glass transition of the samples was determined as the temperature corresponding to the maximum in the tanδ curve. Thermo-mechanical response of the cured resins was determined using a dynamical mechanical analyzer (TA Instruments, Newark, Delaware). Beam samples were cut to 3 mm × 5.5 mm × 60 mm and clamped in the frame using dual cantilever mode. For analysis, samples were heated from 25 to 300°C at a rate of 10°C/min, and cyclic load was applied at a frequency of 10 Hz.

2.2.2. Mechanical properties

Mechanical tests were carried out at room temperature using a universal testing machine (Instron model 4467). The flexural tangent elastic modulus and strength were determined in accordance with standard methods (ASTM D790M) using a loading rate of 1.7 mm/min. The compressive yield behavior was determined using cylindrical specimens, with an aspect ratio of 3. Specimens were machined from samples molded in glass tubes. Care was taken to obtain smooth and parallel faces. Uniaxial compression tests were performed at a loading rate of 0.5 mm/min following ASTM 695.

Fracture toughness was determined using a single edge notched (SEN) type specimen (6.4 mm × 12.7 mm × 60 mm) and applying conventional linear elastic fracture mechanics to determine the critical stress intensity factor in plane strain, K_{1C}. Tests were performed according to ASTM D5045-93. After making a notch at the center of the sample with a reciprocating saw, a sharp crack of length a was initiated by tapping a fresh razor blade into the notch tip at room temperature. Samples were loaded in a 3-point bending fixture at a crosshead speed of 10 mm/min. The mean value of at least eight samples was reported. From load-displacement plots and known crack lengths, the stress intensity factor, K_{1C}, was computed at a maximum load (P). Equation (1) was used, where $f(a/W)$ is a dimensionless function of the ratio a/W (Equation (2)) is a, given by ASTM D5045, W is the specimen height, and B is the thickness.

$$K_{1C} = \frac{f(a/W)P}{B \cdot W^{1/2}} \tag{1}$$

where

$$f(a/W) = 6\frac{a^{1/2}}{W}\frac{\left[1.99 - \frac{a}{W}\left(1-\frac{a}{W}\right)\left(2.15 - 3.93\frac{a}{W} + 2.7\frac{a^2}{W}\right)\right]}{\left(1+2\frac{a}{W}\right)\left(1-\frac{a}{W}\right)^{3/2}} \tag{2}$$

In order to analyze the damage zone around the crack tip, the double-notch four-point-bend (DN-4PB) technique was used (Figure 1). Two edge cracks of approximately equal length were generated in the specimen (64 mm × 12.7 mm × 125 mm). The specimen was then loaded in a four-point bending fixture at a crosshead speed of 10 mm/min, locating the two pre-cracks within the minor span on the tensile side. Owing to stress intensification at the crack tips, a plastic zone formed independently at each crack tip upon loading (the pre-crack spacing exceeded the size of the plastic zone). Because the pre-cracks were not identical, one pre-crack become critical and propagated in an unstable manner, thus unloading the other crack that was immediately arrested.

Transmitted optical microscopy, TOM, was employed to examine the damage zone around the surviving crack tip. Thin sections were obtained using conventional grinding-polishing techniques [28, 29]. First, a block was cut by sectioning normal to the fracture surface but parallel to the direction of crack propagation. The block was encapsulated in epoxy and cured at room temperature. Samples were finely ground and polished. The

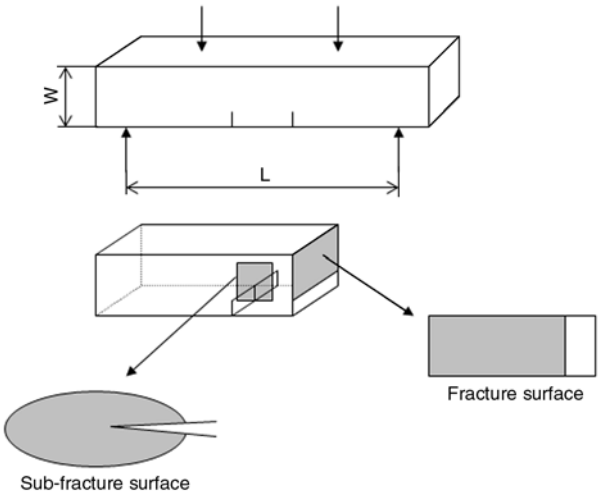

Figure 1. Scheme of the double-notch four-point-bend (DN-4PB) technique

polished surface was mounted onto a clean glass slide using an optically clear epoxy that was allowed to cure overnight at room temperature. The sample was again ground and polished until the plane of interest was finally reached. The thickness of the final material ranged from 150 to 350 μm. Optical micrographs were recorded using a transmission microscope, with and without crossed-polarizers.

Charpy-type impact tests were performed in an instrumented falling weight impact tester (Fractovis, Ceast). Rectangular, V-notched specimens with nominal dimensions $S \times W \times B$ equal to 80 × 10 × 6 mm were struck by an impactor mass of 3.6 kg at an impact speed of 1 m/s, corresponding to an impact energy of 1.8 J at room temperature. Impact strength was calculated as the ratio between energy consumed (area of the load *vs*. deformation curve) and resistant area of the sample (ASTM D256). The distance between supports was set to 70 mm. The average of results obtained from 10 samples per material was reported as the impact strength.

3. Results and discussion

3.1. Morphology of E-P/clay nanocomposites

XRD was used to monitor the expansion behavior of the silicate layers after curing of the nanocomposites. The x-ray scattering intensities for the organically modified clay (Cloisite 30B) and the E-P nanocomposites containing different amounts of clay are shown in Figure 2. The diffraction pattern for the pure clay shows a peak corresponding to the basal plane spacing of 1.54 nm for the organically modified montmorillonite. After the curing process, none of the samples show this basal plane peak, indicating that exfoliation or intercalation has occurred in the system.

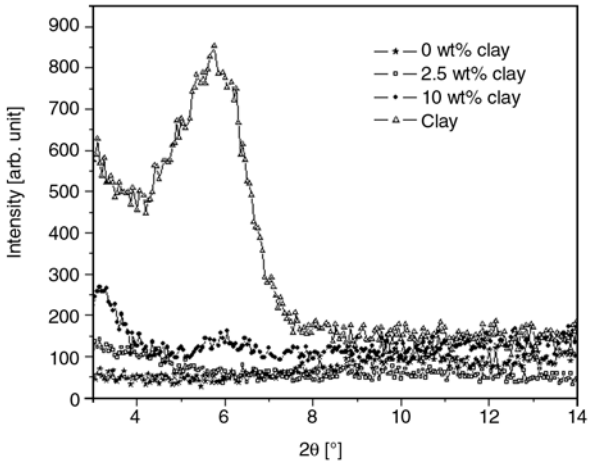

Figure 2. X-ray diffraction pattern for the E-P/clay nanocomposites. Sample: E-P(35/65)

TEM experiments allow the morphological state of the nanocomposite to be delineated more completely. Montmorillonite clay consists of hierarchy structures, of which the individual aluminosilicate sheets (~1 nm thick) may be considered the structural unit. Several sheets stacked face to face with an interlayer charge balancing cation lead to a stack and an agglomeration of these stacks leads to the macroscopically observable micron-sized particles. Therefore, each macroscopic particle of clay is actually comprised of many individual aluminosilicate sheets. Consequently, the formation of a nanocomposite involves the break-up and dispersion of the agglomerated stacks of sheets followed by the swelling of the gallery spacing between the sheets by the polymer and the monomers. Figure 3a and 3b show transmission electron micrographs of the E-P nanocomposite containing 2.5 wt% clay. At low magnifications, some aggregates of clay layers were present in the composites (Figure 3a). However increasing the magnification in an area occupied by an aggregate reveals the individual sheets of clays clearly separated by a layer of E-P polymer as showed in Figure 3b. It is evident that in general, the nanostructures consisted primarily of layered sheets rather than exfoliated single sheets. That is, there are regions where the regular stacking arrangement is maintained with a layer of polymer between the sheets, and also regions where completely delaminated sheers are dispersed individually. The distance between the layers was approximately 10 nm. This long-range ordered structure is typical of thermoset, layered silicate nanocomposites synthesized via *in-situ* polymerization [30].

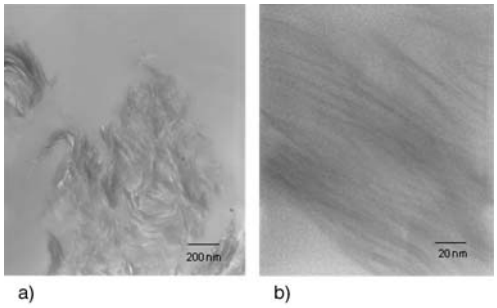

Figure 3. TEM image of E-P/clay nanocomposite containing 2.5 wt% of clay. Sample: E-P(35/65). a) line: 200 nm, b) line: 20 nm

Table 2. Changes in thermal, flexural and compressive behavior of the clay reinforced E-P samples

Matrix	Clay [wt%]	Thermal properties T_g [°C]	Flexural properties		Compression properties Strength [MPa]
			Modulus [MPa]	Strength [MPa]	
E-P (67/33)	0	139.5	3516.1±15.9	121±3.1	144.5±9.2
	1	128.0	–	120±1.2	–
	2.5	127.6	3800.3±57.2	117±2.5	73.6±13.6
	5	126.9	3960.6±36.2	124±2.2	57.6±8.4
	10	132.3	4054.1±105.4	114±1.6	50.4±15.2
E-P (50/50)	0	141.0	3757.3±217.9	135.1±3.4	79.6±8.2
	1	144.8	3549.2±102.3	122.3±1.3	76.2±29.6
	2.5	144.7	–	120.5±2.1	–
	5	143.7	3709.0±164.0	127.9±1.3	76.0±7.1
	10	141.6	4260.4±216.4	119.4±1.8	63.5±4.7
E-P (35/65)	0	122.8	4147.9±297.8	–	82.03±20.4
	1	118.4	4533.4±494.2	–	66.1±13.3
	2.5	116.7	4645.9±114.5	–	52.1±4.6
	5	119.4	–	–	–
	10	116.6	4826.7±162.7	–	30.9±9.2

3.2. Thermal properties

Table 2 shows the changes in T_g of the clay-reinforced E-P samples. Considering the reaction that occurs in the E-P system [26, 27], the addition of epoxy in the E-P formulations increased the glass transition temperature of the networks. The higher crosslinked material is expected to be formed when equimolar amounts of phenolic and epoxy are used (1:1 ratio, E-P(67/33)). However, in this system, the T_g reaches a maximum value for the 50/50 E-P sample (phenol-epoxy ratio 2:1). To explain this maximum, note that for the system under study, the cross-linking density is not the only factor affecting the physical properties of the networks. As the compositions were varied to achieve phenol–epoxy equivalence ratios from 1:1 to 4:1, the epoxy concentration is not sufficient to connect the phenolic chains, leaving a large number of dangling chain ends that could act as plasticizer. Increasing the concentration of phenolic, there is a balance between the dangling chains that increase and the effect of glassy intermolecular forces that increase along this series, due to an increase in hydrogen bonding from the increased numbers of unreacted phenols.

Table 2 also shows the change in the T_g for nanocomposites with various clay loadings. The thermal properties of nanocomposites containing 1:1 and 4:1 phenol-epoxy equivalent ratio exhibit a completely different behavior than the samples with 2:1 phenol-epoxy equivalent ratio. This observation is clear evidence of the effects of cross-linking density and the intermolecular forces due to the unreacted phenol groups, as described previously. However, the general tendency of the T_g is to decrease with increasing additions of nanoclay. Similar variations in T_g have been reported for other nanocomposite systems [30, 31]. For example, Chen *et al.* [31] attributed such variation to the formation of an interphase between the silicate layers. An interphase is defined as the matrix material near the surface of the filler compound, where the matrix properties differ from the properties in the bulk matrix. In this case, the interphase between the nanoclay particles and the matrix may be affected by the cross-linking density, causing or contributing to the observed decrease in the glass transition temperature.

3.3. Mechanical performance

3.3.1. Flexural and compressive properties

Table 2 lists the measured flexural and compressive properties for the E-P/clay composites and unreinforced controls. For the pristine samples, the results show that the flexural modulus increases with decreasing ratio of epoxies to phenols. Tyberg *et al.* [23, 24] attributed this effect to a decrease in the network density, although there is no established relationship between modulus and network density. The addition of the nanoclays substantially increased the flexural modulus of the nanocomposites relative to the neat polymer. For example, 10 wt% of organoclay produced a 20% increase in flexural modulus. The mechanical properties of composites depend on multiple factors, including the aspect

ratio of the filler, the degree of dispersion of the fillers in the matrix, and the adhesion at the filler-matrix interface [32, 33]. In addition, the degree of exfoliation of the layered silicate in the polymer influences the modulus of nanocomposites [34, 35]. Several explanations have been proposed to explain the modulus enhancement observed in polymer layered silicate hybrids. Most explanations focus on the large surface area of the inorganic phase and the corresponding restricted mobility of the polymer chains [34, 36, 37]. In glassy-epoxy systems such as the present system, the stiffness improvement is generally attributed to an increase in the effective particle volume fraction in the nanocomposite [34]. In contrast, a surprising decrease in compressive and flexural strength is observed, despite the addition of a stiff reinforcement [35]. This decrease is attributed to clustering of nanoparticles, as noted from the TEM images (Figure 3a). In most cases, epoxy-based nanocomposites show no improvements in strength [35]. In fact, inhomogeneous microscale dispersions of the layered silicate dramatically lower the strength. This suggests that the strength of brittle matrix nanocomposites is primarily controlled by the dispersion of microscale silicate particles.

3.3.2. Fracture properties

All materials fractured in an unstable manner, however some differences in behaviour were observed among them. Samples with E-P(35/65) and E-P (50/50) exhibited complete brittle fracture as judged from the linearity of the load deflection records (Figure 4) and the features of the fracture surface. Load–time curves dropped to zero instantaneously upon reaching the maximum load. Samples with E-P(67/33) exhibited semi-brittle behaviour and developed limited plasticity ahead of the crack tip. The load increased first linearly and then non-linearly and displayed a drastic drop in coincidence with the sample failure. Features of load-displacement curves were not influenced by the addition of clay. All samples were within the Linear Elastic Fracture Mechanics condition, i. e., $P_{max}/P_{5\%} < 1.1$, and toughness obtained from them represent valid plane strain values satisfying size criteria (Equation (3)):

$$B, a, (W-a) > 2.5\left(\frac{K_{1C}}{\sigma_y}\right)^2 \tag{3}$$

Figure 5 shows the dependence of fracture toughness, (K_{1C}) on clay content for the different E-P nanocomposites. The pure matrix toughness increases with increasing ratios of phenol to epoxy up to a threshold in E-P(50/50). This trend is consistent with expectations of increased toughness with the average molecular weight between crosslinks (increasing ratio of phenol-to-epoxy) up to a threshold, at which point the density of unconnected phenolic chains begins to dominate the properties [23–24]. Note that in the present system, an additional factor affected the physical properties of the networks. As the compositions were varied from epoxy-phenolic equivalent ratios of 1:1 to 1:4, the network densities decreased, but at the same time, the intermolecular forces increased as a result of increased hydrogen bonding from the large num-

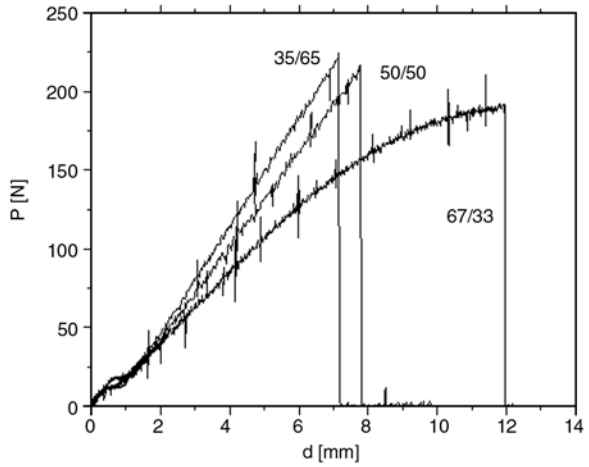

Figure 4. Load deflection curve of pristine samples (P – load and d – deformation)

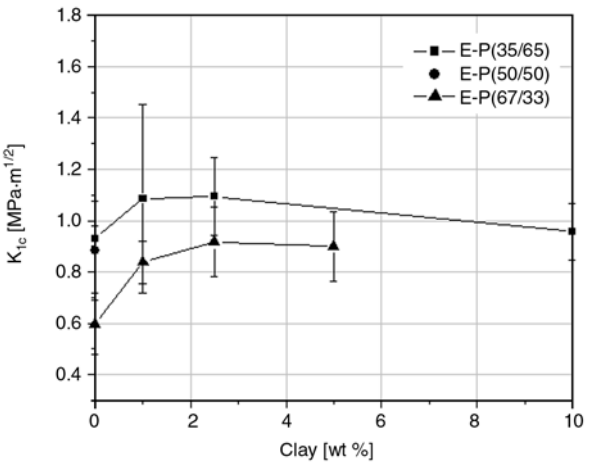

Figure 5. Fracture toughness the different E-P nanocomposites as a function of clay content

ber of unreacted phenols. Both factors contributed to toughness in a complementary fashion.

The fracture toughness of some the E-P nanocomposites increased up to 70% over the unmodified resin. Microscale rigid particles generally tend to increase the toughness of brittle polymers but reduce toughness of ductile polymers [35]. The mechanisms governing fracture properties of thermoset layered silicate nanocomposites are likely to operate at the microscale. The increase in effective particle volume fraction is also likely to contribute to the fracture energy improvements.

SEM micrographs acquired from fracture surfaces of neat polymer samples and nanocomposites provide insight into the fracture mechanism. Typical findings are shown in Figure 6. The unreinforced matrix has a smooth crack surface, indicating that the resistance to crack propagation is low. In contrast, the nanocomposites exhibited a rougher fracture surface, filled with scale-like terraces and steps. The morphology derives from the presence of organoclay layers that force the crack to propagate along a stepped and tortuous path, thereby dissipating energy during fracture. Close observation revealed fine micro-cracks between the scale-like steps, indicating that the clay layers acted as stress concentrators and promoted the formation of the micro-cracks during loading.

Toughening effects of clay in epoxy/clay nanocomposites have been reported extensively [38–41]. Some investigators concluded that crack arrest and pinning [38], as well as massive shear deformation [41] were responsible for the observed toughening. Composites with a high E/P ratio matrix (Figure 6b) exhibited features described as massive shear yielding induced by the stress concentration of rigid nano particles [41]. As E/P ratio diminishes in matrixes (Figure 6c and d) fracture surfaces exhibited features consistent with crack pinning [42–43] as the dominant mechanism for toughening, and the rigid particles also enhance localized plastic deformation between particles. These results agree with the well known fact that plastic deformation of the matrix is limited in thermoset plastics with high crosslink density and microcrack is a main toughening mechanism [44, 45]. In these systems crosslink density increases and toughenability decreases with epoxy content.

The deformation zones generated ahead of the arrested crack-tip in 4 point bend tests are shown in

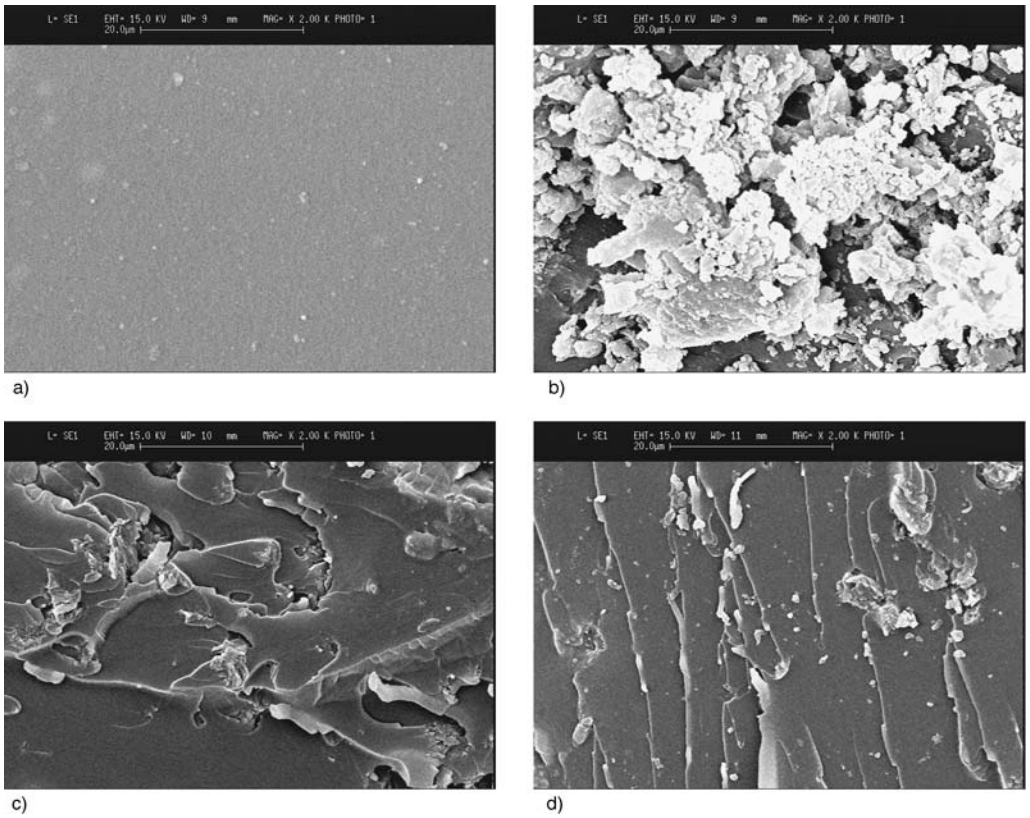

Figure 6. SEM images of fracture surfaces a) E-P(35/65) matrix, b) E-P(35/65) with 2.5 wt% clay, c) E-P(50/50) with 2.5 wt% clay, d) E-P(67/33) with 2.5 wt% clay

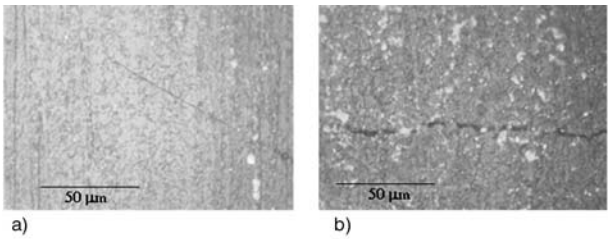

Figure 7. Side views of crack-tip damage for a) E/P matrix and b) E/P with 10 wt% clay specimens under static loading conditions (SEDN-4PB experiments). (Matrix: E-P(35/65)

Figure 7. The bright field micrographs were obtained by transmission optical microscopy (TOM). The unreinforced sample exhibits a smooth crack surface, while the nanocomposites manifest crack trajectories that were tortuous and branched along the crack length.

The findings reported here indicate that multiple mechanisms are involved in the toughening of the current nanocomposites, including microcracking, crack deflection, crack pinning, and matrix shear in different ratios according to the crosslink density of the matrix. However, the toughness reached a maximum for nanocomposites with 2.5–5 wt% of clay content. This is a consequence of two competing processes associated with clay-induced microcracking. Both microcracking and microcrack-enhanced crack deflection are important toughening mechanisms in these materials. Consequently, an increase in clay content will increase the extent of microcracking, and thus, the fracture toughness. On the other hand, as the inter-particle distance becomes smaller at increasing clay contents, the presence of weakly bonded particles resembles cavities ahead of a crack tip. This reduces the material resistance to fracture and forms an extension of the advancing crack. In light of this argument, the fracture toughness of the nanocomposite should decrease with clay content. The combination of the two competing effects gives rise to the maximum in toughness observed for nanocomposites with 2.5–5 wt% of clay content.

4. Impact properties

The dependence of material impact strength on clay content is shown in Figure 8. The error bars indicate the standard deviation.

Impact toughness increases with the change in E-P from 67/33 to 50/50, and a slight additional increase was observed with the change in E-P from

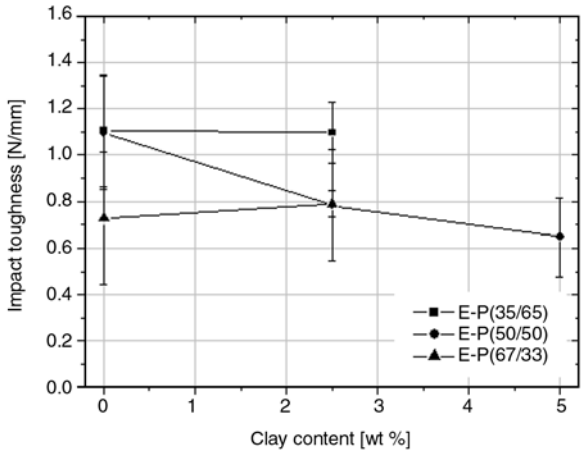

Figure 8. Impact toughness of evaluated nano-materials as a function of clay content

50/50 to 35/65. This trend is similar to the case of fracture toughness measured at quasi-static loading rates. In nanocomposites, the impact strength decreased with increasing clay content, or no effect was found. This can be attributed to the presence of clay particle agglomerates, noted previously, that act as stress concentrators, diminishing impact strength, and the decreasing capability of matrixes to undergo viscoelastic and/or plastic deformation with increasing strain rate [46] SEM images of fracture surfaces from impact toughness tests are shown in Figure 9. The fracture surfaces of the nanocomposites showed irregular, micro-roughened topography consistent with fast crack growth [46–49].

Historically, thermosetting resins such as epoxies have key engineering limitations, including inherent brittleness and moisture uptake. The potential of nano-modifications to achieve an improved toughness-stiffness balance is the motivation for much research, yet general trends have not been conclusively demonstrated for the effects of nano-modifications on impact toughness [49]. However, it has been reported that in general, the impact strength decreases with increasing clay content, especially at high clay contents [49]. Our results suggest that while there was no significant effect of nanoclay additions on impact strength, energy dissipating mechanisms are rate-sensitive. This finding is in agreement with literature data in which the high strain rate attained under impact conditions limited the improvement in strength [43].

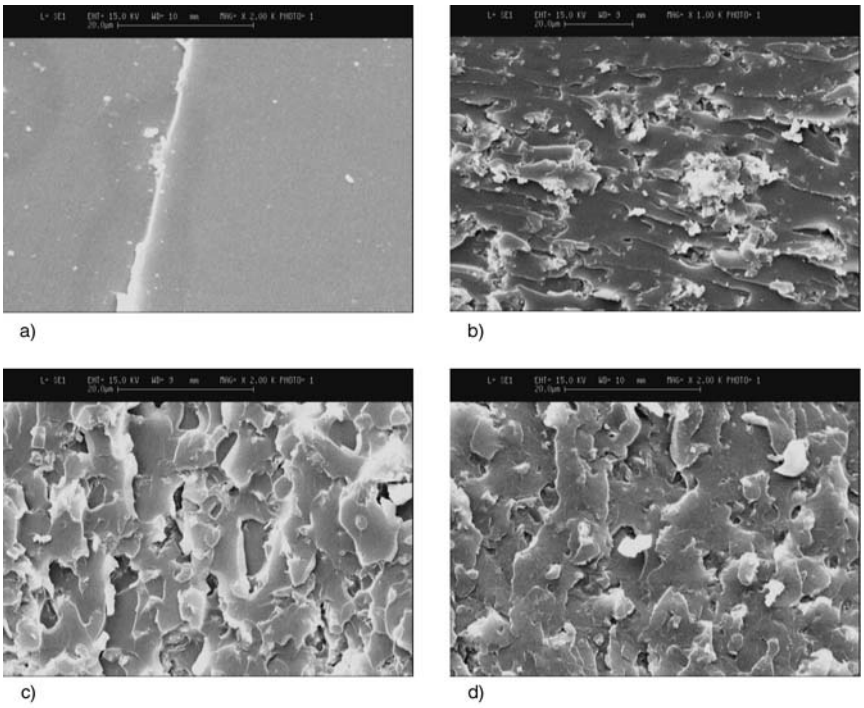

Figure 9. SEM images of fracture surfaces from impact toughness tests a) E-P(35/65) matrix, b) E-P(35/65) with 2.5 wt% clay, c) E-P(50/50) with 2.5 wt% clay, d) E-P(67/33) with 2.5 wt% clay

5. Conclusions

The relationship between the chemical network structures and the mechanical properties of epoxy-phenolic nanocomposites has been elucidated. These nanocomposites show an increase in fracture toughness (70% increase) and Young's modulus (20% increase) compared to the matrix. These enhancements are achieved without a significant decrease in flexural strength. Fractography revealed several mechanisms that contribute to the increase in fracture toughness of the nanoreinforced samples, including micro-cracking, crack deflection, crack pinning, and matrix shear.

The results illustrate the potential to enhance the performance of polymers used for composite matrices through the addition of nanoclays, without diminishing the processing characteristics. Furthermore, the low loadings of organoclay silicates required to achieve these improvements offer promise for performance enhancements with only modest cost increments.

Acknowledgments

The authors are grateful to the Merwyn C. Gill Foundation for financial support.

References

[1] Okada A., Kawasumi M., Usuki A., Kojima Y., Kurauchi T., Kamigaito O.: Swelling behavior of montmorillonite cation exchanged for omega-amino acids by epsilon-caprolactam. Journal of Material Research, **8**, 1174–1178 (1993).

[2] Kojima Y., Usuki A., Kawasumi M., Okada A., Kurauchi T., Kamigaito O.: Synthesis of nylon-6-clay hybrid by montmorillonite intercalated with epsilon-caprolactam. Journal of Polymer Science, Part A: Polymer Chemistry, **31**, 983–986 (1993).

[3] Usuki A., Kojima Y., Kawasumi M., Okada A., Fukushima Y., Kurauchi T., Kamigaito O.: Mechanical-properties of nylon 6-clay hybrid. Journal of Material Research, **8**, 1185–1189 (1993).

[4] Yano K., Usuki A., Okada A., Kuruauchi T., Kamigaito O.: Synthesis and properties of polyimide clay hybrid. Journal of Polymer Science: Part A: Polymer Chemistry, **31**, 2493–2498 (1993).

[5] Okada A., Usuki A.: The chemistry of polymer-clay hybrids. Materials Science and Engineering, **3**, 109–115 (1995).

[6] Lan T., Pinnavaia T. J.: Clay-reinforced epoxy nanocomposites. Chemistry of Materials, **6**, 2216–2219 (1994).

[7] Lan T., Kaviratna P. D., Pinnavaia T. J.: On the nature of polyimide clay hybrid composites. Chemistry of Materials, **6**, 573–575 (1994).

[8] Lan T., Kaviratna P. D., Pinnavaia T. J.: Mechanism of clay tactoid exfoliation in epoxy-clay nanocomposites. Chemistry of Material, **7**, 2144–2150 (1995).
[9] Gilman J. W., Jackson C. L., Morgan A., Harris R.: Flammability properties of polymer-layered-silicate nanocomposites. Chemistry of Materials, **12**, 1866–1872 (2000).
[10] Vaia R. A., Price G., Ruth P. N., Nguyen H. T.: Polymer/layered silicate nanocomposites as high performance ablative materials. Applied Clay Science, **15**, 67–92 (1990).
[11] Messersmith P. B., Giannelis E. P.: Synthesis and characterization of layered silicate-epoxy nanocomposites. Chemistry of Materials, **6**, 1719–1723 (1994).
[12] Messersmith P. B., Giannelis E. P.: Synthesis and barrier properties of poly(epsilon-caprolactone)-layered silicate nanocomposite. Journal of Polymer Science Part A: Polymer Chemistry, **33**, 1047–1052 (1995).
[13] Burnside S. D., Giannelis E. P.: Synthesis and properties of new poly(dimethylsiloxane) nanocomposites. Chemistry of Materials, **7**, 1597–1600 (1995).
[14] Bharadwaj R. K., Mehrabi A. R., Hamilton C., Trujillo C., Murga M., Fan R., Chavira A., Thompson A. K.: Structure-property relationships in cross-linked polyester-clay nanocomposites. Polymer, **43**, 3699–3705 (2002).
[15] Vaia R. A., Giannelis E. P.: Polymer nanocomposites: Status and opportunities. Material Research Society Bulletin, **26**, 394–401 (2001).
[16] Park J. H., Jana S. C.: Mechanism of exfoliation of nanoclay particles in epoxy-clay nanocomposites. Macromolecules, **36**, 2758–2768 (2003).
[17] Giannelis E. P.: Polymer layered silicate nanocomposites. Advanced Materials, **8**, 29–35 (1996).
[18] LeBaron P. C., Wang Z., Pinnavaia T. J.: Polymer-layered silicate nanocomposites: an overview. Applied Clay Science, **15**, 11–29 (1999).
[19] Yeh J. M., Liou S. J., Lai C. Y., Wu P. C., Tsai T. Y.: Enhancement of corrosion protection effect in polyaniline via the formation of polyaniline-clay nanocomposite materials. Chemistry of Materials, **13**, 1131–1136 (2001).
[20] Fornes T. D., Yoon P. J., Hunter D. L., Keskkula H., Paul D. R.: Effect of organoclay structure on nylon 6 nanocomposite morphology and properties. Polymer, **43**, 5915–5933 (2001).
[21] Manfredi L. B., Puglia D., Kenny J. M., Vasquez A.: Structure-properties relationship in resol/montmorillonite nanocomposite. Journal of Applied Polymer Science, **104**, 3082–3089 (2007).
[22] Pappas J., Patel K., Nauman E. B.: Structure and properties of phenolic resin/nanoclay composites synthesized by in situ polymerization. Journal of Applied Polymer Science, **95**, 1169–1174 (2005).
[23] Tyberg C. S., Bergeron K., Sankarapandian M., Shih P., Loos A. C., Dillard D. A., McGrath J. E., Riffle J. S., Sorathia U.: Structure-property relationships of void-free phenolic-epoxy matrix materials. Polymer, **41**, 5053–5062 (2000).
[24] Tyberg C. S., Shih P., Verghese K. N. E., Loos A. C., Lesko J. J., Riffle J. S.: Latent nucleophilic initiators for melt processing phenolic-epoxy matrix composites. Polymer, **41**, 9033–9048 (2000).
[25] Lin-Gibson S., Baranauskas V., Riffle J. S., Sorathia U.: Cresol novolac-epoxy networks: properties and processability. Polymer, **43**, 7389–7398 (2000).
[26] Auad M. L., Zhao L., Nutt S. N., Sorathia U.: Fire-resistant high-performance epoxy-phenolic foam. in '49th International SAMPE Symposium and Exhibition, Long Beach, USA', 305–315 (2004).
[27] Auad M. L., Zhao L., Shen H., Nutt S. R., Sorathia U.: Flammability properties and mechanical performance of epoxy modified phenolic foams. Journal of Applied Polymer Science, **104**, 1399–1407 (2007).
[28] Sue H-J., Yee A. F.: Study of fracture mechanisms of multiphase polymers using the double-notch 4-point-bending method. Journal of Materials Science, **28**, 2975–2980 (1993).
[29] Arias M. L., Frontini P. M., Williams R. J. J.: Analysis of the damage zone around the crack tip for two rubber-modified epoxy matrices exhibiting different toughenability. Polymer, **44**, 1537–1546 (2003).
[30] Kornmann X., Thomann R., Mulhaupt R., Finter J., Berglund L. A.: High performance epoxy-layered silicate nanocomposites. Polymer Engineering and Science, **42**, 1815–1826 (2002).
[31] Chen J-S., Poliks M. D., Ober C. K., Zhang Y., Wiesner U., Giannelis E.: Study of the interlayer expansion mechanism and thermal-mechanical properties of surface-initiated epoxy nanocomposites. Polymer, **43**, 4895–4904 (2002).
[32] Wang K., Wu J., Chen L., He C., Toh M.: Mechanical properties and fracture behavior of epoxy nanocomposites with highly exfoliated pristine clay. in 'ANTEC conference proceedings Chicago, USA', Vol 2, 1820–1824 (2004).
[33] Isik I., Yilmazer U., Bayram G.: Flexural properties and morphology of impact modified epoxy-organoclay nanocomposites. in 'ANTEC conference proceedings Chicago, USA', Vol 3, 2961–2965 (2004).
[34] Kornmann X., Lindberg H., Berglund L. A.: Synthesis of epoxy-clay nanocomposites. Influence of the nature of the curing agent on structure. Polymer, **42**, 4493–4499 (2001).
[35] Zerda A. S., Lesser A. J.: Intercalated clay nanocomposites: Morphology, mechanics, and fracture behavior. Journal of Polymer Science, Part B: Polymer Physics, **39**, 1137–1146 (2001).
[36] Choi M. H., Chung I. J.: Mechanical and thermal properties of phenolic resin-layered silicate nanocomposites synthesized by melt intercalation. Journal of Applied Polymer Science, **90**, 2316–2321 (2003).
[37] Lan T., Kaviratna D., Pinnavaia T. J.: Epoxy self-polymerization in smectite clays. Journal of Physics and Chemistry of Solids, **57**, 1005–1010 (1996).

[38] Becker O., Varley R., Simon G.: Morphology, thermal relaxation and mechanical properties of layered silicate nanocomposites based upon high-functionality epoxy resins. Polymer, **43**, 4365–4373 (2002).

[39] Kornmann X., Thomann R., Mulhaupt R., Finter J., Berglund L. A.: Synthesis of aminecured, epoxy-layered silicate nanocomposites: The influence of the silicate surface modification on the properties. Journal of Applied Polymer Science, **86**, 2643–2652 (2002).

[40] Zilg C., Mülhaupt R., Finter J.: Morphology and toughness/stiffness balance of nanocomposites based upon anhydride-cured epoxy resins and layered silicates. Macromolecular Chemistry and Physics, **200**, 661–667 (1999).

[41] Ratna D., Manoj N. R., Varley R., Singh Raman R. K., Simon G. P.: Clay-reinforced epoxy nanocomposites. Polymer International, **52**, 1403–1407 (2003).

[42] Maazouz A., Sautereau H., Gerard J. F.: Hybrid-particulate composites based on an epoxy matriz, a reactive rubber, and glass beads: morphology, viscoelastic, and mechanical properties. Journal of Applied Polymer Science, **50**, 615–626 (1993).

[43] Bandyopadhyay S.: Macroscopic fracture behavior: Correlation with microscopic aspects of deformation. in 'Toughened plastics I. Science and engineering' (eds.: Riew C. K., Kinloch A. J.). American Chemical Society, Washington D.C., 211–258 (1993).

[44] Lu F., Plummer C. J. G., Cantwell W. J., Kausch H-H.: Toughening mechanisms in modified epoxy resins with different crosslink densities. Polymer Bulletin, **37**, 399–406 (1996).

[45] Shiann H. L., Nauman E. B.: Effect of cross-linking density on the toughening mechanisms of rubber-modified thermosets. Journal of Materials Science, **26**, 81–90 (1991).

[46] Yee A. F., Du J., Thouless M. D.: Toughening of epoxies. In 'Polymer Blends' (Eds.: Paul D. R, Bucknall C. B.), John Wiley and Sons, New York, 225–267 (2000).

[47] Chan J., Gillham J. K., Kinloch A. J., Shaw S. J.: Rubber-modified epoxies: morphology, transitions, and mechanical properties. in 'Rubber-modified thermoset resins' (eds.: Riew C. K., Gillham J. K.), American Chemical Society, Washington D.C., 261–279 (1984).

[48] Bascom W. D., Hunston D. L.: Fracture of elastomer-modified epoxy polymers. in 'Rubber-toughened plastics' (ed.: Riew K.), American Chemical Society, Washington D.C., 135–172 (1989).

[49] Isik I., Yilmazer U., Bayram G.: Impact modified epoxy/montmorillonite nanocomposites: synthesis and characterization. Polymer, **44**, 6371–6377 (2003).